Impact of Morphology and Confinement Effects on the Properties of Aligned Nanofiber Architectures

by

Itai Y. Stein

Submitted to the Department of Mechanical Engineering
in partial fulfillment of the requirements for the degree of

Doctor of Philosophy in Mechanical Engineering

at the

MASSACHUSETTS INSTITUTE OF TECHNOLOGY

June 2016

© Massachusetts Institute of Technology 2016. All rights reserved.

Author . . . .
Department of Mechanical Engineering
May 9, 2016

Certified by . . . .
Brian L. Wardle
Professor of Aeronautics and Astronautics
Thesis Supervisor

Certified by . . . .
Evelyn N. Wang
Gail E. Kendall Associate Professor of Mechanical Engineering
Chairman, Thesis Committee

Certified by . . . .
A. John Hart
Associate Professor of Mechanical Engineering
Mitsui Career Development Professor in Contemporary Technology
Thesis Committee

Certified by . . . .
Alexie M. Kolpak
Assistant Professor of Mechanical Engineering
Rockwell International Career Development Professor
Thesis Committee

Accepted by . . . .
Rohan C. Abeyaratne
Professor of Mechanical Engineering
Quentin Berg Professor of Mechanics
Chairman, Department Graduate Committee

Impact of Morphology and Confinement Effects on the Properties of Aligned Nanofiber Architectures

by

Itai Y. Stein

Submitted to the Department of Mechanical Engineering
on May 9, 2016, in partial fulfillment of the
requirements for the degree of
Doctor of Philosophy in Mechanical Engineering

Abstract

The intrinsic and scale-dependent properties of nanofibers (NFs), nanowires, and nanotubes have made them the focus of many application-specific nanostructured materials studies. However, various NF morphology and proximity effects can lead to $> 1000\times$ reductions in the performance of NF-based material architectures, such as bulk materials and structures comprised of scalable aligned NF arrays. The physical and chemical origins of these effects, along with the concomitant structure-property mechanisms of materials comprised of aligned NFs, are not currently known and cannot be properly integrated into existing theories. This originates, in part, from an incomplete understanding of the morphology of real NF systems, particularly in three-dimensions.

Through experiments, theory, and multi-scale simulation, this dissertation presents a framework capable of modeling the stochastic 3D morphology of a relevant NF system, carbon nanotubes (CNTs), assembled into aligned CNT (A-CNT) arrays. New descriptions of the multi-wall A-CNT morphology demonstrate that the CNT tortuosity, quantified via sinusoidal amplitude-wavelength waviness ratio (w), decreases significantly from $w \approx 0.2$ to 0.1 as the CNT volume fraction (V_f) is increased from $V_\mathrm{f} \sim 1$ to 20%. Using these new relations, a 3D stochastic morphology description is presented, and used to quantify the mechanical behavior of A-CNT arrays, A-CNT polymer matrix nanocomposites (A-PNCs), and A-CNT carbon matrix nanocomposites (A-CMNCs) via a mechanics analysis that was previously applied to carbon nanocoils. Focusing on deformations in the A-CNT axial reinforcement direction, torsion and shear deformation mechanisms, which are governed by the low (< 1 GPa) intrinsic shear modulus of the CNTs, are shown to have an effective compliance contribution of $> 90\%$ in the experimental A-CNT w regime, and are inferred to be the physical mechanisms responsible for the previously observed $\sim 100\times$ increase in the A-CNT effective indentation modulus as V_f is increased from ~ 1 to 20%. In the case of A-PNCs, the polymer matrix effectively eliminates the torsion compliance contribution, so that the observed $\sim 2\times$ enhancement in the effective axial elastic modulus of A-PNCs as V_f is increased from ~ 1 to 20% is explained. The geometry of the graphitic crystallites that comprise the pyrolytic carbon (PyC) matrix of A-CMNCs is found to not evolve significantly at pyrolysis temperatures of 1000 to 1400°C, and crystallite size estimates from Raman spectroscopy reveal that the Tuinstra-Koenig correlation disagrees with the sizes measured by x-ray diffraction, suggesting a new amorphization transition crystallite size of 6 nm instead of $2-3$ nm. In the case of A-CMNCs, CNT reinforcement is shown to lower the energy barrier (inferred through the pyrolysis temperature) for meso-scale self-organization of the graphitic crystallites of the PyC matrix, while having no effect on the PyC matrix on the atomic scale. Mechanical property analysis and modeling indicates that the aerospace materials selection criterion of the A-CMNCs can be enhanced to > 8 GPa $\times$ (g/cm^3)$^{-2}$ at $V_\mathrm{f} > 20\%$ (experimentally we observe a value of ~ 5 GPa $\times$ (g/cm^3)$^{-2}$ at $V_\mathrm{f} \sim 10\%$). A-CMNCs introduced in this work have the potential to outperform state-of-the-art superhard materials, such as diamond (≈ 7.8 GPa $\times$ (g/cm^3)$^{-2}$) and cubic boron nitride (≈ 5.2 GPa $\times$ (g/cm^3)$^{-2}$).

Using the structure-property prediction tools developed in this thesis, precise tailoring and prediction of application-specific performance of aligned NF based architectures is enabled, and specific new understanding of A-CNT systems is established. Future paths of study that enable the design and manufacture of several classes of next-generation materials are recommended.

Thesis Supervisor: Brian L. Wardle
Title: Professor of Aeronautics and Astronautics

Acknowledgements

The list of people that made this work possible is long, and at the forefront is Prof. Brian Wardle, without whom this project would be impossible. Thanks to my committee members, Profs. Wang, Hart, and Kolpak, for all their support and guidance. I could not have done this without you. Thanks to all the members of necstlab for their help and advice throughout the last five years. Teamwork and collaboration are what a great work environment is all about. A special thanks to Stevie, who pushed me very hard when I was still new to necstlab - he is part of the reason I accomplished as much as I did during my time at MIT. Thanks to all my great UROPs and CMSE summer scholars: Henna, Peter, Hanna, JJ, Mackenzie, Naomi, Roget, Chlöe, and Alex - their contributions to my work and this dissertation were priceless. Many thanks to all my great mentors from Carnegie Mellon University, whose teaching and guidance enabled me to come to MIT for graduate school: Profs. Islam, McGaughey, and Bockstaller. Last but not least, a very special thanks to my family and friends for supporting me throughout this entire process, and for keeping me sane when the workloads were simply not.

This thesis is dedicated to my beautiful wife Isabella
without whose support, love, smiles, and laughter my life would not be the same.

Contents

Acknowledgements **5**

Contents **7**

List of Figures **11**

List of Tables **21**

Abbreviations and Symbols **23**

1 Introduction **29**

1.1 Aligned Carbon Nanotubes for Next-Generation Materials 30

1.2 Thesis Outline 32

2 Background **35**

2.1 Overview of A-CNT Physical Properties 36

2.2 State-of-the-Art Multi-scale Modeling and Simulation Techniques 40

2.3 The Path Toward More Accurate Property Prediction Tools 43

2.4 Conclusions 45

3 Objectives and Approach **47**

3.1 Objectives 47

3.2 General Approach 47

3.2.1 Three-dimensional Morphology of A-CNTs 48

3.2.2 Mechanical Property Prediction for A-CNT Systems 49

3.2.3 Limitations of Current Work 51

4 Morphology of Aligned Carbon Nanotube Architectures 53
4.1 Current State of the Art of A-CNT Morphology Quantification 54
4.2 Morphology Characterization, Modeling, and Simulation 56
4.2.1 Experimental Quantification of A-CNT Waviness 56
4.2.2 Theoretical Framework for Deterministic Waviness Corrected A-CNT Packing Geometry 57
4.2.2.1 Inter-CNT Spacing Relations 58
4.2.2.2 Waviness Correction for Square and Hexagonal Packing 59
4.2.3 Simulation Framework for Stochastic 3D A-CNT Morphology 59
4.2.3.1 Three-Dimensional Morphology Simulation Scheme 59
4.2.3.2 Unit Cell Analysis for Simulating Morphology in 3D 61
4.3 Results and Discussion 63
4.3.1 Evaluation of Morphology Error Scaling and Validity Regime for Simulation Framework 63
4.3.2 Experimental Quantification of A-CNT Waviness Evolution with V_f 65
4.3.3 Waviness Corrected A-CNT Packing Structure 67
4.4 Conclusions and Recommendations for Future Work 72

5 Elastic Modeling of Aligned Carbon Nanotube Arrays 75
5.1 Compliance Prediction of A-CNT Arrays 75
5.2 Modeling of A-CNT Mechanical Behavior 77
5.2.1 Unit Cell Analysis 78
5.2.2 A-CNT Array Effective Modulus from Compliance Contribution of Deformation Modes 79
5.3 Guide for Applying This Simulation Framework to Other Aligned Nanofiber Systems 79
5.4 Results and Discussion 80
5.4.1 Deformation Mode Contribution to Effective A-CNT Compliance 81
5.4.2 A-CNT Array Effective Modulus Scaling 82
5.5 Conclusions and Recommendations for Future Work 84

6 Aligned Carbon Nanotube Polymer Matrix Nanocomposites 87
6.1 Elastic Axial Stiffness Prediction for A-PNCs 87
6.2 Modeling of A-PNC Elastic Behavior 89

6.2.1 Waviness Evolution 89
6.2.2 Mechanical Modeling and Effective CNT Modulus 90
6.3 Results and Discussion 92
6.3.1 Deformation Mode Contribution to Axial Effective A-PNC Compliance . . 92
6.3.2 A-PNC Array Effective Modulus Scaling 93
6.4 Conclusions and Recommendations for Future Work 95

7 Carbon Matrix and Aligned Carbon Nanotube Carbon Matrix Nancomposites 97
7.1 Structure and Mechanical Properties of PyCs and A-CMNCs Derived *via* Polymeric Precursors 98
7.2 Synthesis and Processing Techniques 106
7.3 Structure-Mechanical Property Characterization and Modeling 107
7.3.1 Structure and Morphology Characterization 107
7.3.1.1 XRD Analysis 107
7.3.1.2 Raman Spectroscopy Analysis 107
7.3.1.3 FTIR Analysis 108
7.3.1.4 Theoretical Framework for Matrix Density Scaling with Crystallite Geometry 109
7.3.2 Hardness Scaling 110
7.3.2.1 Experimental Vickers Microhardness Evaluation 110
7.3.2.2 Theoretical Framework for Hardness Scaling with Crystallite Size and Thickness 110
7.3.2.3 Effective Axial A-CMNC Modulus *via* 3D A-CNT Morphology . 112
7.4 Results and Discussion 113
7.4.1 PyC Structure and Morphology 114
7.4.1.1 Graphitic Crystallite Size and Thickness Scaling 114
7.4.1.2 Bonding Character Evolution 119
7.4.1.3 Chemical Structure Evolution 122
7.4.1.4 Apparent Density Scaling 125
7.4.2 Mechanical Behavior Scaling 127
7.4.2.1 Pyrolysis Temperature Dependence 127
7.4.2.2 Scaling of Axial Effective Modulus with CNT Packing Proximity 131

7.5 Conclusions and Recommendations for Future Work 134

8 Conclusions and Recommendations 137

8.1 Summary of Thesis Contributions 138

8.2 Recommendations for Future Work 143

A Waviness Data 147

References 151

List of Figures

1.1 Reported mechanical and thermal properties of CNTs. (a) Specific modulus-specific strength plot comparing the properties of composite materials to other engineering materials, such CNTs. (b) Thermal properties of CNTs as a function of their diameter showing that their phonon transport properties are diminished as a function of their diameter based on the plot reported in Marconnet et al. Since CNTs promise higher specific stiffness, specific strength, and phonon transport properties, many groups are currently working on their incorporation into composite architectures. . 31

1.2 Reported stiffness for CNT systems as a function of their size, original to this thesis, reproduced from Stein, Lewis, and Wardle. The plot shows how the elastic modulus (E), when normalized by the CNT volume fraction (V_f), scales with the number of CNTs enclosed in the structure demonstrating that isolated CNTs and CNT bundles/fibers exhibit $E/V_\mathrm{f} > 100$ GPa, whereas larger scale CNT pillars and arrays exhibit $E/V_\mathrm{f} \lessapprox 1$ GPa. 32

2.1 Scaling of effectivek_eff electrical conductivity (σ_eff) as a function of the CNT volume fraction (V_f) for unaligned CNTs (U-CNTs), A-CNTs, and A-PNCs, underscoring that the σ_eff previously reported for CNT systems is lower than the $\sigma > 10^8$ S/m figure predicted by theory at room temperature. 36

2.2 Thermal properties of CNTs, graphene, and other carbon allotropes at room temperature as presented by Pop et al. (a) Plot summarizing the effective k_eff thermal conductivity (k_eff) values of CNTs, graphene, graphite, and diamond illustrating that suspended graphene, CNTs, and diamond can achieve $k \sim 3000$ W/mK. (b) k_eff as a function of the phonon MFP showing that suspended graphene achieves the highest k_eff value because it has the longest MFP (~ 600 nm). 38

2.3 Scaling of the 2D modulus (E_{2D}) and 3D modulus (E_{3D}) of graphene as a function of the defect density as presented by López-Polín et al. This plot shows that carefully tuning the defect density can enhance the mechanical properties of graphene, whereas $> 1\%$ missing atoms in graphene will lead to diminished stiffness. 39

2.4 Illustration showing the treatment of the C$-$C bond as an effective structural element by the MSM approach as presented by Eberhardt and Wallmersperger. 41

2.5 Illustration of the atomistic and corresponding mesoscopic treatment of a CNT as presented by Cranford and Buehler. 42

4.1 Real wavy A-CNTs and theoretical frameworks. (a) Representative HRSEM image of wavy A-CNTs. (b) Illustration of the CNT morphology normally assumed in existing theoretical frameworks, which neglect the CNT waviness, and the wavy CNTs with realistic stochastic morphologies generated using the simulation framework presented here. 55

4.2 3D morphology of the A-CNTs that comprise A-PNCs visualized *via* quantitative electron tomography as presented by Natarajan et al. 56

4.3 Tortuosity (τ) as a function of waviness ratio (w) for sinusoidal (Eq. 4.1a) and helical (Eq. 4.1b) functional forms of the CNT morphology. Inset shows an illustration of w using the sinusoidal amplitude/wavelength (a/λ) functional form, and w for the helical functional form (not illustrated) would be evaluated by defining the helix radius as a. 57

4.4 Illustration of N, and the effective constitutive triangles that comprise each coordination. The average of Γ_{min} and Γ_{max}, defined as Γ, is used in throughout this dissertation as an easily accessible measure of the morphology of A-CNT ($\rightarrow \Gamma$). . 58

4.5 Three-dimensional morphology simulation details. (a) Illustration of the simulation scheme, origin of Γ from N, and the top view of an initialized simulation cell comprised of collimated 100 CNTs for $N = 4$ (square packing) and $N = 6$ (hexagonal packing). (b) Initialized simulation comprised of 100 wavy CNTs showing how the average node displacements in the $x-y$ plane and z direction are tied to the a and λ that originate from the experimentally-quantified sinusoidal w ($\rightarrow w = a/\lambda$) and used to generate wavy CNTs. 60

4.6 Unit cell used in the analysis defined using the average displacement in the $x-y$ plane ($\rightarrow \Delta r$) and 10 nodes in the z direction ($\rightarrow \Delta z$). Δr and Δz are tied to the amplitude (a) and wavelength (λ) from the waviness ratio ($w = a/\lambda$) which is used to simulate the morphology of the CNTs in three dimensions. The radius of curvature (R_{c}) is evaluated using the unit cell, and is used to approximate the maximum CNT volume fraction that the simulation can be used to study as discussed below. 62

4.7 Factors that link $\chi(w)$ and $\zeta(w)$ to w for A-CNTs studied in this work. (a) $\chi(w)$ scaling with w demonstrating that CNT interactions with the hard boundaries that define the confining volume are significant at $w \gtrapprox 0.3$ where $\chi(w)$ transitions from a linear scaling (see Eq.4.6a) to a power scaling. (b) $\zeta(w)$ scaling with w demonstrating that CNT-boundary interactions are significant at $w \gtrapprox 0.3$ where $\zeta(w)$ transitions from a power scaling (see Eq. 4.6b) to a linear scaling. 63

4.8 Standard error scaling and V_{f} validity regime. (a) Scaling in standard error of the measured Γ values demonstrating the importance of number of CNTs in the simulation (n), and replicating the familiar $1/\sqrt{n}$ standard error scaling for Gaussian statistics. (b) Plot showing the evolution of the CNT alignment, represented by R_{c}, as a function of w. 64

4.9 Evolution of the CNT waviness with packing. (a) Cross-sectional HRSEM micrographs of A-CNT arrays at V_{f} ranging from $\sim 1-20$ vol. % CNTs showing the reduction in CNT waviness. (b) Plot demonstrating that w can be reduced by $\sim 50\%$ by increasing V_{f} from ~ 1 vol. % CNTs to ~ 20 vol. % CNTs. 66

4.10 Impact of waviness (w) on the packing morphology of A-CNT arrays for square and hexagonal close packing. (a) Evolution of the waviness correction (see Eq.(4.4)) for square packing ($\Omega_{\square}$) as a function of w showing that the scaling of $\Omega_{\square}$ can be represented by three power laws at $w < 0.05$, $0.05 \leq w \leq 0.125$, and $w > 0.125$, and that square packing is best suited for A-CNT systems with $w \gtrapprox 0.15$ where $\Omega_{\square}$ increases very gradually. (b) Scaling of the waviness correction (see Eq.(4.4)) for hexagonal packing ($\Omega_{\hexagon}$) with w showing that $\Omega_{\hexagon}$ can be described by two power laws at $w < 0.1$, and $w \geq 0.1$, and that hexagonal packing is best suited for CNT systems with $w \lessapprox 0.05$ where $< 1\%$ error will be induced by neglecting the CNT waviness. 68

4.11 Evolution of morphology of A-CNTs as a function of their V_f. (a) Experimentally determined Γ as a function of V_f, previously reported theoretical scaling of Γ with V_f for collimated A-CNTs, and the simulated scaling of Γ with V_f for wavy A-CNTs. Inset: scaling of Ω with V_f. (b) The evolution of N during packing resulting from the previously reported theoretical scaling for collimated A-CNTs and their bundles, and the simulated scaling for wavy A-CNTs showing that integration of CNT waviness into the theoretical framework is necessary to attain a coordination number scaling that is applicable beyond $V_\mathrm{f} = 20\%$. 70

5.1 Elastic behavior of A-CNTs under compression as presented by Cao et al. (a) Illustration of the buckling modes of A-CNTs. (b) Resulting stress-strain curve and E_eff for A-CNTs. 76

5.2 Deformation mechanisms of a carbon nanocoil as presented by Chen et al. 77

5.3 Illustration and scaling of the compliance contribution ($\rightarrow \xi_\mathrm{mode}/\xi_\mathrm{tot}$ where $\xi_\mathrm{tot} = \sum \xi$) of the four deformation modes as a function of the waviness ratio (w) at CNT volume fraction (V_f) of $V_\mathrm{f} = 1\%$ CNTs. 81

5.4 Contribution of extension, shear, bending, and torsion deformation mechanisms (see Eq. 5.1 to the effective compliance ($\rightarrow \xi_\mathrm{mode}/\xi_\mathrm{tot}$ where $\xi_\mathrm{tot} = \sum \xi$) of wavy CNTs as a function of the waviness ratio (w) and CNT volume fraction. (a) Deformation mode contributions for CNTs with $V_\mathrm{f} \approx 5\%$. (b) Deformation mode contributions for CNTs with $V_\mathrm{f} \approx 10\%$. (c) Deformation mode contributions for CNTs with $V_\mathrm{f} \approx 20\%$. (d) Deformation mode contributions for CNTs with $V_\mathrm{f} \approx 40\%$. 82

5.5 Elastic response of wavy aligned CNTs. (a) Plot of the effective axial modulus of wavy CNTs ($E_\mathrm{cnt}(w)$) normalized by the intrinsic modulus of straight CNTs ($E_\mathrm{cnt}(0)$) as a function of w and V_f indicating that waviness can lead to orders of magnitude reductions in modulus. (b) Plot comparing the scaling of the effective modulus with V_f ($\rightarrow E_\mathrm{cnt}(V_\mathrm{f})$) for the 10^5 simulated wavy CNTs (via Eq. 5.3) to the previously reported experimental and theoretical scaling of $E_\mathrm{cnt}(V_\mathrm{f})$. This plot shows that the shear modulus (G) of the CNTs, which dominates the torsion and shear deformation mechanisms, governs the scaling of $E_\mathrm{cnt}(V_\mathrm{f})$. 83

6.1 Experimentally determined and rule of mixtures predicted V_f scaling of E_pnc. (a) Plot comparing the experimental scaling of $E_\mathrm{pnc}(V_\mathrm{f})$ to the values predicted by rule of mixtures for $E_\mathrm{pm} \approx 3.1$ GPa showing the large overpredictions of rule of mixtures. (b) Plot comparing the experimental scaling of $E_\mathrm{pnc}(V_\mathrm{f})$ to the values predicted by rule of mixtures for $E_\mathrm{pm} \approx 4.7$ GPa showing again the orders of magnitude overpredictions of E_pnc by rule of mixtures. 88

6.2 Top view of a simulated carbon nanotube (CNT) illustrating the two-dimensional random walk that comprises the waviness (left), side view of an aligned carbon nanotube polymer matrix nanocomposite (A-PNC) comprised of simulated wavy CNTs (center), and illustration of the unit cell used in the morphology and mechanical property analysis (right) showing the three CNT deformation modes that contribute to the elastic response of the wavy CNTs in the A-PNC. 91

6.3 Contribution of extension, shear,and bending deformation mechanisms (see Eq. 6.2a) to the effective compliance ($\rightarrow \xi_\mathrm{mode}/\xi_\mathrm{tot}$ where $\xi_\mathrm{tot} = \sum \xi$) of wavy CNTs that comprise the A-PNC as a function of the waviness ratio (w) and ratio of the intrinsic CNT longitudinal and shear moduli ($\rightarrow Y/G$) for $Y/G = 1000$ (●), $Y/G = 250$ (■), $Y/G = 100$ (▼), and $Y/G = 10$ (▲). (a) Extension mode contributions. (b) Shear mode contributions. (c) Bending mode contributions. 93

6.4 Plot of the effective modulus of wavy CNTs ($E_\mathrm{cnt}(w)$) as a function of the waviness ratio (w) demonstrating that waviness can lead to orders of magnitude reductions in stiffness. 94

6.5 Axial modulus scaling with V_f for A-PNCs. (a) Plot comparing the scaling of $E_\mathrm{pnc}(V_\mathrm{f})$ as a function of the CNT morphology (via Eq. 6.1 $\rightarrow w(V_\mathrm{f})$ and Eqs. 6.2a–6.2f) to a previously reported experimental and FEA scaling of $E_\mathrm{pnc}(V_\mathrm{f})$ where the effective shear modulus of the CNTs is $G \approx 3.1$ GPa. This plot shows that including the evolution of w with V_f better represents observed scaling of $E_\mathrm{pnc}(V_\mathrm{f})$, and that A-CNT infusion with a polymer to form A-PNCs reduces $w(V_\mathrm{f})$ by $\approx 25\%$ ($\rightarrow \Lambda \approx 0.75$). (b) Plot comparing the scaling of $E_\mathrm{pnc}(V_\mathrm{f})$ as a function of the CNT morphology (via Eq. 6.1 and Eqs. 6.2a–6.2f) to a previously reported experimental and FEA scaling of $E_\mathrm{pnc}(V_\mathrm{f})$ where $G \approx 4.7$ GPa. This plot demonstrates that a $\approx 10\%$ reduction in $w(V_\mathrm{f})$ ($\rightarrow \Lambda \approx 0.9$) during A-PNC synthesis can best represent the previously observed scaling of $E_\mathrm{pnc}(V_\mathrm{f})$. 95

7.1 Structure and geometry of the graphitic crystallites that comprise PyC. (a) Illustration of exemplary LD and HD packing structures of graphitic crystallites in PyC where a $\sim 15\%$ increase in density from LD to HD is typical. (b) Illustration of L_a and L_c used to approximate the size and geometry of the crystallites that comprise PyCs, and their relationship with the [100] and [001] $hk\ell$ lattice directions that orthogonal to the (100) and (002) lattice planes. Note: for the illustrated 3-layer crystallite, L_c is twice the inter-layer separation. 99

7.2 Illustration of the previously proposed mechanism of graphite transformation into defective diamond consisting of three stages: (1) graphite → nanocrystalline (NC) graphite; (2) NC graphite → amorphous carbon (a-C); (3) a-C → tetrahedral amorphous carbon (ta-C). (a) Position of the G band as a function of amorphization stage (sp^3) character demonstrating that the maximum G peak position occurs between stages 1 and 2. (b) Inverse of the ratio of the intensities of the G and D bands ($I_\mathrm{G}/I_\mathrm{D}$) illustrating that the minimum value of $I_\mathrm{G}/I_\mathrm{D}$ occurs between stages 1 and 2. Reproduced from Ferrari and Robertson. 101

7.3 Previously reported scaling of H_V for LD (●, and ■) and HD (▼) PyCs as a function of L_a, (a), and L_c, (b), showing the wide spread and a lack of a robust trend. 103

7.4 Previously reported scaling of hardness (H_V), estimated *via* nanoindentation, to the effective modulus (E_eff) of a variety of carbon and silicon based materials as presented Gogotsi et al. 105

7.5 Theoretical framework and model predictions for the PyC matrix density (ρ_pyc). (a) Illustration of the crystallite stacking and unit cell representing the structure of an LD PyC exhibiting an 'open structure'. (b) Plot of ρ_pyc as a function the crystallite orientation angle (θ_oa) for a variety of crystallite geometries (L_a/L_c). 109

7.6 Illustration of the indentation technique utilized to experimentally quantify the mechanical behavior of the PyCs and A-CMNCs, *i.e.* *via* hardness (H_V). The inset presented illustrations of the deformation mechanisms that govern the measured H_V, and the model orientation angle (θ_th) where they are most relevant. 111

7.7 XRD analysis results for *in situ* pyrolysis of PyCs, A-CNTs, and A-CMNCs as a function of T_p. (a) XRD patterns of phenolic resin pyrolysis (transforming into PyC) showing the evolution of the (002) and (100) peaks. (b) XRD patterns of A-CNTs heated up to 1500°C demonstrating that heat treatments at $\lesssim$ 1000°C lead to little change in the original CNT structure. (c) XRD patterns of A-PNC precursors transforming into A-CMNCs. 115

7.8 XRD analysis results for *ex situ* pyrolysis of PyCs as a function of the pyrolysis temperature (T_p). (a) XRD patterns showing the evolution of the (002) and (100) peaks as a function of T_p. (b) L_a and L_c as a function of T_p. (c) d_{002} evolution as a function of T_p. 116

7.9 XRD analysis results for *ex situ* pyrolysis of A-CMNCs as a function of T_p. (a) XRD patterns showing the evolution of the (002), (100), and (110) peaks as a function of T_p. (b) L_a and L_c as a function of T_p. (c) d_{002} evolution as a function of T_p. 117

7.10 Raman spectroscopy analysis results as a function of T_p utilizing samples from both the *in situ* and *ex situ* pyrolysis approaches. (a) Raman spectra (experimental curves and fits *via* Eq. 7.4) showing the evolution of the D and G bands as a function of T_p. (b) Evolution of $I_\mathrm{D}/I_\mathrm{G}$ and $A_\mathrm{D}/A_\mathrm{G}$ as a function of T_p. (c) Scaling of γ_D and γ_G as a function of T_p. 119

7.11 Scaling of the intensity ratio of the D- and G-bands ($I_\mathrm{D}/I_\mathrm{G}$) as a function of the crystallite size (L_a) showing that the previously proposed approximations of L_a from $I_\mathrm{D}/I_\mathrm{G}$ (Eq. 7.3) are not representative here. Since the $I_\mathrm{D}/I_\mathrm{G} \propto L_\mathrm{a}^{-1}$ scaling proposed by Eq. 7.3a and Eq. 7.3b are not exhibited by the experimental data, whereas $I_\mathrm{D}/I_\mathrm{G} \propto L_\mathrm{a}^2$ scaling proposed in Eq. 7.3c is more representative of the experimental data, Eq. 7.10, which modified the intersection point of Eq. 7.3c and Eq. 7.3b to a more realistic value ($\rightarrow L_\mathrm{a} \approx 6.5 \pm 0.5$ nm, instead of $\sim 2-3$ nm), is the only scaling relation that is able to capture the trend in the data. 120

7.12 Raman spectroscopy analysis results for A-CMNCs as a function of the CNT volume fraction (V_f). (a) Raman spectra (experimental curves and fits *via* Eq. 7.4) showing the evolution of the D and G bands as a function of V_f. (b) Evolution of $I_\mathrm{D}/I_\mathrm{G}$ and $A_\mathrm{D}/A_\mathrm{G}$ as a function of V_f. (c) Scaling of Γ_D and Γ_G of the D and G bands as a function of V_f. 122

7.13 Representative FTIR spectra for *in situ* pyrolysis of PyCs and A-CNTs as a function of the pyrolysis temperature (T_p). (a) FTIR spectra for cured phenolic resin transforming into PyC for T_p up to 1000°C illustrating that $-$OH groups are present on the surface of the PyCs, and that $\mathrm{C-O_2}$, $\mathrm{H_2O}$ and methylene groups are released as byproducts of the pyrolyzation leading the bands at 1233 $\mathrm{cm^{-1}}$ and 1474 $\mathrm{cm^{-1}}$ to disappear, and a band corresponding to a more complex polyaromatic system to appear at 1636 $\mathrm{cm^{-1}}$. (b) FTIR spectra of A-CNTs before and after thermal treatment at $T_\mathrm{p} = 1500$°C demonstrating that $-$OH groups are present on the surface of the CNTs, as observed previously, and that the CNTs that comprise the A-CNTs are highly thermally stable since no chemical structure alterations are seen at < 1800 $\mathrm{cm^{-1}}$. 123

7.14 Representative FTIR spectra for *ex situ* pyrolysis of PyCs and A-CMNCs as a function of the pyrolysis temperature (T_p). (a) FTIR spectra for PyCs as a function of T_p up to 1400°C. (b) FTIR spectra of A-CMNCs as a function of T_p up to 1400°C showing slight changes in the chemical structure of A-CMNCs as a function of T_p. 124

7.15 Evolution of PyC density, ρ_pyc (from Eq. 7.6), as a function of crystallite geometry, L_a/L_c, and orientation angle, θ_oa. The predictions of Eq. 7.6 agree very well with previous data on ρ_pyc for HD PyCs (from Zhang et al.), but overestimates ρ_pyc for LD PyCs (from the current work, Yajima et al., and Zhang et al.) due to the presence of a significant amount of > 100 nm diameter pores in such PyCs. 125

7.16 Scaling of hardness (H_V) as a function of pyrolysis temperature (T_p) for the PyCs studied here, and in previous works. Good agreement with Eq. 7.7b indicates that the low inter-layer shear modulus of the graphitic crystallites governs the measured H_V. 127

7.17 Hardness (H_V) as a function of apparent density (ρ) for the PyCs studied here and various other PyCs, carbon materials, and superhard materials such as carbides, nitrides, oxides, and phosphides showing that for lightweight applications such as aerospace (*i.e.* design parameter of H_V/ρ^2), PyCs are among the leading candidate materials. 130

7.18 Axial modulus scaling with V_f for A-CMNCs. The scaling of $E_\mathrm{cmnc}(V_\mathrm{f})$ as a function of the CNT morphology (via Eq. 7.9) is compared to the experimentally quantified $E_\mathrm{cmnc}(V_\mathrm{f})$ that was converted from H_V using the previously reported empirical conversion factor of $E_\mathrm{cmnc}/H_\mathrm{V} \sim 8-12\times$. Additionally, the theoretical and experimental $E_\mathrm{cmnc}(V_\mathrm{f})$ results are compared to the results of a previous simulation study on an A-CMNC that has an a-C matrix. 132

7.19 Hardness (H_V) as a function of density (ρ) for the A-CMNCs studied here and various other PyCs, carbon materials, and superhard materials as summarized in Figure 7.17. This plot shows that A-CMNCs synthesized at $V_\mathrm{f} > 30\%$ could outperform diamond in super lightweight aerospace structure that use H_V/ρ^2 design parameter for materials selection. 133

List of Tables

4.1 Experimentally determined w and τ from Eq. 4.1 as a function of V_f. The included values of experimental mean and standard deviation $\mu_\mathrm{w}^\mathrm{sin}$, $\delta_\mathrm{w}^\mathrm{sin}$, and their calculated sinusoidal and helical forms μ_τ^sin, δ_τ^sin, μ_τ^helix, and $\delta_\tau^\mathrm{helix}$ were approximated from 30 CNTs ($\rightarrow n = 30$). See Appendix A for the raw waviness data. 67

4.2 Γ and Ω as a function of V_f, evaluated using the simulation described in Section 4.2.3. 71

4.3 N estimated for A-CNT arrays as a function of V_f, evaluated using previously reported experimental data (see Figure 4.11). 72

7.1 Experimental and theoretical values of in-plane (C_{11}), out-of-plane (C_{33}), and interlayer shear (C_{44}) elastic constants for graphene/graphite as reported by Savini et al. 110

7.2 Crystallite geometry estimated from XRD that includes L_a (via Eq. 7.1a), L_c (via Eq. 7.1b), and d_{002} (via Eq. 7.2) with standard deviation as a function of pyrolysis temperature (T_p) for the *in situ* and *ex situ* pyrolyzation approaches. 116

7.3 Experimental and theoretical (from Eq. 7.6 and Eq. 7.7b) values of hardness (H_V) and apparent density (ρ_pyc) for PyCs as a function of pyrolysis temperature (T_p), and the experimental specific hardness using the H_V/ρ and H_V/ρ^2 design parameters for comparison with other superhard materials. Since the current theoretical model for ρ_pyc is not capable of accounting for porosity in the PyCs, the predicted ρ_pyc values are significantly higher than those measured experimentally, thereby leading to the theoretical H_V/ρ and H_V/ρ^2 to be far lower than their experimental equivalents. 126

7.4 Literature values of the apparent density (ρ) and hardness (H_V) for PyCs, other carbon materials, and superhard carbides, nitrides, oxides, and phosphides, and their respective specific hardness *via* the H_V/ρ and H_V/ρ^2 design parameters. 129

7.5 Experimental and theoretical (from Eq. 7.6 and Eq. 7.7b) values of hardness (H_V) and apparent density (ρ_cmnc) of A-CMNCs as a function of the pyrolysis temperature (T_p), and the experimental specific hardness using the H_V/ρ and H_V/ρ^2 design parameters for comparison with other superhard materials. 131

A.1 Experimentally evaluated waviness amplitude (a) for A-CNT arrays a function of V_f. 148

A.2 Experimentally evaluated waviness wavelength (λ) for A-CNT arrays a function of V_f. 149

Abbreviations and Symbols

a-C	Amorphous carbon
A-CMNC	Aligned carbon nanotube carbon matrix nanocomposite
A-CNT	Aligned carbon nanotube
A-PNC	Aligned carbon nanotube polymer matrix nanocomposite
BSM	Bead and spring model
BWF	Breit-Wigner-Fano (band)
c−BN	Cubic boron nitride
C/C	Carbon fiber reinforced carbon
CM	Continuum modeling
CNT	Carbon nanotube
FEA	Finite element analysis
FTIR	Fourier transform infrared (spectroscopy)
HD	High density (pyrolytic carbon)
HRSEM	High resolution scanning electron microscopy
HRTEM	High resolution transmission electron microscopy
LD	Low density (pyrolytic carbon)
LJ	Lennard-Jones potential
MD	Molecular dynamics
MFFM	Mesoscopic force field model
MFP	Mean free path
MSM	Molecular structural model
NC	Nanocrystalline
NCM	Nano-scale continuum modeling
NF	Nanofiber

PyC	Pyrolytic carbon
RVE	Representative volume element
ta-C	Tetrahedral amorphous carbon
U-CNT	Unaligned carbon nanotube
vdW	Van der Waals interactions
XPS	X-ray photoelectron spectroscopy
XRD	X-ray diffraction
α	Shear coefficient of a carbon nanotube assuming hollow cylinder geometry, []
β_{002}	Full width at half maximum of the (002) peak in XRD, [°]
β_{100}	Full width at half maximum of the (100) peak in XRD, [°]
β_{110}	Full width at half maximum of the (110) peak in XRD, [°]
$\chi(w)$	Waviness dependent displacement parameter in directions perpendicular to carbon nanotube alignment direction, []
Δr	Average displacement perpendicular to wavy carbon nanotube alignment direction, [nm]
Δz	Average displacement along the wavy carbon nanotube alignment direction, [nm]
$\delta_\tau^{\text{helix}}$	Standard deviation of helical tortuosity, []
$\delta_\tau^{\sin}$	Standard deviation of sinusoidal tortuosity, []
$\delta_w^{\sin}$	Standard deviation of sinusoidal waviness ratio, []
Γ	Average inter-carbon nanotube spacing in aligned carbon nanotube arrays, [nm]
γ_{D}	Half width half maximum of the D-band in Raman Spectroscopy, [cm^{-1}]
$\gamma_{\text{G,a}-\text{C}}$	Half width half maximum of the amorphous carbon G-band in Raman Spectroscopy, [cm^{-1}]
γ_{G}	Half width half maximum of the G-band in Raman Spectroscopy, [cm^{-1}]
$\Gamma_{\max}$	Maximum inter-carbon nanotube spacing in aligned carbon nanotube arrays, [nm]
$\Gamma_{\min}$	Minimum inter-carbon nanotube spacing in aligned carbon nanotube arrays, [nm]
Λ	Scaling factor quantifying polymer infusion induced carbon nanotube waviness reduction, []
λ	Sinusoidal waviness wavelength, [nm]
λ_{xrd}	Wavelength of the incident x-ray radiation, [nm]
$\mathbb{R}$	Coefficient of determination, []
μ_τ^{helix}	Mean value of helical tortuosity, []

$\mu_{\tau}^{\sin}$	Mean value of sinusoidal tortuosity, []
$\mu_{w}^{\sin}$	Mean value of sinusoidal waviness ratio, []
ν	Poisson ratio, []
Ω	Waviness correction factor for aligned carbon nanotube arrays, []
ω	Raman shift, [cm^{-1}]
$\Omega_{\hexagon}$	Waviness correction factor for hexagonal packing, []
ω_{D}	Peak position of D-band in Raman Spectroscopy, [cm^{-1}]
ω_{G}	Peak position of G-band in Raman Spectroscopy, [cm^{-1}]
ω_{int}	Half width of the Raman integration regime, [cm^{-1}]
$\Omega_{\square}$	Waviness correction factor for square packing, []
ρ_{cnt}	Carbon nanotube intrinsic density, [$\mathrm{g/cm}^3$]
ρ_{g}	Density of single crystal graphene/graphite, [$\mathrm{g/cm}^3$]
ρ_{pyc}	Pyrolytic carbon apparent density, [$\mathrm{g/cm}^3$]
σ_{eff}	Effective electrical conductivity, [S/m]
θ_{100}	Position of the (002) peak in XRD, [°]
θ_{100}	Position of the (100) peak in XRD, [°]
θ_{110}	Position of the (110) peak in XRD, [°]
θ_{oa}	Graphitic crystallite orientation angle for PyC density model, [°]
θ_{th}	Theoretical orientation of graphitic crystallites for hardness estimation, [°]
$\theta_{\triangle}$	Isosceles angle of the constitutive triangles at each coordination number, [°]
τ	Tortuosity, also known as stochastic waviness, []
$\tau(w)_{\mathrm{helix}}$	Effective tortuosity evaluated *via* carbon nanotube waviness ratio assuming helical geometry, []
$\tau(w)_{\sin}$	Effective tortuosity evaluated *via* carbon nanotube waviness ratio assuming sinusoidal geometry, []
ξ_{bending}	Bending compliance contribution, [m/N]
$\xi_{\mathrm{extension}}$	Extension compliance contribution, [m/N]
ξ_{mode}	Compliance contribution of a deformation mechanism, [m/N]
ξ_{shear}	Shear compliance contribution, [m/N]
ξ_{torsion}	Torsion compliance contribution, [m/N]
ξ_{tot}	Total compliance contribution, [m/N]

$\zeta(w)$	Waviness dependent displacement parameter in the direction parallel to carbon nanotube alignment direction, []
A	Cross-sectional area of a carbon nanotube assuming hollow cylinder geometry, [nm^2]
A_{D}	Integrated intensity of the D-band in Raman Spectroscopy, [cm^{-1}]
A_{G}	Integrated intensity of the G-band in Raman Spectroscopy, [cm^{-1}]
C_{11}	In-plane tension/compression stiffness constant, [GPa]
C_{33}	Out-of-plane tension/compression stiffness constant, [GPa]
C_{44}	Inter-layer shear stiffness constant, [GPa]
D_{i}	Carbon nanotube inner diameter, [nm]
D_{o}	Carbon nanotube outer diameter, [nm]
E_{2D}	Two-dimensional graphene elastic modulus, [N/m]
E_{3D}	Three-dimensional graphene elastic modulus, [TPa]
$E_{\mathrm{cmnc}}(w)$	Waviness dependent effective longitudinal A-CMNC elastic modulus, [GPa]
E_{cm}	Pyrolytic carbon matrix effective elastic modulus, [GPa]
$E_{\mathrm{cnt}}(w)$	Waviness dependent effective longitudinal carbon nanotube array elastic modulus, [GPa]
E_{eff}	Effective elastic modulus, [GPa]
E_{pm}	Polymer matrix effective elastic modulus, [GPa]
$E_{\mathrm{pnc}}(w)$	Waviness dependent effective longitudinal A-PNC elastic modulus, [GPa]
G	Effective carbon nanotube shear modulus, [GPa]
$H_{\mathrm{V,th}}$	Theoretical pyrolytic carbon hardness, [GPa]
H_{V}	Vickers hardness, [GPa]
$hk\ell$	Miller indices, []
I	Area moment of inertia assuming hollow cylinder geometry, [nm^4]
$I(\omega)$	Raman intensity, [a.u.]
I_{D}	Intensity of the D-band in Raman Spectroscopy, [a.u.]
$I_{\mathrm{G,a-C}}$	Intensity of G-band of amorphous carbon in Raman Spectroscopy, [a.u.]
I_{G}	Intensity of the G-band in Raman Spectroscopy, [a.u.]
J	Polar moment of inertia assuming hollow cylinder geometry, [nm^4]
$K(w)$	Waviness dependent effective longitudinal carbon nanotube spring constant, [N/m]
k_{eff}	Effective thermal conductivity, [W/mK]

L_{1D}	Height of a carbon nanotube along alignment direction, [nm]
L_{3D}	True arc length of a carbon nanotube, [nm]
L_{a}	Graphitic crystallite size for the pyrolytic carbon matrix, [nm]
L_{c}	Graphitic crystallite thickness for the pyrolytic carbon matrix, [nm]
N	Effective two-dimensional coordination number for aligned carbon nanotubes, []
n	Number of carbon nanotubes, []
n_{xrd}	Constant for Bragg's law that determines reflection order, []
t_{hold}	Hold time at pyrolysis temperature for carbon matrix manufacturing, [min]
T_{p}	Pyrolyzation temperature, [°C]
V_{f}	Carbon nanotube volume fraction, [%]
w	Waviness ratio assuming sinusoidal function form, []
x	Direction perpendicular to the carbon nanotube alignment direction, []
Y	Theoretical effective longitudinal carbon nanotube Young's modulus, [TPa]
y	Direction perpendicular to the carbon nanotube alignment direction, []
z	Direction parallel to the carbon nanotube alignment direction, []

Chapter 1

Introduction

Current state of the art structural materials face a number of key challenges, and the use of nanofiber (NF) architectures with controlled morphology as structural elements could enable the design and manufacture of next-generation materials with enhanced performance and functionality. Some of the key capabilities that are desired in next-generation materials are summarized below. Many high value applications require multi-functional materials that are both lightweight, and incorporate power system elements, e.g. energy harvesting and storage. Another example is high value space applications, such as colonization and manned spaceflight for extended periods of time, require the development of better shielding materials, which would mitigate the greatest environmental risk to humans in space, radiation. These new advanced materials could be used to shield both astronauts and electronics from a wide variety of radiation species, such as electromagnetic, galactic cosmic, and solar cosmic radiation. Another important problem faced by aerospace structures is thermal management and protection, which requires lightweight and flexible materials with highly anisotropic thermal properties. These non-isotropic materials, which are scalable to large structures, could act as thermal insulators in one direction, and thermal conductors in another direction, thereby mitigating thermal hot spots and problems with thermal cracking. Many general transportation and vehicle applications also require their materials to have properties that are highly tailorable, while remaining multi-functional, lightweight, and providing improved damage tolerance. Finally, materials that are specifically designed to operate in extreme environments, which include heat, radiation, highly oxidizing environments, and both high and low pressures, are fundamental to many current industries, such as aerospace and nuclear power, and future industries, such as space mining and exploration. In summary, next-generation advanced materials will need to possess a high degree of multi-functionality, while being lightweight and highly resistant to their extreme operating environments. While materials that simultaneously fulfill all of these requirements do not currently exist, aligned NF based architectures, especially those comprised of carbon nanotubes (CNTs), could be engineered and tailored to exhibit all of these properties. In the remainder of this Chapter, the use of NF architectures to create the next-generation of structural materials is discussed, and the outline of the work pursued in this thesis is presented.

1.1 Aligned Carbon Nanotubes for Next-Generation Materials

The predicted (and sometimes realized) electrical,[1–4] thermal,[5–8] and mechanical properties of one dimensional nanoscale systems,[9–11] such as nanowires, nanofibers, and nanotubes, has motivated decades of research into their application in centimeter to meter-scale material solutions with widespread societal impact, e.g. microprocessors, medical devices, energy storage and harvesting devices, and high strength low density structural materials.[12–18] Due to their intrinsic elastic modulus $\gtrsim 1$ TPa ($\sim 2\times$ that of SiC and $5\times$ that of steel), theoretical intrinsic thermal conductivity > 1000 W/mK (potentially higher than that of diamond, and several times that of copper), and potential for superconductivity *via* ballistic electron transport, CNTs are one of the prime candidates for the design and manufacture of next-generation materials.[12] When organized into aligned CNT (A-CNT) arrays, the fabrication of highly scalable nanostructured architectures with tunable properties becomes possible.[12,18] To take full advantage of the exceptional and highly anisotropic intrinsic properties of NFs, especially CNTs, many recent studied focused on the use of A-CNTs in nanocomposite structures.[18–28] See Figure 1.1 for a specific modulus vs. specific strength (Figure 1.1a) and thermal conductivity vs. diameter (Figure 1.1b) plots demonstrating the potential performance enhancements that may result through integration of CNTs into composites. However, the properties reported by these previous studies were far lower than the properties predicted using current theory.[12]

Some of the main reasons why existing models cannot accurately predict the behavior of CNTs in scalable architectures, such as A-CNT arrays, are the various CNT morphology and proximity effects.[13,14,18,29] Non-idealities in morphology are one of the main reasons why the intrinsic properties of CNTs could only be attained in architectures comprised of a small number of CNTs,[30–33] where CNTs have ideal straight morphologies. In large assemblies, where the CNTs normally have non-ideal morphologies, effective CNT array properties up to three orders of magnitude lower than

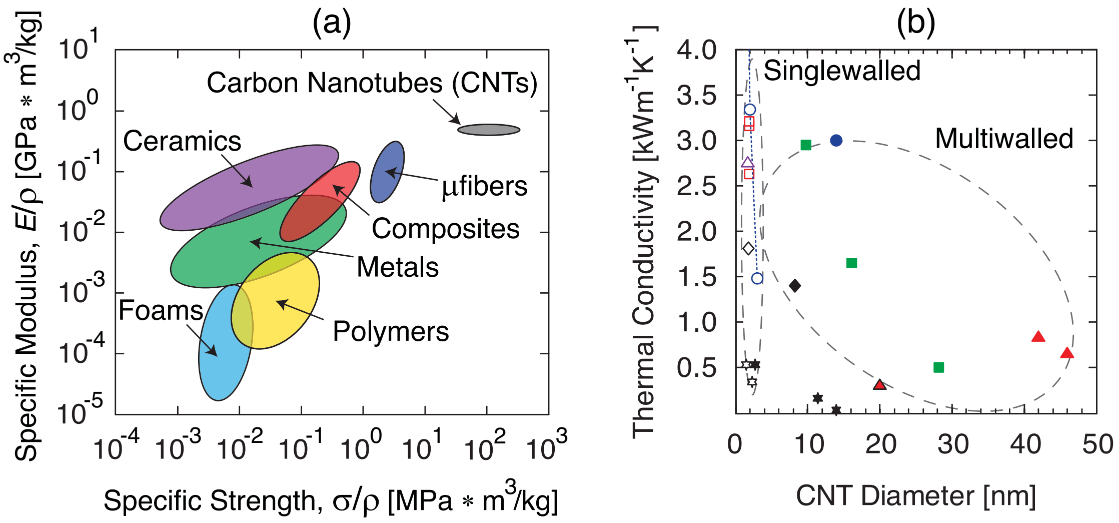

Figure 1.1: Reported mechanical and thermal properties of CNTs. (a) Specific modulus-specific strength plot comparing the properties of composite materials to other engineering materials, such CNTs. (b) Thermal properties of CNTs as a function of their diameter showing that their phonon transport properties are diminished as a function of their diameter based on the plot reported in Marconnet et al.[8] Since CNTs promise higher specific stiffness, specific strength, and phonon transport properties, many groups are currently working on their incorporation into composite architectures.

expected were observed.[29,34–40] See Figure 1.2 for a plot of the stiffness of CNT structures as a function of their size. This large discrepancy in the properties of CNTs in scalable structures, such as CNT arrays, originates from their complicated stochastic three-dimensional morphology and the local curvature, commonly known as waviness or tortuosity, that results from their synthesis process.[40–42] In this dissertation, theoretical and simulation tools that show how CNT waviness and proximity effects govern the behavior of CNT arrays and their composites are developed.

In this thesis, A-CNT arrays were grown in a 22 mm internal diameter quartz tube furnace at atmospheric pressure *via* a thermal catalytic chemical vapor deposition process, very similar to a previously described process,[19,22,43] with ethylene as the carbon source. The CNTs were grown on 10 mm $\times$ 10 mm Si substrates forming A-CNT arrays that are $\gtrsim 1$ mm tall, and are comprised of multiwalled CNTs that have an average outer diameter of ≈ 8 nm ($3-7$ walls[44] with an average inner diameter of ≈ 5 nm),[45] evaluated intrinsic CNT density of ≈ 1.7 g/cm^3,[28] average inter-CNT spacing of ≈ 80 nm, and corresponding volume fraction of $\sim 1\%$ CNTs.[43,45,46] See Chapter 4 for additional details about the morphology of the A-CNTs. The mechanical behavior of the CNTs was studied in both free-standing array form (see Chapter 5), and in A-CNT composite forms (see Chapters 6 and 7). This was achieved using a simulation framework capable of modeling $> 10^5$ CNTs with realistic 3D morphologies,[40–42] and using a previous analysis developed for

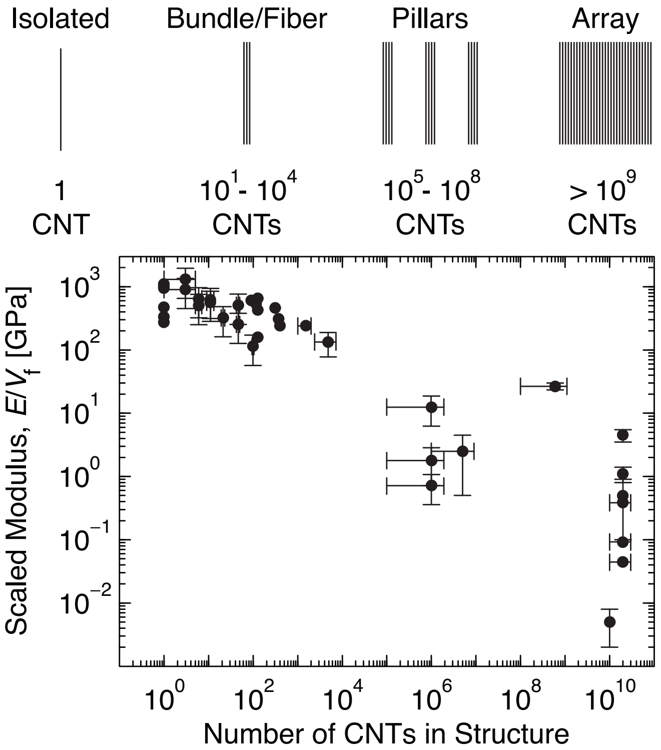

Figure 1.2: Reported stiffness for CNT systems as a function of their size, original to this thesis, reproduced from Stein, Lewis, and Wardle.[40] The plot shows how the elastic modulus (E), when normalized by the CNT volume fraction (V_f), scales with the number of CNTs enclosed in the structure demonstrating that isolated CNTs and CNT bundles/fibers exhibit $E/V_\mathrm{f} > 100$ GPa,[30–35] whereas larger scale CNT pillars and arrays exhibit $E/V_\mathrm{f} \lessapprox 1$ GPa.[29,36–39]

the mechanical behavior of carbon nanocoils.[47] Since A-CNT architectures could pave the road to next-generation material architectures with exceptional properties, but their desired properties could not be attained in previous work, this thesis focuses on studying the origin of the orders of magnitude over-prediction of the A-CNT composite properties from the underlying physics, and recommending future paths of study that could minimize such performance unpredictability.

1.2 Thesis Outline

In this dissertation, the evolution of the CNT morphology as a function of packing proximity is evaluated, and the influence of CNT morphology on the mechanical properties of A-CNT arrays and their composites is quantified. These findings are used to elucidate the physical mechanisms that lead to stiffness losses in A-CNT structures, and to recommend future paths of study that would enable better tuning and prediction of the 3D elastic constitutive relations of A-CNT arrays and

A-CNT based composites with a variety of matrix chemistries and nano-structures.

In Chapter 2, an overview of previously synthesized A-CNT architectures and their observed properties is presented, followed by a discussion of the shortcomings of these current generation materials including their possible physical origin, and the previous ways these limitations were overcome. Next, the work that motivated and enabled the development of the theoretical and simulation tools presented here are discussed, and the ways these tools can be used to better predict and understand the behavior of A-CNT architectures is outlined.

In Chapter 3, the objectives of this dissertation are articulated, and the general approach employed for understanding and predicting the mechanical behavior of A-CNT arrays and their composites is described.

In Chapter 4, the developed multi-scale simulation framework is described in detail, and is used to describe the evolution of the packing morphology of CNTs, *via* their effective two-dimensional coordination number, as a function of their volume fraction (V_f). These findings are used to quantitatively describe the morphology of the CNTs in three-dimensions, and to recommend future areas of study that would enable more precise modeling of the self-organization of CNTs during the growth process leading to less uniform (more bundled), and thereby more representative, local V_f.

In Chapter 5, the simulation framework, along with a previously reported mechanical model that was originally developed for carbon nanocoils, is used to predict the effective stiffness of the CNTs that comprise A-CNTs arrays as a function of the four deformation mechanisms: extension, shear, bending, and torsion. Using previously reported nanoindentation data measured for A-CNTs for V_f ranging from $\sim 1-20\%$, the deformation mode that dominates the elastic response of A-CNT arrays is identified, and the observed orders of magnitude enhancement in A-CNT array modulus is explained more robustly. These findings are used to quantify the impact of the shear modulus of the A-CNTs on their performance as reinforcing agents, and to recommend further experimental, theoretical, and simulation work that will enable robust prediction of the mechanical behavior of A-CNTs during deformation without ignoring or assuming an overly simplistic CNT-CNT interaction potential.

In Chapter 6, the simulation framework is applied to A-CNT polymer matrix nanocomposites (A-PNCs), and is used to predict their effective stiffness assuming that the polymeric matrix prevents the free movement of the CNTs, and thereby eliminates the torsion deformation mode. Using previously reported uniaxial tension and nanoindentation data measured for A-PNCs at V_f ranging from $\sim 1-20\%$, the impact of the ratio of the CNT longitudinal modulus and polymer matrix modulus is quantified, and the lower than expected enhancement of the effective longitudinal modulus of the A-PNCs is explained in detail. These findings are used to approximate the three-dimensional elastic constitutive relations of A-PNCs, and to recommend further experimental and computational work that will enable representative prediction of the performance of A-PNC layers in macroscopic hybrid material architectures where interfacial phenomena dominate the mechanical behavior.

In Chapter 7, the structure-property relations of the carbon matrix for A-CNT carbon matrix nanocomposites (A-CMNCs) manufactured using industry compatible polymer derived-ceramics processing is presented. Using the simulation framework, the effective stiffness of A-CMNCs is predicted for V_f ranging from $\sim 1-20\%$, and is compared to the experimentally evaluated mechanical properties of A-CMNCs attained using Vickers microhardness, and previously reported literature values for A-CMNCs. These findings are used to compare the A-CMNCs to a variety of other reference engineering materials, and to recommend paths of study that would enable manufacture of A-CMNC with enhanced and precisely predictable mechanical behavior.

In Chapter 8, the important findings of this dissertation are summarized and perspectives on these discoveries are provided. Next, recommendations for future studies in the areas of A-CNT nanocomposite synthesis and processing, morphology characterization and modeling, and material property testing and prediction are made.

Chapter 2

Background

Aligned NF architectures have tremendous potential for many high value applications, especially where low density and high multi-functionality are a necessity. However, the widespread adoption of such materials, especially as A-CNTs, is hindered by the performance limitations of their current generation nanocomposites. A-CNTs are the most well-studied aligned NF architecture. These limitations include orders of magnitude lower than predicted stiffness, and underwhelming thermal and electrical properties. To design next-generation material architectures that achieve the full potential of CNTs, the morphological (meso-scale) origins of these problems first need to be understood. The next Section contains an overview of current generation A-CNT materials with a focus on the attainable physical properties, and the likely physical origins of the underwhelming performance of these A-CNT systems are discussed. In the next Section, the multi-scale theoretical and simulation tools recently developed to better predict the behavior of these materials are introduced, and the challenges that limit the accuracy of property prediction are discussed. In the remainder of this Chapter, the previous overly-simplistic assumptions that need to be revisited are outlined, and the road-map for the development, and eventual coupling into a unified multi-scale framework, of simulations that could address these issues at each of their respective length-scales is presented.

The purpose of this Chapter is to provide the general background necessary for understanding the overall motivation and state of the art for the work performed in this dissertation. To make sure that the presented work can be understood fully, subsequent Chapters will provide additional detailed background information when necessary.

2.1 Overview of A-CNT Physical Properties

While there a variety of CNT physical properties that can be exploited in materials design, this section will focus on the three most commonly studied A-CNT properties: electrical, thermal, and mechanical. In this Section, the properties of a selection of previously produced A-CNT architectures, that include both pure A-CNT systems and A-CNT nanocomposites, are explored, and their performance, which is a function of the underlying CNTs, is evaluated.

The most common measure of electron transport efficacy in A-CNT systems is the effective electrical conductivity (σ_{eff}). Early work on idealized (singlewalled) CNTs predicted their σ_{eff} along the CNT length to exceed 10^8 S/m at room temperature,[54] but such a figure could not be realized in A-CNT systems, e.g. A-CNT arrays and A-PNCs,[20,48–53] especially when the CNTs are comprised of multiple walls. Some of the best recent studies have reported that their A-CNT systems exhibit axial $\sigma_{\text{eff}} \sim 10^4 - 10^5$ S/m,[48,52,53] which are orders of magnitude lower than expected. See Figure 2.1 for a plot of the previously reported axial σ_{eff} values as a function of the V_f of the CNT system.[48] This large difference originates from CNT non-idealities that are characterized at two different length-scales: atomic structure (nano-scale $\rightarrow \lesssim 1$ nm) and morphology (meso-scale $\rightarrow 10 - 100$ nm).

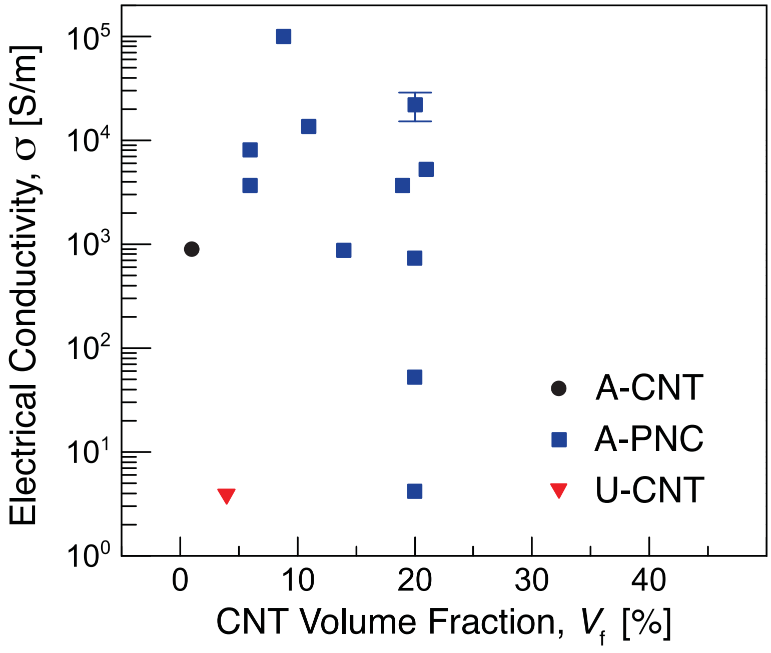

Figure 2.1: Scaling of electrical conductivity (σ_{eff}) as a function of the CNT volume fraction (V_f) for unaligned CNTs (U-CNTs),[48] A-CNTs,[49] and A-PNCs,[20,48,50–53] showing that the σ_{eff} previously reported for CNT systems is lower than the $\sigma > 10^8$ S/m figure predicted by theory at room temperature.

Atomic structural factors that can hinder electron transport in CNTs include vacancies and Stone-Wales defects,[55–57] which are known electron scattering sites in graphitic materials,[58–61] but are native to CNTs synthesized using scalable techniques, e.g. CVD.[46,62] These structural defects in CNTs can also lead to the (exohedral) adsorption of ambient humidity onto the CNT walls,[46,57] which could further diminish electron transport along the CNT length through the Poole-Frenkel conduction mechanism,[63–66] and may also increase the CNT-CNT junction resistance,[67,68] which plays a key role in the transport of electrons in A-CNT arrays and their composites.[69–71] Also, due to the fluctuation of CNT-CNT interactions during the CNT synthesis process,[72,73] many A-CNT arrays have very high degrees of local curvature on the meso-scale,[74] and such curvature is associated with band gaps that hinder electron transport along the tube.[75,76] Therefore, to avoid large over-predictions of the electron transport properties in A-CNT based materials, theoretical and simulation frameworks must accurately model the CNTs in the nano- and meso-scales, and the common assumptions of pristine CNTs with perfectly straight and collimated morphologies should be used with the utmost care.

Phonon transport in A-CNTs is normally quantified using their effective thermal conductivity (k_{eff}). Early theoretical studies on pristine singlewalled CNTs predicted that these 1D nanomaterials can exhibit effective k_{eff} that exceeds 3000 W/mK parallel to the CNT length at room temperature,[77–79] however these values of k_{eff} could not be attained in A-CNT systems.[12,80,81] The best figures for the axial k_{eff} reported in recent experimental and theoretical studies for A-CNT systems comprised of $> 10^3$ CNTs are on the order of ~ 100 W/mK,[19,81] which is more than $10\times$ lower than predicted by theory, and cannot be accounted for by the variations in k_{eff} induced by differences in CNT length,[82] defect density,[83] and number of walls.[84] See Figure 2.2 for a plot of the k_{eff} values previously reported for CNTs, graphene, and other carbon allotropes, and how k_{eff} scales with the size and mean free path (MFP) of graphene, as presented by Pop et al.[85] Similar to electron transport, this underwhelming phonon transport performance of A-CNT architectures originates from CNT non-idealities at two different length-scales: $\lesssim 1$ nm scale, and $10 - 100$ nm scale, i.e. meso-scale. At the $\lesssim 1$ nm scale, defects such as divacancies, inter-layer bonds, and Stone-Wales defects lead to phonon scattering both for acoustic and optical phonons and heat carrying electrons,[60,85–90] thereby limiting heat transport and diminishing k_{eff} of CNTs that exhibit these structural defects by up to $100\times$.[90–92] At the $10 - 100$ nm scale, CNT edge/surface roughness (e.g. local variation in the CNT diameter) and curvature lead to acoustic phonon scattering,[93–95] which may not be a dramatic effect in CNTs that are longer than the phonon mean free path,[96–98]

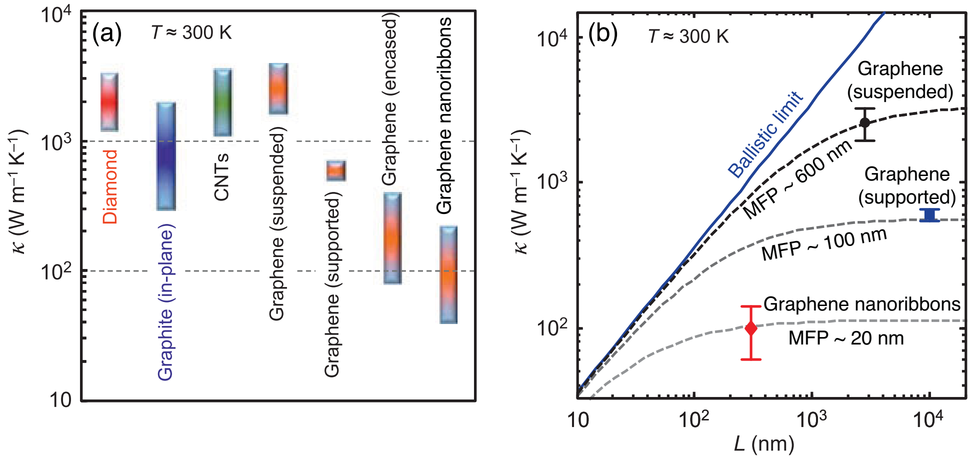

Figure 2.2: Thermal properties of CNTs, graphene, and other carbon allotropes at room temperature as presented by Pop et al.[85] (a) Plot summarizing the thermal conductivity (k_{eff}) values of CNTs, graphene, graphite, and diamond illustrating that suspended graphene, CNTs, and diamond can achieve $k \sim 3000$ W/mK. (b) k_{eff} as a function of the phonon MFP showing that suspended graphene achieves the highest k_{eff} value because it has the longest MFP ($\sim$ 600 nm).[85]

but may diminish the CNT energy carrying capacity.[60,85,99] Such phonon scattering strongly affects heat transport in CNTs because, unlike other electrically conductive nanomaterials, acoustic phonons are the dominant heat carrier in graphene and CNTs,[99,100] and their conductance governs k_{eff}. Therefore, to minimize the over-predictions of the thermal transport efficacy of A-CNT based materials, the development of multi-scale simulation frameworks that can account for the CNT non-idealities on the $\lesssim 1$ nm and $10 - 100$ nm scales is required, and is an important area of study that may enhance material property prediction capabilities.

Mechanical behavior of A-CNTs is normally quantified using their effective elastic modulus (E_{eff}). The E_{eff} for pristine CNTs systems parallel to the CNT length is normally assumed to be of similar magnitude as the in-plane E_{eff} of the graphitic crystallites that comprise highly ordered pyrolytic graphite, where $E_{\mathrm{eff}} \sim 1$ TPa.[3,12,101] However, as discussed in Chapter 1, the best figures of the axial E_{eff} recently reported for CVD grown large-scale A-CNT systems, i.e. $> 10^6$ CNTs, are on the order of $\sim 1 - 1000$ MPa,[29,36–39] which is more than three orders of magnitude lower than expected.[40,102] The dramatically diminished stiffness of A-CNT architectures originates from two mechanisms: in-plane and out-of-plane defect-mediated intrinsic CNT stiffness losses; and CNT morphology governed deformation mode, e.g. extension, shear, bending, and torsion, contribution to the CNT effective stiffness. In-plane defects, such as vacancies and Hackelite defects and 'grain boundaries', and out-of-plane defects, such as inter-layer bonds, are known to enhance the compliance of CNTs both along their alignment direction,[103–111] and radial direction,[112] while enhancing their inter-layer shear moduli.[113] As discussed earlier, these defects are inevitable for CVD grown CNTs, especially multiwalled CNTs, but previous work indicates that their presence should not lead to stiffness losses that exceed 50% of the original value of E_{eff} ($\rightarrow\sim$ 0.5 TPa),[104–109] and recent work on graphene indicates that controlled introduction of defects may actually enhance E_{eff} by up to $2\times$.[109,114,115] See Figure 2.3 for the scaling of the two-dimensional ($E_{2\text{D}}$) and three-dimensional ($E_{3\text{D}}$) E_{eff} of graphene as a function of the defect density showing this effect as presented by López-Polín et al.[114] Morphology activation of the shear and torsion deformation modes, which are dominated by the low intrinsic shear modulus (G) of CNTs that can have a value similar to the transverse shear modulus of turbostratically stacked graphene/graphite,[116,117] i.e. 0.1 GPa $\lesssim G \lesssim$ 1 GPa,[118,119] can lead to orders of magnitude losses in the CNT effective stiffness.[40,42,102] Since even the most well-aligned A-CNTs previously reported in the literature, e.g. 'super-aligned' A-CNTs,[120–123] do have some non-negligible degree of tortuosity, these CNT morphology mediated losses require creativity to overcome, and recent work on CNT densification shows that CNT proximity interactions at higher V_{f} can diminish the local curvature in CNTs, and effectively limit the contribution of the shear and torsion deformation modes to the effective E_{eff}. Therefore, to enable reliable prediction of the mechanical behavior of A-CNT systems, representative measures of the three-dimensional morphology of CNTs and the nature and concentration of their native wall

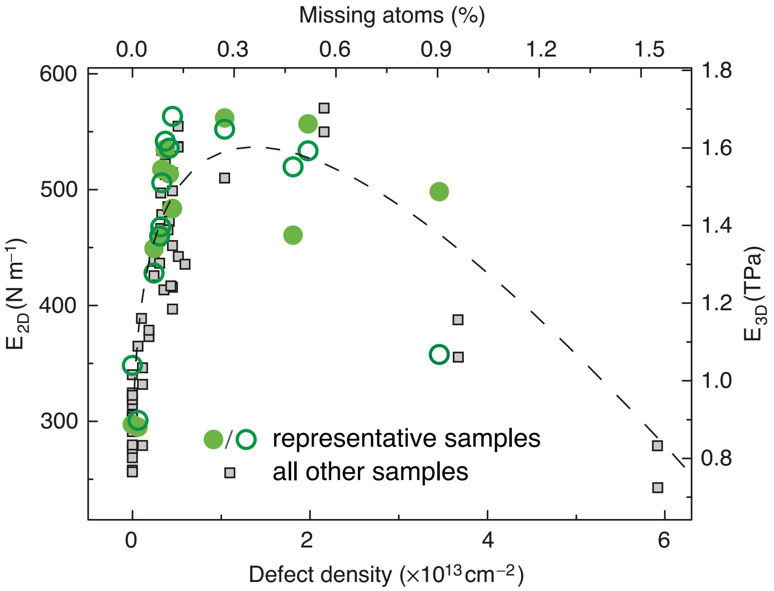

Figure 2.3: Scaling of the 2D modulus ($E_{2\text{D}}$) and 3D modulus ($E_{3\text{D}}$) of graphene as a function of the defect density as presented by López-Polín et al.[114] This plot shows that carefully tuning the defect density can enhance the mechanical properties of graphene, whereas $>1\%$ missing atoms in graphene will lead to diminished stiffness.[114,115]

defects must be integrated into theoretical and simulation frameworks.

This Section presented the currently attainable electrical, thermal, and mechanical properties of A-CNT architectures, and the physical origin of their far from anticipated performance. In addition, we will consider nanocmposites comprised of A-CNTs in this thesis. The literature on A-CNT based nanocomposites is nearly vanishingly small and is used in the discussion of the relevant sections in Chapters 6 and 7. In the next Section, existing state-of-the-art multi-scale modeling and simulation tools will be reviewed, and how they currently model CNTs to better account for their complex underlying physical phenomena will be discussed.

2.2 State-of-the-Art Multi-scale Modeling and Simulation Techniques

Since representative modeling of the behavior of CNT based architectures requires solving two sets of governing equations, i.e. quantum/atomistic mechanics equations of state in $\lesssim 1$ nm scale and the classical/continuum mechanics equations of state at the meso-scale, many recent theoretical and simulation frameworks have embraced multi-scale approaches to account for all the underlying physics. In this Section, two emerging multi-scale modeling techniques that have garnered much interest in recent years will be presented, and they include hybrid atomistic/continuum techniques and meso-scale frameworks. Although this Section will mainly explore the application of these techniques to the mechanical behavior of A-CNT systems, since this dissertation focuses on the mechanical property prediction of A-CNT based materials, extension of these techniques to enable prediction of the A-CNT phonon and electron transport properties makes these techniques important in general to the future application of A-CNT materials in high value industrial applications.

Hybrid simulations of atomistic and continuum modeling methods have the potential to offer the best of both worlds: true quantum mechanical treatment of phenomena that occur at the ~ 1 nm scale, and classical treatment of phenomena that occur at the ~ 1 μm scale and above. This hybrid approach is commonly utilized for A-CNT composites, and works by treating the representative volume element (RVE) around the CNTs, which includes the C atoms that comprise the CNTs and the (polymer) matrix region close to the CNT surface known as the 'interphase' region, using an atomistic technique such as molecular dynamics (MD), while the rest of the matrix is modeled using a continuum modeling (CM) technique, such as micromechanics, utilizing either an analytical or finite element analysis (FEA).[126–130] However, these hybrid techniques are limited by the large computational expense of the atomistic simulation,[131] and also require several simplifications to model a complex structure such a CNT.[124] To overcome this challenge, more recent studies have developed nano-scale CM (NCM) techniques that replace the C−C bond with a continuum element.[128] The most common way this is achieved is by treating the C−C bond as a structural member with properties obtained by atomistic modeling, which is commonly known as the molecular structural model (MSM).[128,132,133] See Figure 2.4 for an illustration of how the MSM approach treats the C−C bond as an effective structural element as presented by Eberhardt and Wallmersperger.[124] Through recent extensions and improvements of the original MSM approaches,[124,134–137] such as improving the underlying chemical force field description to ensure consistency in terms of energy,[124] the NCM approach was shown to be an effective compromise between atomistic and continuum techniques. This analysis was successfully utilized to model CNTs containing a few simple kinds of wall defects.[128] However, while NCM and hybrid atomistic-continuum simulations are promising, they cannot accurately replicate the morphology of CNTs, whose contribution to the observed stiffness losses in A-CNT systems far eclipses the contribution of structural defects, and explains why

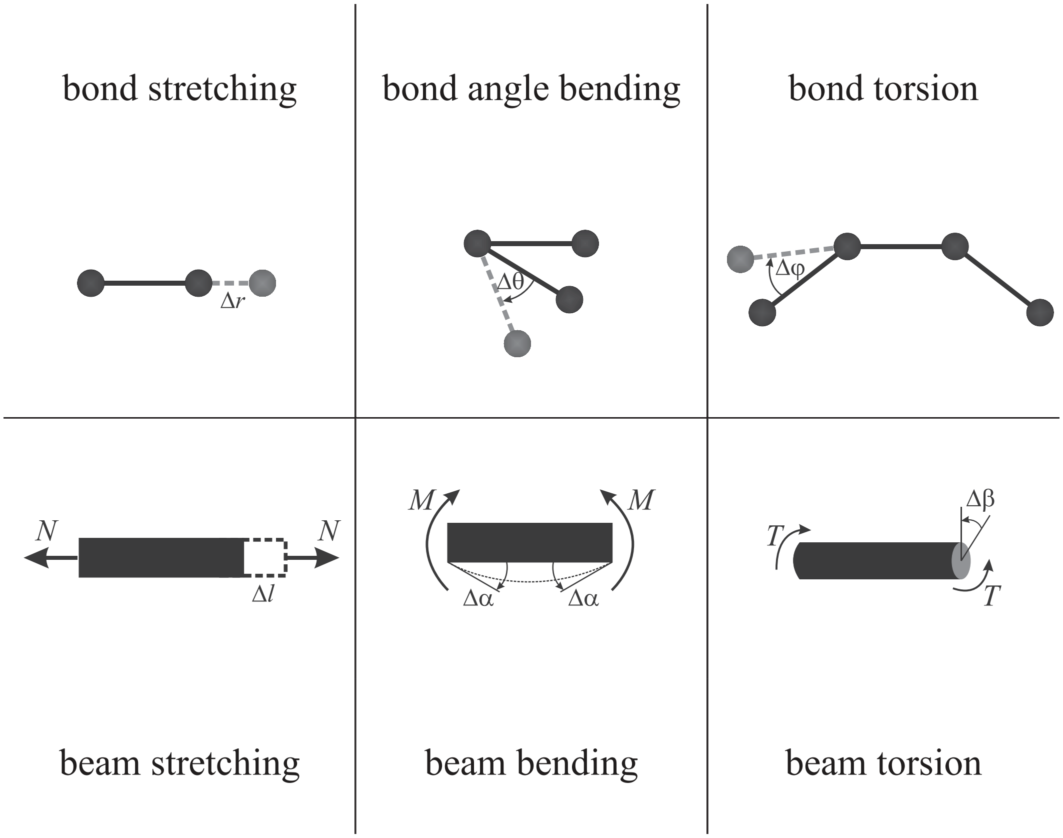

Figure 2.4: Illustration showing the treatment of the C−C bond as an effective structural element by the MSM approach as presented by Eberhardt and Wallmersperger.[124]

most of these techniques yield predictions of 0.4 TPa $\leq E_{\mathrm{cnt},\|} \leq$ 3.0 TPa, which are still at least 3 orders of magnitude greater than experimental data.[128]

Coarse-grained meso-scale simulations promise the ability to simultaneously account for inter-CNT interactions while reproducing the experimentally observed CNT morphology.[138] This is normally achieved by discretizing the CNTs that comprise the A-CNT arrays in two ways: (1) by representing the CNTs as a collection of point masses connected by linear springs, commonly known as the bead and spring model (BSM);[125,138–147] and (2) by describing the motion of a CNT with respect to the dynamics of nodal point masses that are connected by flexible cylinders, commonly known as the mesoscopic force field model (MFFM).[91,94,144,148–153] Both of these techniques are able to account for the electrostatic interactions of the CNTs *via* an analytical potential, such as the common 12-6 Lennard-Jones (LJ) potential.[91,94,125,138,139,141–153] See Figure 2.5 for a schematic illustrating the atom-scale, nm-scale, and meso-scale treatment of a CNT as presented by Cranford and Buehler.[125] Recent work on coarse-grained simulations of CNTs have had much success in re-producing their self-organization where bundles form,[91,94,138,141–143,146,147,149–152] e.g. during the growth process or during mechanical manipulation,[138,141–143,147] and their mechanical deformation as a result of an applied stimuli,[138,141–143,146,147] such as load applied *via* a

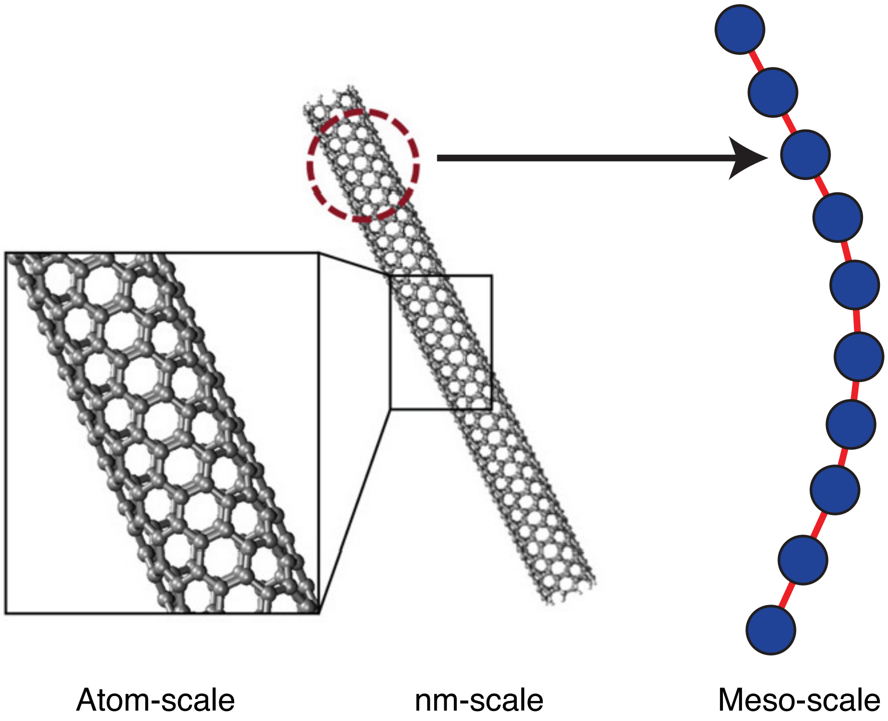

Figure 2.5: Illustration of the atomistic and corresponding mesoscopic treatment of a CNT as presented by Cranford and Buehler.[125]

nanoindentor.[138] However, these meso-scale techniques are not particularly well-suited to account for atomic-scale defects,[138] such as Stone-Wales or Hackelite defects, and waviness that is not of simple function form,[154] both of which could be native to the tortuous CNTs that are modeled *via* the mesoscopic approximation.[40–42,46] Also, these models assume that electrostatic interactions within the mesoscopically discretized CNTs are uniform and of simple analytical form, e.g. the LJ potential normally used to model van der Waals (vdW) interactions.[91,94,125,138,139,141–153] However, the CNT-CNT electrostatic interactions may not be purely vdW in nature in CNTs with native wall defects and adsorbed gas species,[40–42,46] which means that this coarse-grained meso-scale is best used for single-walled CNTs with low defect concentrations. Since these techniques could enable the modeling of CNTs with realistic morphologies, but information on the three-dimensional morphology of A-CNTs was not available until very recently,[155–157] very little is currently known about how the three-dimensional morphology of A-CNTs relates to their mechanical behavior, and other physical properties, but these meso-scale techniques offer a promising methodology to achieve property prediction in A-CNT systems comprised of CNTs with non-reducible stochastic wavy morphologies.

This Section presented the current state-of-the-art techniques to approximate the CNTs that comprise A-CNT arrays, and simulate their mechanical behavior. In the next Section, the limitations that hinder the property prediction capabilities of these existing techniques will be reviewed, their origin from the assumptions currently employed to model the CNTs that comprise A-CNT architectures will be presented, and the course of study necessary for future work to simplify and overcome these challenges will be proposed.

2.3 The Path Toward More Accurate Property Prediction Tools

Although Sections 2.1 and 2.2 discussed in detail the two main kinds of non-idealities that exist in CNTs and how they influence the physical properties, and therefore performance, of A-CNT systems, these factors cannot be integrated into the current generation theoretical and simulation frameworks that underpin material property prediction toolboxes. To make up for these shortcomings of current generation models, a number of simplifying assumptions are made, and the major ones focusing on modulus prediction include:

- ▷ The CNT bonding character is pristine and contains no defects such as vacancies, Stone-Wales/dislocations, and out-of-plane bonds.

▷ The CNT geometry/structure can be adequately modeled using a cylinder with effective parameters, e.g. effective wall thickness, that unify continuum and atomistic predictions.

▷ The interactions of the CNT walls, e.g. inter-layer load transfer, are very small relative to the CNT intrinsic contributions, and can be neglected altogether.

▷ The CNT morphology can be approximated using a simple functional form, e.g. perfectly straight 'collimated' morphology or sinusoidal/helical 'wavy' morphology.

▷ Inter-CNT interactions can be represented using highly idealized analytical potentials, such as the 12-6 LJ potential.

While eliminating all of these assumptions will take significant effort, and is currently not possible, recently available data can enable the development of multi-scale simulations that could address these issues at each of their respective length-scales. To achieve this, an array of simulations that work on the following characteristic length-scales need to be developed and coupled:

▷ < 1 nm scale: MD simulation that models the many-body interaction (covalent and electrostatic) of atoms both in regular hexagonal structures, out-of-plane bonds, divacancies, hackelite defect loops, and Stone-Wales dislocations.

▷ $1 - 10$ nm scale: NCM simulation that models the effective interactions of pristine and defective regions within the CNTs.

▷ $10 - 10^3$ nm scale: coarse-grained meso-scale simulation that re-produces the 3D stochastic morphology of real CNTs that comprise A-CNT arrays and assembles the NCM/MD regions in real 3D space. This simulation, in combination with the MD simulation, should be used to evaluate the inter-CNT interactions within the A-CNT systems.

▷ $> 10^3$ nm scale: CM modeling that utilizes the generated 'wavy' A-CNT arrays to predict the behavior of A-CNT systems comprised of $> 10^5$ CNTs.

Since MD simulations that are capable of efficiently modeling the behavior of defective CNT regions are currently in their infancy, effectively accounting for the true structure and many-body interactions within CNTs remains a challenge. Also, since properly accounting for the defective regions is not currently possible, representative NCM simulation of the forces that exist within CNTs poses an additional challenge. Additionally, since the mechanical behavior of A-CNT systems is dramatically influenced by their non-idealities on the $10-10^3$ nm scale, but effective ways to account for the stochastic three-dimensional CNT morphology do not currently exist, this dissertation will focus on overcoming this challenge *via* the development of a coarse-grained meso-scale simulation that accurately re-produces the experimentally observed CNT morphology (see Chapter 4 for details), and the coupling of the generated 'wavy' A-CNT arrays to a CM model to efficiently predict the mechanical behavior of A-CNT arrays (see Chapter 5) and A-CNT based polymer- and carbon-matrix nanocomposites (see Chapters 6 and 7).

2.4 Conclusions

In this Chapter, the known electrical, thermal, and mechanical properties of A-CNT based systems were presented, and the physical origins of their underwhelming performance in macroscopic material structures were established. The current state-of-the-art property prediction tools that have the potential to account for these non-idealities and direct further work with the end goal of synthesizing A-CNT based materials with enhanced properties were reviewed, and the limitations of these models and future paths of study that could help overcome these challenges were discussed. In the next Section, the objectives of this thesis are outlined, and a framework for meeting these objectives, informed by the works discussed in this Section, is presented.

Chapter 3

Objectives and Approach

To realize A-CNT architectures with tunable anisotropic physical properties for next-generation material applications, the evolution of the three-dimensional CNT morphology as a function of processing must be understood. Additionally, to enable accurate prediction of the mechanical behavior of A-CNT systems, a clear understanding of the effects of CNT morphology on the compliance contribution of the CNT deformation mechanisms must be developed.

3.1 Objectives

The objectives of this dissertation are to gain insight into the effects of CNT atomistic structure and morphology on the performance of A-CNT arrays and their nanocomposites. This required the development of several key theoretical models and simulation frameworks to help understand the implications of the experimental results, and to gain more insight into the general behavior of A-CNTs and materials comprised of A-CNTs.

3.2 General Approach

This dissertation can be organized into two primary areas of investigation: quantification and simulation of the evolution of the three-dimensional packing morphology of A-CNTs as a function of their V_f; and mechanical property characterization, modeling, and prediction for A-CNT arrays, A-PNCs, and A-CMNCs. The strategies used in each stage, their limitations, and the origin of their limitations are outlined in the remainder of this Chapter, and the results of the work outlined here can be found in subsequent Chapters.

3.2.1 Three-dimensional Morphology of A-CNTs

The A-CNT morphology study focused on quantifying the evolution of the CNT waviness as a function of packing proximity, which is controlled *via* the V_f (at a range of 1 vol. % CNTs $\leq V_\mathrm{f} \leq$ 20 vol. % CNTs), and modeling the packing structure of A-CNT systems in a highly scalable simulation capable of studying $> 10^5$ CNTs with realistic stochastic morphologies. Through the course of this thesis, the ability to model and describe A-CNT arrays transitioned from deterministic fits to analytic expressions (such as sinusoudal waviness) to a stochastic description. This study required quantification and analysis of the A-CNT morphology using experiments, theory, and simulation, (see Chapter 4 for more details) and each approach includes the following elements:

Experimental: evolution of waviness with V_f

- ▷ Evaluation of the deterministic waviness ratio (w) assuming a sinusoidal functional form *via* cross-sectional high resolution scanning electron microscopy (HRSEM) of A-CNT arrays at 1 vol. % CNTs $\leq V_\mathrm{f} \leq$ 20 vol. % CNTs.
- ▷ Conversion of deterministic waviness (w) into stochastic waviness, known as the tortuosity (τ) using both sinusoidal and helical functional forms.

Theory: waviness-corrected morphology

- ▷ Evaluation of deterministic waviness correction factor for square ($\Omega_\square$) and hexagonal ($\Omega_\hexagon$) packing of aligned NF arrays as a function of w.
- ▷ Modeling of the deterministic waviness correction factor for A-CNT arrays (Ω) as a function of V_f and the inter-CNT spacing (Γ).
- ▷ Calculation of the effective two-dimensional coordination number (N) for A-CNTs with stochastic wavy morphologies.

Simulation: A-CNT arrays with stochastic three-dimensional morphology

- ▷ Development of meso-scale technique to replicate the effective two-dimensional random walk transverse to the CNT alignment direction (i.e. $x-y$ plane) that gives rise to the stochastic wavy morphology during A-CNT growth, with appropriate discretization of the A-CNTs along their alignment direction (i.e. z direction).
- ▷ Evaluation of the average $x-y$ (Δr) and z ($\rightarrow \Delta z$) displacements.

- ▷ Calculate the average arc length of each CNT in the array ($\equiv \tau$), and iteratively adjust Δz until τ for the A-CNT array matches the experimentally evaluated stochastic waviness assuming sinusoidal function form ($\rightarrow \tau(w)_{\text{sin}}$).
- ▷ Definition of a characteristic unit cell used to model the CNT waviness, and evaluation of non-dimensional coefficients that connect the stochastic Δr and Δz used to model the three-dimensional CNT morphology to the deterministic w evaluated from experiments.

The simulated array of wavy A-CNTs, whose three-dimensional morphology closely resembles the packing structure of experimentally observed A-CNTs, is then used to quantify the compliance contribution of the four modes of deformation that can occur in wavy CNTs, following a previous analysis on carbon nanocoils: extension, shear, bending, and torsion. These compliance contributions are then used to predict the mechanical behavior of A-CNT systems, as detailed in Section 3.2.2. CNT-CNT interaction effects are not explicitly modeled but are captured implicitly at higher packing fractions (see discussion in Section 3.2.3).

3.2.2 Mechanical Property Prediction for A-CNT Systems

Since the mechanical properties of A-CNT composites are strongly influenced by the elastic behavior of the underlying A-CNT arrays, the property prediction study began with A-CNT arrays that have no matrix material in the inter-CNT region (see Chapter 5), was extended to A-PNCs that have a thermoset epoxy polymeric matrix that is not affected by CNT packing (see Chapter 6), and concluded with A-CMNCs that have a pyrolytic carbon (PyC) matrix that evolves with CNT proximity (see Chapter 7). Mechanical property predictions for each of these materials required slightly different model inputs, sets of assumptions, and experimental data for validation, as detailed here:

A-CNTs: effective array stiffness for non-interacting CNTs

- ▷ The extension, shear, bending, and torsion mechanisms are all assumed to be active, and the combination of their contribution yields the effective spring constant of the CNTs as a function of w ($\rightarrow K(w)$).
- ▷ The intrinsic Young's modulus of CNTs (Y) has a value of $Y \sim 1$ TPa, whereas G for CNTs has a value of $G \sim 1$ GPa.
- ▷ The A-CNT array effective modulus as a function of w ($\rightarrow E_{\text{cnt}}(w)$) is also a function of V_{f}, since w evolves with V_{f}.

- ▷ Predicted $E_{\text{cnt}}(w)$ results are compared to previously reported E values for A-CNTs measured using nanoindentation (Ref. 29), and the value of G is used to analyze the E scaling previously reported by Ref. 29.

A-PNCs: effective nanocomposite stiffness *via* rule of mixtures for constant elastic modulus of the polymer matrix (E_{pm})

- ▷ The extension, shear, and bending mechanisms are all assumed to be active, while torsion is assumed to be eliminated by the polymer matrix, and the combination of their contribution yields $K(w)$.
- ▷ Y for CNTs has a value of $Y \sim 1$ TPa, whereas G for CNTs has a value of $G \sim 1$ GPa when $G \geq E_{\text{pm}}$, and $G \approx E_{\text{pm}}$ when $G < E_{\text{pm}}$.
- ▷ The A-PNC effective modulus as a function of w ($\rightarrow E_{\text{pnc}}(w)$) is approximated *via* rule of mixtures of $E_{\text{cnt}}(w)$ and E_{pm}.
- ▷ Predicted $E_{\text{pnc}}(w)$ results are compared to previously reported E values for A-PNCs measured using nanoindentation (Ref. 50) and tensile tests (Ref. 158), and a factor that quantifies the reduction in w as a result of polymer infusion (Λ) is used to analyze the previously reported E scaling from Ref. 50 and Ref. 158.

A-CMNCs: effective nanocomposite stiffness *via* rule of mixtures for evolving elastic modulus of the PyC matrix (E_{cm})

- ▷ The extension, shear, and bending mechanisms are all assumed to be active, while torsion is assumed to be eliminated by the PyC matrix, and the combination of their contribution yields $K(w)$.
- ▷ E_{cm} is modeled using the size (L_{a}) and thickness (L_{c}) of the graphitic crystallites that comprise the PyC, both of which evolve with V_{f}.
- ▷ Y for CNTs has a value of $Y \sim 1$ TPa, whereas G for CNTs has a value of $G \sim 1$ GPa when $G \geq E_{\text{cm}}$, and $G \approx E_{\text{cm}}$ when $G < E_{\text{cm}}$.
- ▷ The A-CMNC effective modulus as a function of w ($\rightarrow E_{\text{cmnc}}(w)$) is approximated *via* rule of mixtures of $E_{\text{cnt}}(w)$ and E_{cm}.
- ▷ Predicted $E_{\text{cmnc}}(w)$ results are compared to E values for A-CMNCs measured using Vickers microhardness testing and recently reported simulation results for A-CMNCs modeled using an amorphous carbon matrix from Ref. 159.

By predicting the behavior of these three kinds of A-CNT comprised material systems, property prediction for many other types of A-CNT based materials is enabled, since the analyses presented in Chapters 4 – 6 can be modified to accommodate a wide variety of CNT morphologies and matrix material structure and chemistry.

3.2.3 Limitations of Current Work

Although the approaches outlined in Section 3.2.1 and Section 3.2.2 of this Chapter are an advance, there were some limitations that were imposed by the current state-of-the-art of characterization and modeling techniques:

Three-dimensional Morphology of A-CNTs:

- ▷ The CNT bundling characteristics/formation and CNT-CNT interaction within A-CNT systems could not be included in the current approach because the evolution of the CNT electrostatic interactions as a function of CNT proximity is not currently known.
- ▷ CNT entanglement/interpenetration could not be modeled because true 3D descriptions of the topology of CNTs that comprise A-CNT arrays is currently unavailable.

Mechanical Property Prediction for A-CNT Comprised Materials:

- ▷ Influence of CNT-CNT frictional effects during deformation could not be studied because of lack of experimental 3D CNT morphology data.
- ▷ Impact of matrix on the CNT morphology in nanocomposites could not be directly studied because of insufficient experimental data on the evolution of the packing geometry and topology of A-CNT during polymer infusions, and subsequent curings, with a secondary material.
- ▷ Explicit inclusion of the (polymer-CNT or PyC-CNT) interphase region was not possible because of a lack of experimental and simulation data on their micro/nanostructure and mechanical properties/behavior.
- ▷ Property prediction on A-CNT systems with $V_\mathrm{f} > 20\%$ could not be included here because experimental data on such CNT systems is not currently available due to manufacturing challenges.

Additional work that can enable future studies to overcome these limitations can be found in Chapter 8.

Chapter 4

Morphology of Aligned Carbon Nanotube Architectures

To predict how CNT non-idealities affect the performance of A-CNT systems, the morphology of A-CNT arrays must first be explored and analyzed in three-dimensions. While the morphology of A-CNTs was previously characterized in a wide variety of ways, quantification of the three-dimensional morphology of A-CNTs was not possible until very recently,[157] and this Chapter presents an approach to simulate A-CNT arrays comprised of $> 10^5$ CNTs with realistic stochastic morphologies using a previously developed theoretical framework for the A-CNT packing structure, and experimental A-CNT morphology quantifications. Using this knowledge, structure-property relations of A-CNT arrays and their composites can be developed, allowing more precise control over the performance of materials comprised of A-CNTs.

This Chapter presents the experimental, theoretical, and simulation approach utilized to quantify and model the morphology of A-CNT arrays in three-dimensions. A-CNTs are a model NF architecture, and many of the techniques and quantifications presented here are generally applicable to other NF systems. The 3D analysis of the A-CNT packing structure is achieved through four easily accessible morphology measures of CNTs: inter-CNT spacing (Γ), two-dimensional coordination number (N), sinusoidal waviness ratio (w), and CNT volume fraction (V_f).[1]

---

[1] Parts of this Chapter previously appeared in Refs. 40 and 41

4.1 Current State of the Art of A-CNT Morphology Quantification

As briefly mentioned above, this Chapter focuses on the experimentally guided theory and simulation tools that were developed to model the stochastic morphology of the CNTs that comprise A-CNT arrays. In this Section, previous deterministic efforts to quantify the morphology of A-CNTs are reviewed, and recently developed techniques that enable the direct evaluation of the three-dimensional morphology of A-CNTs are discussed.

Although previous works on CVD grown A-CNTs have reported that the CNTs that comprise scalable arrays have waviness/tortuosity that is not negligible,[72–74,153,160,161] is directly tied to the parameters used in the synthesis process,[72,73] and strongly impacts their behavior,[72,73] existing theoretical models usually assume idealized collimated A-CNTs ($w = 0$) for simplicity.[43,46] To account for this waviness, previous studies have used the sinusoidal functional form of w, characterized by the ratio of the amplitude (a) and wavelength (λ) of the sine waves ($\rightarrow w = a/\lambda$), and have shown that $w \gtrapprox 0.2$ for the as-synthesized A-CNT arrays used throughout this dissertation.[50,70,158] See Figure 4.1a for a high resolution scanning electron micrograph of the cross-sectional morphology of as-grown A-CNTs demonstrating their significant waviness. These models mention that since a precise description of the CNT waviness was not available at the time, further work is required to appropriately account for waviness when modeling the evolution of the CNT packing morphology.[43] In this Chapter, A-CNT arrays comprised of 10^5 CNTs with realistic morphologies are simulated, and the impact of the CNT waviness on an easily accessible measure of the CNT morphology, Γ, and the N that specifies the A-CNT packing geometry are presented. See Figure 4.1b for an illustration of the collimated ($w = 0$) idealization utilized by some previous studies, and the simulated wavy A-CNTs studied here.

While previous studies on quantifying the morphology of A-CNTs used 2D imaging techniques, such as HRSEM and high resolution transmission electron microscopy (HRTEM), these techniques are not well suited for extracting all of the parameters that characterize the complex three-dimensional morphology of the CNTs, *e.g.* bundling points, angular dispersion, and waviness.[157,162] These 3D morphology features can be quantified *via* quantitative electron tomography, which is emerging as one of the preferred approaches to visualize nanostructured materials in 3D,[155,163–165] and was recently utilized to study A-CNTs arrays,[166,167] and A-PNCs manufactured over a range of V_f.[157] See Figure 4.2 for the 3D morphology of the A-CNTs that comprise A-PNCs visualized *via* quantitative electron tomography as presented by Natarajan et al.[157] The

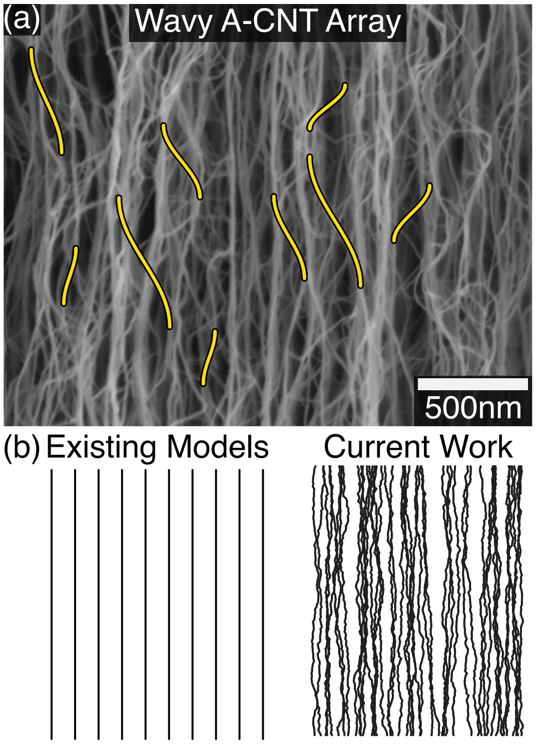

Figure 4.1: Real wavy A-CNTs and theoretical frameworks. (a) Representative HRSEM image of wavy A-CNTs. (b) Illustration of the CNT morphology normally assumed in existing theoretical frameworks, which neglect the CNT waviness, and the wavy CNTs with realistic stochastic morphologies generated using the simulation framework presented here.

key measure of 3D waviness used throughout this dissertation is τ, which can be readily extracted from the 3D CNT reconstructions, and can be converted back to an effective 2D waviness description, *i.e.* w, by assuming a functional form, such as the common sinusoidal functional form used here and throughout the literature (see Section 4.2.1). Using τ, this Chapter develops a simulation framework that is capable of modeling 3D A-CNT arrays with a stochastic representation of waviness.

This Section introduced previous morphology quantification efforts, and the cutting edge approach to characterizing A-CNT systems in 3D. In the remainder of this Chapter, the experimental, theoretical, and simulation efforts undertaken to model the A-CNT morphology, along with their resulting 3D visualizations, are presented and discussed.

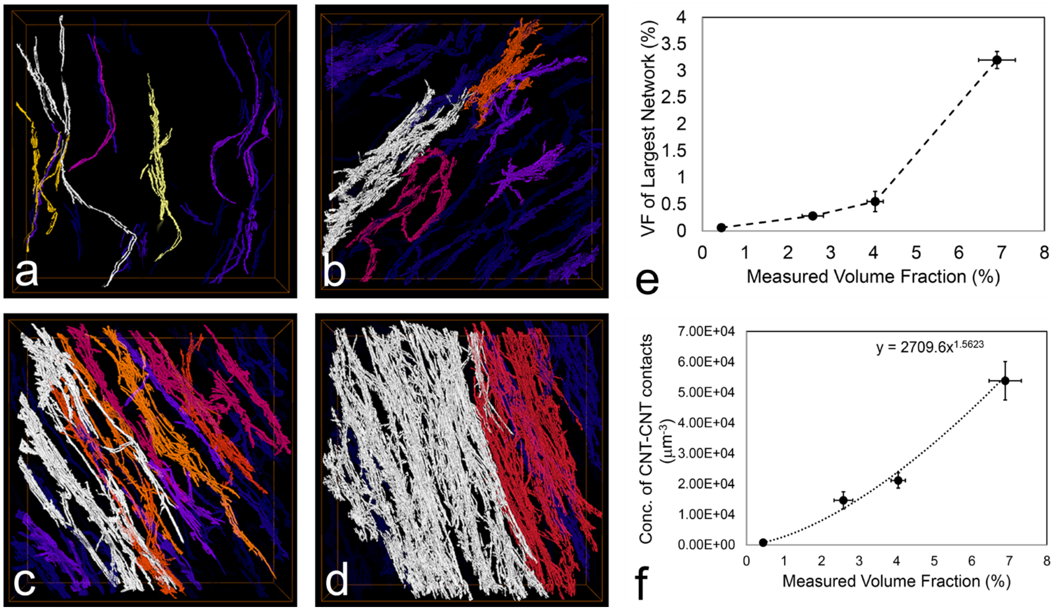

Figure 4.2: 3D morphology of the A-CNTs that comprise A-PNCs visualized *via* quantitative electron tomography as presented by Natarajan et al.[157]

4.2 Morphology Characterization, Modeling, and Simulation

In this Section, experimental, theoretical, and simulation methodologies are presented. Section 4.2.1 contains the experimental details, and equations that enable conversion from the deterministic w to the stochastic τ. Section 4.2.2 outlines the theoretical framework used to quantify the impact of waviness on the packing structure of A-CNTs. Section 4.2.3 details the developed simulation framework utilized to model the stochastic morphology of A-CNT systems in 3D. These tools will be used to analyze and model the three-dimensional morphology of A-CNTs, and to recommend future paths of study that will enable better more representative simulation of the morphology of A-CNT systems.

4.2.1 Experimental Quantification of A-CNT Waviness

To estimate the waviness evolution of A-CNT arrays as a function of packing proximity, w was approximated from images of the cross-sectional morphology of CNT arrays with $1\% \lesssim V_\mathrm{f} \lesssim 20\%$ taken using an HRSEM (JEOL 6700, 3.0 mm working distance, $1-1.5$ kV accelerating voltage),[40,43,46,70] and by assuming a sinusoidal function form for w. At each V_f, w was approximated from 30 CNTs ($\rightarrow n = 30$). To convert from a deterministic waviness description (defined by w) to a stochastic one, τ of the CNTs, which is defined as the ratio of the true (arc) length of the CNTs to the measured height of the CNT array in the z direction, should be used instead of w. τ can be defined as follows for w that have sinusoidal ($\rightarrow \tau(w)_{\text{sin}}$) or helical ($\rightarrow \tau(w)_{\text{helix}}$) functional forms (Eq. 4.1 and Eq. 4.2 are simplified using $\rightarrow w = a/\lambda$ and setting $a = 1$):[70]

$$\tau(w)_{\text{sin}} = \int_{0}^{1} \sqrt{\left(1 + (2\pi w \cos(2\pi z))^2\right)}\, \mathrm{d}z \tag{4.1a}$$

$$\tau(w)_{\text{helix}} = \sqrt{(1 + (2\pi w)^2)} \tag{4.1b}$$

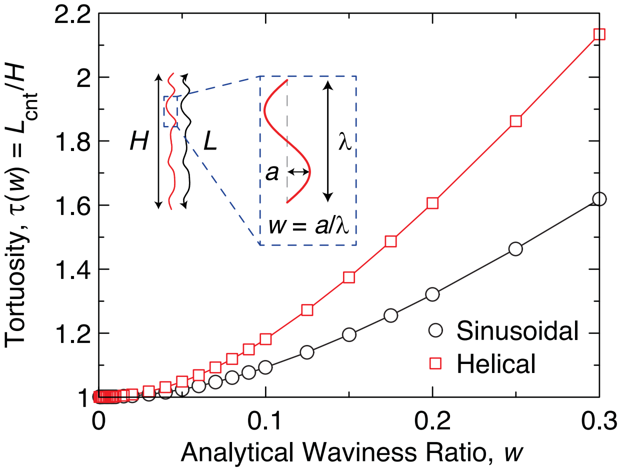

Figure 4.3: Tortuosity (τ) as a function of waviness ratio (w) for sinusoidal (Eq. 4.1a) and helical (Eq. 4.1b) functional forms of the CNT morphology. Inset shows an illustration of w using the sinusoidal amplitude/wavelength (a/λ) functional form, and w for the helical functional form (not illustrated) would be evaluated by defining the helix radius as a.

See Figure 4.3 for a plot of τ_{sin} and τ_{helix} evaluated *via* Eq. 4.1a and Eq. 4.1b. The mean, standard deviation, and uncertainty of τ using both the sinusoidal ($\rightarrow \mu_{\tau}^{\text{sin}}$, $\delta_{\tau}^{\text{sin}}$ and $\delta_{\tau}^{\text{sin}}/\sqrt{n}$, respectively) and helical ($\rightarrow \mu_{\tau}^{\text{helix}}$, $\delta_{\tau}^{\text{helix}}$ and $\delta_{\tau}^{\text{helix}}/\sqrt{n}$, respectively) functional forms can be found in Table 4.1 in Section 4.3.2.

4.2.2 Theoretical Framework for Deterministic Waviness Corrected A-CNT Packing Geometry

This Section contains the equations used to compute the inter-CNT spacings, and the accessible exohedral CNT array porosity.

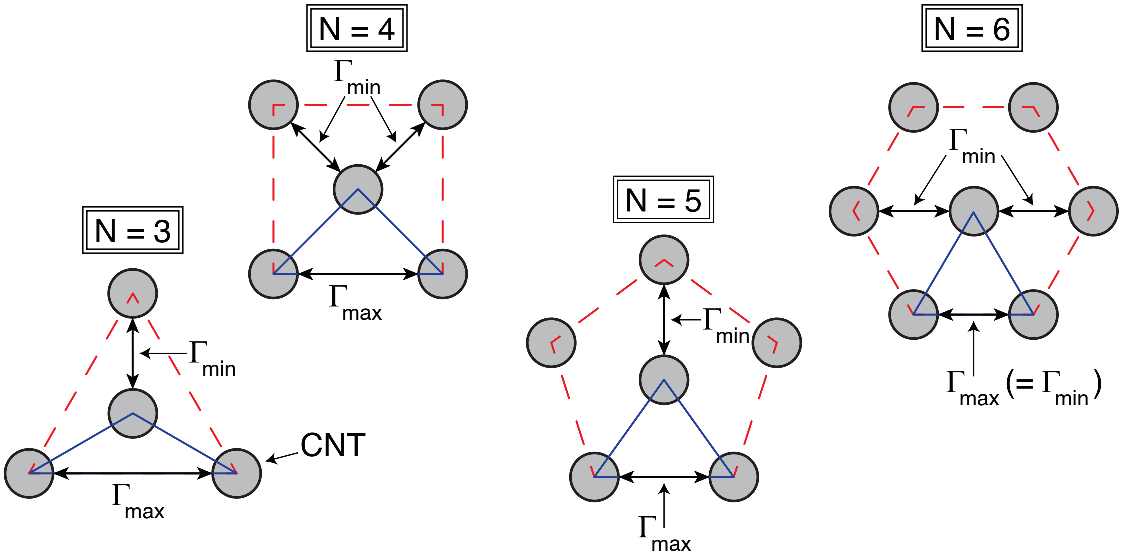

Figure 4.4: Illustration of N, and the effective constitutive triangles that comprise each coordination.[43,46] The average of Γ_{min} and Γ_{max}, defined as Γ, is used in throughout this dissertation as an easily accessible measure of the morphology of A-CNT.

4.2.2.1 Inter-CNT Spacing Relations

A previous study[43] developed the following relationship between Γ, V_{f}, the CNT outer diameter (D_{o}), and N of an idealized A-CNT system (See Fig. 4.4 for an illustration of the geometry):

$$\Gamma = D_{\text{o}} \left((11.77(N)^{-3.042} + 0.9496) \sqrt{\frac{\sqrt{3}\pi}{6V_{\text{f}}}} - 1 \right) \tag{4.2a}$$

$$N = 2.511(V_{\text{f}}) + 3.932 \tag{4.2b}$$

Note that the previous study found that packing coordination increased strongly with V_{f} (see Eq. 4.2b), likely due to the biaxial densification utilized to create high V_{f} arrays from as-grown ($V_{\text{f}} \sim 1\%$) arrays. Using the isosceles angle ($\theta_{\triangle}$) of the constitutive triangles at each N, the minimum (Γ_{min}) and maximum (Γ_{max}) inter-CNT spacings can be separated from Γ, yielding the following:

$$\theta_{\triangle} = \pi \left(\frac{1}{2} - \frac{1}{N} \right) \tag{4.3a}$$

$$\Gamma_{\text{min}} = 2 \left(\frac{\Gamma}{1 + 2\cos(\theta_{\triangle})} \right) \tag{4.3b}$$

$$\Gamma_{\text{max}} = 4\cos(\theta_{\triangle}) \left(\frac{\Gamma}{1 + 2\cos(\theta_{\triangle})} \right) \tag{4.3c}$$

4.2.2.2 Waviness Correction for Square and Hexagonal Packing

To quantitatively evaluate the impact of waviness on the morphology of the A-CNT arrays, a measure that can be relatively easily assessed experimentally was selected: Γ. To approximate Γ for the simulated wavy CNTs (see Section 4.2.3), the difference in position in the $x-y$ plane for each CNT was calculated using the separation of the current CNT, for example a CNT in the center of a square unit cell located in layer B (see Figure 4.5 in Section 4.2.3 for an illustration), with its neighboring CNTs as follows: the inter-CNT separation for CNTs in the same layer, *i.e.* the two neighboring CNTs in layer B for the exemplary CNT, which yields Γ_{min}. Γ was approximated by simply taking the average of Γ_{min} and Γ_{max}.[43] The CNTs on the outer boundary were treated differently to account for the missing neighbor CNTs, but have a very small contribution $\ll 0.1\%$ overall if sufficiently large simulation cells are used ($n \gtrapprox 1600$). The contribution of the CNT waviness to Γ was included in the analysis as follows:

$$\Gamma(w) = \Omega(w)\Gamma(w=0) \tag{4.4}$$

Where Ω is the waviness correction with a value that is > 1 for $w > 0$, and $\Gamma(w=0)$ is evaluated using N and V_{f} using the previously reported theoretical framework.[43]

4.2.3 Simulation Framework for Stochastic 3D A-CNT Morphology

Here the various components that enable simulation of the A-CNT morphology both stochastically and in 3D are discussed.

4.2.3.1 Three-Dimensional Morphology Simulation Scheme

To simulate wavy CNTs, each CNT was discretized into an array of nodes in three dimensions (*xyz* space). The position of the first node was determined using the constitutive triangles that are defined by the two dimensional ($x-y$ plane) coordination number (N), which was discussed in detail previously.[43,46] See Figure 4.5 for illustration of the constitutive triangles that define each N. Since values of N that fall between square ($N=4$) and hexagonal ($N=6$) close packing may not propagate properly in the $x-y$ plane, CNTs were initialized in layers, and each layer was arranged in a manner analogous to Bernal stacking (*i.e.* ABAB type stacking) to facilitate the formation of constitutive triangles with appropriate dimensions as defined by N and V_{f}.[43] See Figure 4.5 for an illustration of the layer-like arrangement of the first nodes of the discretized CNTs, and for exemplary initialized

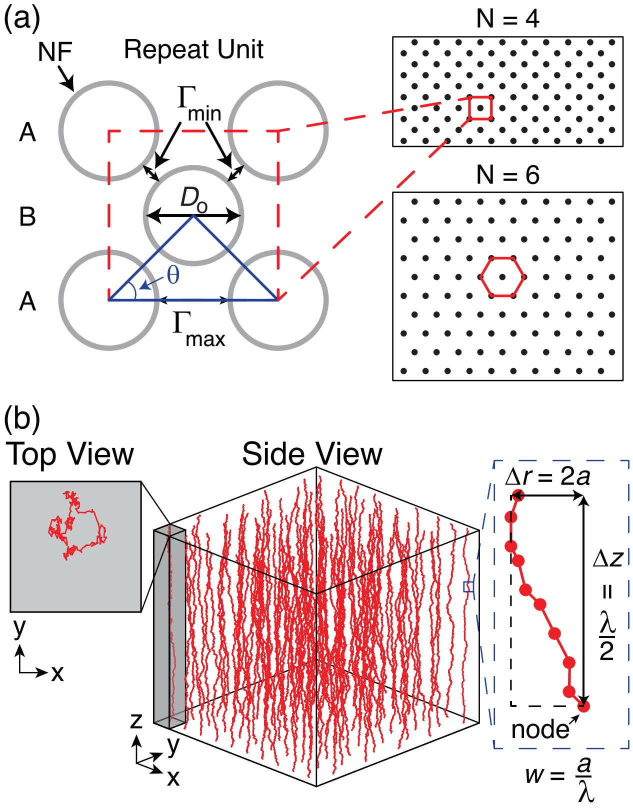

Figure 4.5: Three-dimensional morphology simulation details. (a) Illustration of the simulation scheme, origin of Γ from N, and the top view of an initialized simulation cell comprised of collimated 100 CNTs for $N = 4$ (square packing) and $N = 6$ (hexagonal packing). (b) Initialized simulation comprised of 100 wavy CNTs showing how the average node displacements in the $x-y$ plane and z direction are tied to the a and λ that originate from the experimentally-quantified sinusoidal w ($\rightarrow w = a/\lambda$) and used to generate wavy CNTs.

simulations comprised of 100 CNTs ($\rightarrow n = 100$) for $N = 4$ and $N = 6$. To apply the appropriate waviness to all other nodes, the displacement of each node relative to the node that precedes it, defined as Δr, was evaluated using the a extracted from w, and the node displacement increment in the z direction was set at a magnitude of 0.05λ, which has a value equal to Γ_{max},[40,46] so that a unit cell comprised of 10 nodes (see Figure 4.5b for illustration) will have a total z displacement, defined as Δz, of magnitude $\lambda/2$. See Section 4.2.3.2 for a discussion about the unit cell used in the analysis. Since the waviness of the CNTs is inherently random, the displacement specified by the evaluated a was independently applied to the nodes of the CNT in both x and y directions using Gaussian distributions. Using Gaussian distributions to apply the node displacements has two distinct advantages: 1) The mean and standard deviations (normally $\gtrsim$ 50% of the mean values)[40,50,158] of w can be used to directly specify the waviness, which may not be true with other distributions; 2) the node displacements are no longer uniform nor deterministic, *e.g.* as in cases where sinusoidal or helical functional forms were assumed,[168–172] likely leading to more realistic morphologies. Also, while the current method does not explicitly account for CNT-CNT interactions, *e.g.* van der Waals (vdW) interactions used in recent modeling efforts,[139,147,173] in the three-dimensional morphology evolution, the stochastic nature of the CNT array morphology implicitly accounts for the attractive and repulsive forces that would be experienced by the CNTs, while avoiding the assumption of a simplistic electrostatic potential that may not be representative for CNTs with native defects and other adsorbed species.[46] The main difference between the current method, and modeling efforts that include electrostatic interactions, is that CNT arrays simulated here might form fewer bundles/aggregates, but such an effect should be very small when averaged over a sample size of $> 10^5$ CNTs. See Figure 4.5b for a top-view snapshot of a single wavy CNT along the z direction demonstrating the random-walk like nodal displacement, and for a side view snapshot of a simulation comprised of $n = 100$ wavy CNTs. To ensure that the waviness generated using the scheme used here is consistent with the amount of waviness that would result if a simple sinusoidal functional form was used instead, the separation of the nodes in the z direction was adjusted so that the ratios of the true length of the CNT (L_{3D}) to the measured height of the CNT in the z direction (L_{1D}) for both schemes were matched. The $L_{\mathrm{3D}}/L_{\mathrm{1D}}$ ratio is a common way to evaluate τ of the CNTs, and since τ does not depend on the functional form, a, and λ of the waviness, the $L_{\mathrm{3D}}/L_{\mathrm{1D}}$ ratio is a more flexible measure by which the waviness of CNTs can be quantified and compared between systems.

4.2.3.2 Unit Cell Analysis for Simulating Morphology in 3D

To define the unit cell used in the analysis, one has to consider two displacements: the Δr, *i.e.* the two-dimensional random walk; and Δz, *i.e.* the nodal displacement. Each unit cell was comprised of 10 nodes whose z separation has a magnitude of 0.05λ ($\rightarrow 0.5\lambda$ for 10 nodes) as mentioned in Section 4.2.3.1, where λ is the characteristic wavelength of the waviness from w. See Figure 4.6 inset for illustration of the unit cell used in this analysis. Using the geometry of the unit cell shown in Figure 4.6, Δr, Δz, and the local radius of curvature of the CNT (R_{c}) from the intersecting chord theorem can be defined as follows:

$$\Delta r = \chi(w)\lambda \tag{4.5a}$$

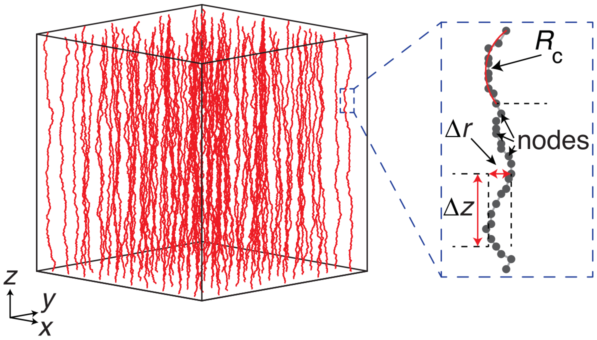

Figure 4.6: Unit cell used in the analysis defined using the average displacement in the $x-y$ plane ($\rightarrow \Delta r$) and 10 nodes in the z direction ($\rightarrow \Delta z$). Δr and Δz are tied to the amplitude (a) and wavelength (λ) from the waviness ratio ($w = a/\lambda$) which is used to simulate the morphology of the CNTs in three dimensions. The radius of curvature (R_c) is evaluated using the unit cell, and is used to approximate the maximum CNT volume fraction that the simulation can be used to study as discussed below.

$$\Delta z = \zeta(w)\left(\frac{\lambda}{2}\right) \tag{4.5b}$$

$$R_\mathrm{c} = 0.5\left(\Delta r + \frac{\Delta z^2}{16\Delta r}\right) \tag{4.5c}$$

where $\chi(w)$ is a factor that relates the average of the displacement of the CNTs in the $x-y$ plane, a stochastic quantity, to the deterministic w, and $\zeta(w)$ connects the separation of the nodes that bound the unit cell in the z direction, a quantity that is varied to control the average stochastic tortuosity of each wavy CNT (see Eq. 4.5), to the deterministic w. To approximate $\chi(w)$ and $\zeta(w)$, the average Δr and Δz are evaluated (see Figure 4.7) leading to the following functional forms:

$$\chi(w) = a_3 w \tag{4.6a}$$

$$\zeta(w) = a_4(w)^{b_4} + c_4 \tag{4.6b}$$

where $a_3 = 0.8794$ (coefficient of determination $\mathbb{R}^2 = 0.9999$); and $a_4 = -0.0748$, $b_4 = 0.6459$, and $c_4 = 0.4260$ ($\mathbb{R}^2 = 0.9962$). The fits in Eq. 4.6 begin to deviate significantly from the simulation data at $w > 0.3$, an effect that originates from interactions with the simulation box that confines each CNT and (in the model) prevents the CNTs from venturing outside of their confining box. This forces the CNTs to be non-interacting, and ensures that the system can be treated as dilute. Such an approximation is likely reasonable when the CNTs are not all in bundles, *e.g.* in A-CNT volume fractions that are far below the theoretical maximum of $\sim 83.45\%$ CNTs.[43] Since the CNT-CNT electrostatic interactions are not well understood, and require further study to properly

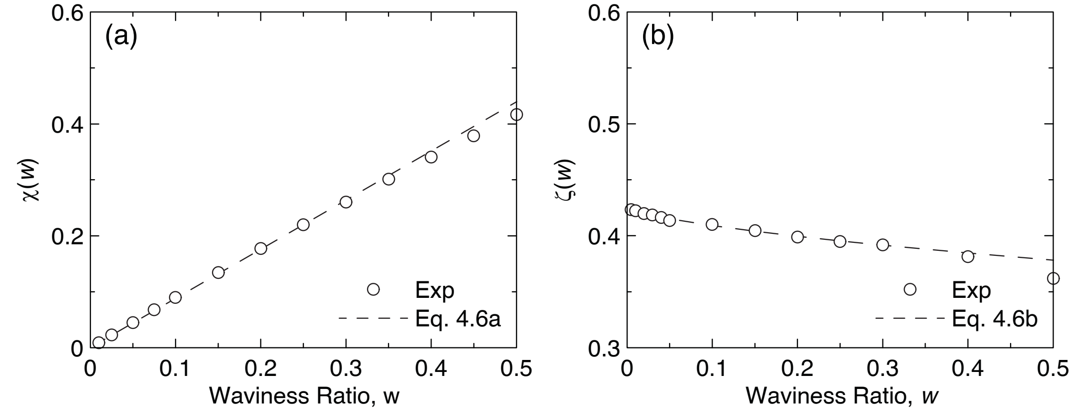

Figure 4.7: Factors that link $\chi(w)$ and $\zeta(w)$ to w for A-CNTs studied in this work. (a) $\chi(w)$ scaling with w demonstrating that CNT interactions with the hard boundaries that define the confining volume are significant at $w \gtrapprox 0.3$ where $\chi(w)$ transitions from a linear scaling (see Eq.4.6a) to a power scaling. (b) $\zeta(w)$ scaling with w demonstrating that CNT-boundary interactions are significant at $w \gtrapprox 0.3$ where $\zeta(w)$ transitions from a power scaling (see Eq. 4.6b) to a linear scaling.

simulate and model, this study was limited to $w \lessapprox 0.3$ where $\chi(w)$ is a constant and $\zeta(w)$ varies by $\lessapprox 10\%$.

4.3 Results and Discussion

In this Section, the experimental, theoretical, and simulation results are presented. Section 4.3.1 contains error scaling of the 3D morphology analysis, and the maximum V_f that the simulation can be utilized to study. Section 4.3.2 contains the experimental results of the w scaling with V_f. Section 4.3.3 uses the w evolution with packing proximity to quantify the impact of waviness on the packing morphology of A-CNT arrays *via* Γ, and concludes with the scaling of Ω with V_f that enables the waviness of A-CNT arrays to be accounted for when modeling their effective packing structure (via N).

4.3.1 Evaluation of Morphology Error Scaling and Validity Regime for Simulation Framework

To simulate the morphology of CNTs in 3D, each CNT was discretized into an array of nodes in *xyz* space as discussed in detail in Section 4.2.3. The width of the confining two-dimensional area that bounds the node displacements of CNTs was defined using the CNT Γ_min and Γ_max (*e.g.* ≈ 64 nm and ≈ 92 nm at $V_\mathrm{f} \approx 1$ vol. % CNTs) quantified previously,[43,46] including the evolution of the packing morphology of the CNTs as their V_f is increased *via* densification. To approximate the error scaling of the morphology measurement with the size of the $n \times n$ simulation cell, the model standard error of Γ was evaluated as a function of n, and is plotted in Figure 4.8a. As Figure 4.8a demonstrates, the familiar standard error scaling of $\propto 1/\sqrt{n}$ is exhibited, and to ensure a standard error of $\lesssim 0.1\%$, a simulation size of $n > 10^5$ ($\rightarrow 320 \times 320 = 1.024 \times 10^5$ CNTs) is used throughout this dissertation. Also, since the tortuosity dependent local radius of curvature (R_c) of the CNTs strongly influences their elastic response and may determine the maximum valid V_f for the model to be representative, Δr and Δz were used to evaluate R_c *via* Eq. 4.5c in Section 4.2.3.2. See Figure 4.8b for an illustration of R_c evaluated using 10 nodes, and the scaling of R_c with w

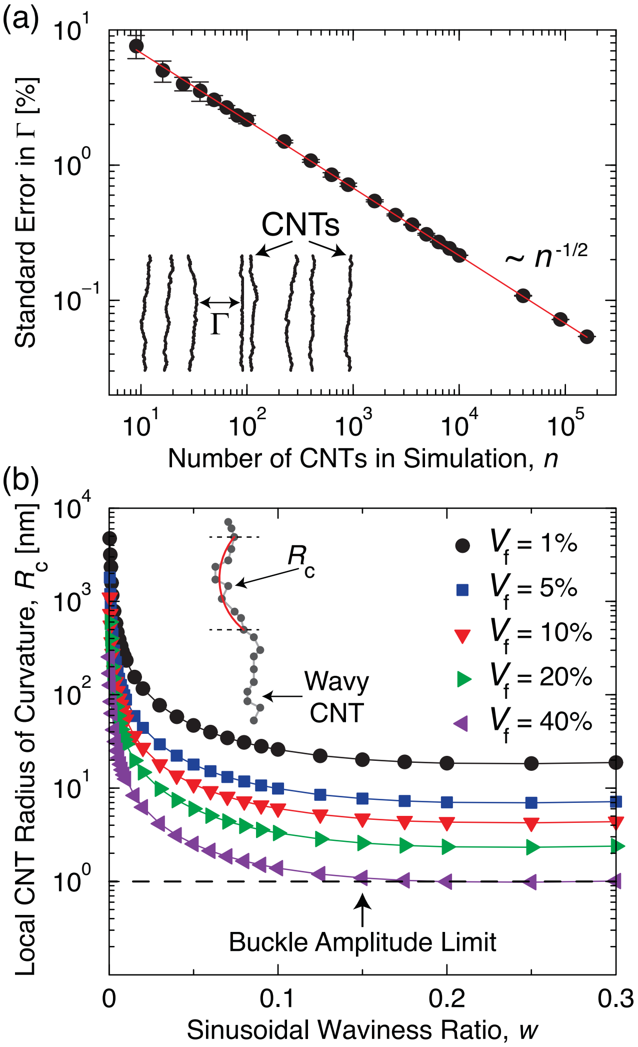

Figure 4.8: Standard error scaling and V_f validity regime. (a) Scaling in standard error of the measured Γ values demonstrating the importance of number of CNTs in the simulation (n), and replicating the familiar $1/\sqrt{n}$ standard error scaling for Gaussian statistics. (b) Plot showing the evolution of the CNT alignment, represented by R_c, as a function of w.

and V_{f}. As Figure 4.8b demonstrates, R_{c} plateaus at $0.1 \leq w \leq 0.3$ and has a value of ~ 1 nm for $V_{\mathrm{f}} = 40\%$ CNTs, a value that is on the same order of the curvature of ripples that are expected to form on the surface of ~ 8 nm diameter (~ 1.5 nm wall thickness) CNTs during buckling,[174,175] indicating that the simulation results are physical for $V_{\mathrm{f}} \leq 40\%$ CNTs. A note should be made that $R_{\mathrm{c}} \sim 1$ nm is on the same order as the variations in the CNT inner and outer diameter that were reported previously,[70] and that such nanoscale surface features can arise through either Stone-Wales or inter-wall defects.[62,176–178] To ensure that R_{c} is evaluated for an amount of waviness that is generalizable to other non-stochastic descriptions, *e.g.* sinusoidal or helical functional forms, Δz was controlled so that $L_{\mathrm{3D}}/L_{\mathrm{1D}}$, also known as τ, for the stochastic system matched the $L_{\mathrm{3D}}/L_{\mathrm{1D}}$ ratio (*i.e.* τ) for the deterministic sinusoidal description at each value of w. See Section 4.2.3 for details. To evaluate the impact of CNT proximity effects on their morphology, the evolution of w as a function of the V_{f} was quantified.

4.3.2 Experimental Quantification of A-CNT Waviness Evolution with V_{f}

The waviness of the A-CNT arrays was evaluated employing a simple sinusoidal amplitude-wavelength (a/λ) definition of w, and was approximated from HRSEM images of the cross-sectional morphology of the A-CNT arrays. See Figure 4.9a for exemplary HRSEM micrographs of A-CNT arrays as a function of V_{f}, and for an illustration of the waviness quantification using a sinusoidal definition of w. Note that these HRSEM images were taken from both edges, and the middle region, of the grown A-CNT arrays, to ensure that the w estimated here is representative for the entire volume of the A-CNT arrays. Since HRSEM images of the morphology of the CNT arrays are projections of a three-dimensional system onto a two-dimensional surface, information about the waviness in the transverse direction (*i.e.* the direction parallel to incident electron beam, in the $x-y$ plane of Figure 4.6) is lost and must be accounted for. To account for the loss of depth information, a correction factor of $\sqrt{2}$ was applied to simulate a mean view angle of 45° (λ is independent of the view angle and requires no correction).[50] See Figure 4.9b for a plot of the evaluated w as a function of V_{f}. As Figure 4.9b illustrates, CNT confinement at higher V_{f} both reduces the mean values and statistical uncertainties of w significantly from $\sim 0.2 \pm 0.02$ at $V_{\mathrm{f}} \approx 1\%$ CNTs to $\sim 0.1 \pm 0.01$ at $V_{\mathrm{f}} \approx 20\%$ CNTs (See Table 4.1 for details, and Appendix A for the raw waviness data). Note that the experimental V_{f} is simply calculated from the geometry change of the as-grown $V_{\mathrm{f}} \sim 1\%$ A-CNT arrays to the higher V_{f} due to the biaxial mechanical densification method employed here.[22] The values for w at $V_{\mathrm{f}} \sim 1\%$ CNTs are on the same order as previously reported for similar A-CNT systems, $w \simeq 0.2 \pm 0.1$,[50,179] and are in agreement with recently reported τ ($\rightarrow L_{3D}/L_{1D}$) evolution of similar A-CNTs during densification, where $\rightarrow L_{3D}/L_{1D}$ decreased from ~ 1.2 ($\rightarrow w \sim 0.15$) at the as-grown state ($V_f \sim 3\%$ CNTs) to ~ 1.06 ($\rightarrow w \sim 0.08$) for A-CNTs densified by a factor of $6\times$ ($V_f \sim 20\%$ CNTs).[45] Since the statistical uncertainty (and standard deviation) of w decreases significantly during packing, but the A-CNT morphology remains very stochastic (the standard deviation of w is consistently at $\gtrsim 50\%$ of the mean value of w as shown by Table 4.1), representative descriptions of the CNT waviness and morphology must account for both the mean and uncertainty in w. Therefore, to simulate the observed scaling of w as a function of V_f, both the mean ($\mu_w^{\sin}$) values of w and the standard deviation in $\mu_w^{\sin}$ ($\delta_w^{\sin}$) were fit independently *via* power laws using the theoretical maximum V_f of 83.45% CNTs, where both the mean and standard deviation of w have a value of 0,[43] leading to the following scaling relations (with coefficient of determination

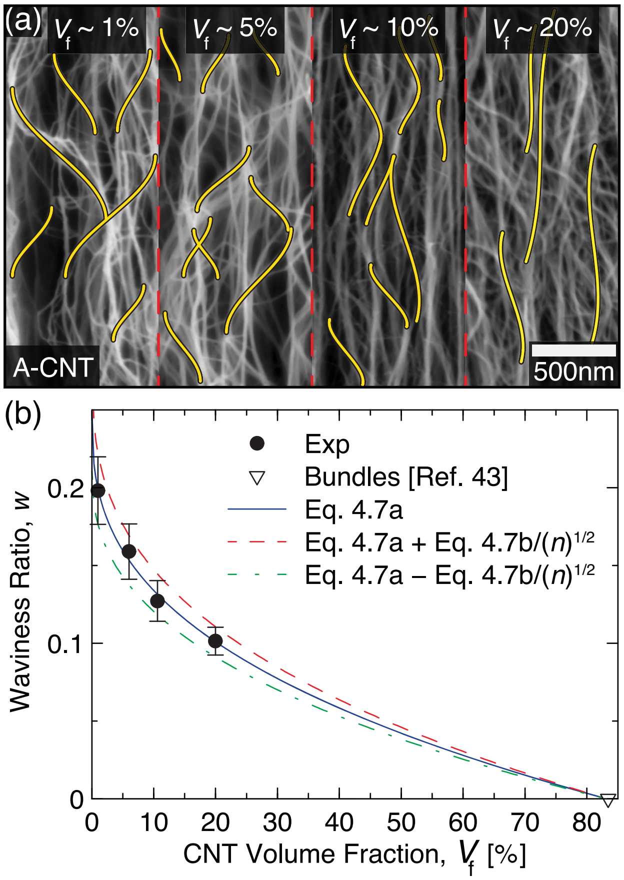

Figure 4.9: Evolution of the CNT waviness with packing. (a) Cross-sectional HRSEM micrographs of A-CNT arrays at V_f ranging from $\sim 1-20$ vol. % CNTs showing the reduction in CNT waviness. (b) Plot demonstrating that w can be reduced by $\sim 50\%$ by increasing V_f from ~ 1 vol. % CNTs to ~ 20 vol. % CNTs.

$\mathbb{R}^2 = 0.9996$ for Eq. 4.7a and $\mathbb{R}^2 = 0.9812$ for Eq. 4.7b):

$$\mu_{\mathrm{w}}^{\sin}(V_{\mathrm{f}}) = -0.04967(V_{\mathrm{f}})^{0.3646} + 0.2489 \tag{4.7a}$$

$$\delta_{\mathrm{w}}^{\sin}(V_{\mathrm{f}}) = -0.0852(V_{\mathrm{f}})^{0.2037} + 0.2100 \tag{4.7b}$$

Using the scaling relations presented in Eq. 4.7, the impact of waviness on the mechanical behavior of CNT arrays was explored in Chapter 5.

Table 4.1: Experimentally determined w and τ from Eq. 4.1 as a function of V_{f}. The included values of experimental mean and standard deviation $\mu_{\mathrm{w}}^{\sin}$, $\delta_{\mathrm{w}}^{\sin}$, and their calculated sinusoidal and helical forms $\mu_{\tau}^{\sin}$, $\delta_{\tau}^{\sin}$, $\mu_{\tau}^{\mathrm{helix}}$, and $\delta_{\tau}^{\mathrm{helix}}$ were approximated from 30 CNTs ($\rightarrow n = 30$). See Appendix A for the raw waviness data.

V_{f} [%]	Experimental waviness (sinusoidal)		Sinusoidal tortuosity		Helical tortuosity	
	$\mu_{\mathrm{w}}^{\sin}$	$\delta_{\mathrm{w}}^{\sin}$	$\mu_{\tau}^{\sin}$	$\delta_{\tau}^{\sin}$	$\mu_{\tau}^{\mathrm{helix}}$	$\delta_{\tau}^{\mathrm{helix}}$
1	0.198	0.119	1.352	0.352	1.596	0.556
6	0.159	0.098	1.253	0.243	1.414	0.414
10.6	0.127	0.072	1.171	0.147	1.279	0.272
20	0.101	0.049	1.109	0.097	1.184	0.161

4.3.3 Waviness Corrected A-CNT Packing Structure

Since square ($N = 4$) and hexagonal ($N = 6$) packing are the most commonly assumed coordinations,[43] but dependence on CNT waviness is not currently known, Γ was evaluated as a function of w for $0 \leq w \leq 0.3$ which are representative of the typical range of the experimentally observed A-CNT waviness.[40,70,157] Using Γ at $w = 0$ ($\rightarrow \Gamma(w = 0)$), *i.e.* morphology of idealized collimated CNTs, the waviness correction for $N = 4$ ($\rightarrow \Omega_{\square}$) and $N = 6$ ($\rightarrow \Omega_{\hexagon}$) was evaluated *via* Eq. (4.4). See Figure 4.10 for plots demonstrating the scaling of $\Omega_{\square}$ and $\Omega_{\hexagon}$ with w. As Figure 4.10a demonstrates, the scaling of $\Omega_{\square}$ with w can be described by power laws at three different regimes ($\mathbb{R}^2 > 0.997$):

$$\Omega_{\square}(w) = \begin{cases} 4(w)^{1.6} + 1, & w < 0.05 \\ -0.0012(w)^{-1.2} + 1.076, & 0.05 \leq w \leq 0.125 \\ -0.0057(w)^{-0.47} + 1.076, & 0.125 < w \leq 0.3 \end{cases} \tag{4.8}$$

These three modes may be associated with physical effects with (1) initiation ($\rightarrow 0 \leq w < 0.05$), where the CNTs are just starting to fill the inter-CNT region, (2) crowding ($\rightarrow 0.05 \leq w \leq 0.125$),

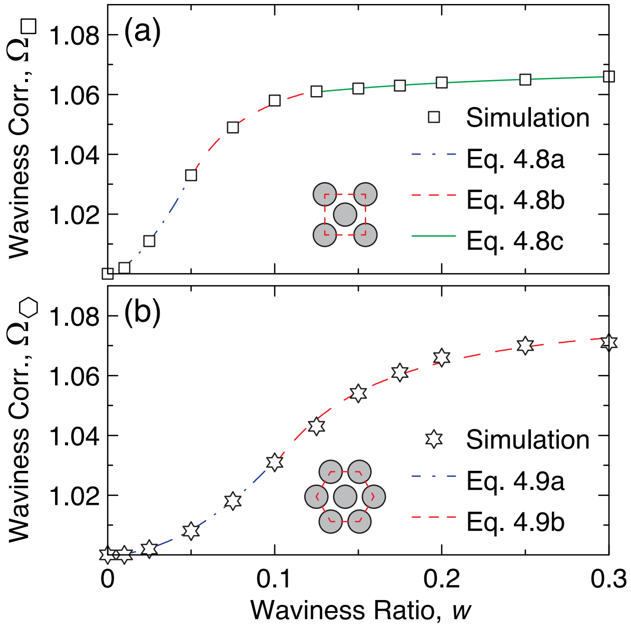

Figure 4.10: Impact of waviness (w) on the packing morphology of A-CNT arrays for square and hexagonal close packing. (a) Evolution of the waviness correction (see Eq.(4.4)) for square packing ($\Omega_{\square}$) as a function of w showing that the scaling of $\Omega_{\square}$ can be represented by three power laws at $w < 0.05$, $0.05 \leq w \leq 0.125$, and $w > 0.125$, and that square packing is best suited for A-CNT systems with $w \gtrapprox 0.15$ where $\Omega_{\square}$ increases very gradually. (b) Scaling of the waviness correction (see Eq.(4.4)) for hexagonal packing ($\Omega_{\hexagon}$) with w showing that $\Omega_{\hexagon}$ can be described by two power laws at $w < 0.1$, and $w \geq 0.1$, and that hexagonal packing is best suited for CNT systems with $w \lessapprox 0.05$ where $< 1\%$ error will be induced by neglecting the CNT waviness.

where the CNTs are starting to feel their neighbors (or bounding box in the simulation) that is characteristic of the formation of significant CNT bundles/junctions, and (3) saturation ($\rightarrow 0.125 < w \leq 0.3$), where the CNTs have already filled up most of the inter-CNT space and are perhaps slowly adding more CNT junctions/bundles. Figure 4.10a also indicates that $\Omega_{\square}$ is nearly constant at $w \gtrapprox 0.15$, where $\Omega_{\square} \approx 1.07$, meaning that square close packing is best suited for approximating the morphology of CNT arrays with significant waviness. As Figure 4.10b illustrates, the evolution of $\Omega_{\hexagon}$ with w is characteristic of power laws at two different regimes:

$$\Omega_{\hexagon}(w) = \begin{cases} 2.5(w)^{1.9} + 1, & w \leq 0.1 \\ -0.00143(w)^{-1.56} + 1.082, & 0.1 < w \leq 0.3 \end{cases} \tag{4.9}$$

The first two modes are consistent with the initiation ($\rightarrow 0 \leq w \leq 0.1$) and crowding ($\rightarrow 0.1 < w \leq 0.3$) modes of $\Omega_{\square}$, but since the first two modes span larger regimes for $\Omega_{\hexagon}$, and the saturation mode is not yet seen in Figure 4.10b, the saturation mode of $\Omega_{\hexagon}$ will occur later at $w > 0.3$. Also, since the first mode of $\Omega_{\hexagon}$ extends up to $w \approx 0.1$, Figure 4.10b indicates that hexagonal close packing will be best for CNTs with a small amount of waviness, where neglecting waviness will not incur a significant amount of error in the average packing morphology. Since $\Omega_{\square}$ and $\Omega_{\hexagon}$ are non-dimensional ratios of Γ that natively include the CNT diameter contribution, the results presented in Figure 4.10 are independent of the CNT diameter. To properly account for waviness in real A-CNT arrays, where N is not constant as V_{f} is increased, the previously reported scaling of evolution of the morphology exemplary system of A-CNTs, *i.e. via* Γ, as a function of the V_{f} is explored,[43] and the recently reported scaling of w for this system as a function of V_{f} is used to quantify the evolution of N as a function of CNT packing.[40]

Recent experimental work has demonstrated that, in an exemplary system of chemical vapor deposition (CVD) grown millimeter-long A-CNTs,[43,46] Γ is reduced from $\sim$ 80 nm to $\sim$ 10 nm as V_{f} is increased from $\sim$ 1 vol. % CNTs to $\sim$ 20 vol. % CNTs.[43] See Figure 4.11a for the previously reported experimental values of Γ. To better understand and model how Γ and Ω scale with V_{f}, the previous work assumed that the CNTs are collimated (*i.e.* not wavy), and using a continuous two-dimensional coordination number (N) model, extracted the effective coordination number at each V_{f}.[43] Using the theoretical data point of $N = 6$ at $V_{\mathrm{f}} = 83.4$ % CNTs, the previous study showed that N scales linearly with V_{f} (See Figure 4.11b).[43] Such a scaling relation assumes that very few CNT bundles form throughout the range of V_{f}, which might be reasonable for $V_{\mathrm{f}} \lessapprox 20\%$ CNTs (where experimental data was provided),[43] but is likely not true for $V_{\mathrm{f}} > 20\%$ where the formation of CNT bundles with $N = 6$ is likely more pronounced. The key limitation of the previous analysis was that the CNT waviness could not be integrated into the Γ description used to calculate N, which can lead to errors in the evaluated N, as shown in Figure 4.10. Using the experimental scaling relation of the mean and standard deviation of w with V_{f} (see Eq. 4.7),[40] the scaling of Γ and Ω with V_{f} was simulated and can be found in Figure 4.11a. As Figure 4.11a demonstrates, the simulated scaling of Γ with V_{f} agrees very well with both the experimental and previous theoretical model results,[43] and Ω scales linearly with V_{f} ($\mathbb{R}^2 = 0.9969$) for sinusoidal waviness:

$$\Omega = -0.002V_{\mathrm{f}} + 1.072 \tag{4.10}$$

See Table 4.2 for the calculated Γ and Ω values as a function of V_{f} using the simulated wavy A-CNT arrays. Using these simulation results, N was evaluated for CNTs with more realistic morphologies (see Figure 4.11b). As Figure 4.11b illustrates, the scaling of N with V_{f} for wavy A-CNTs

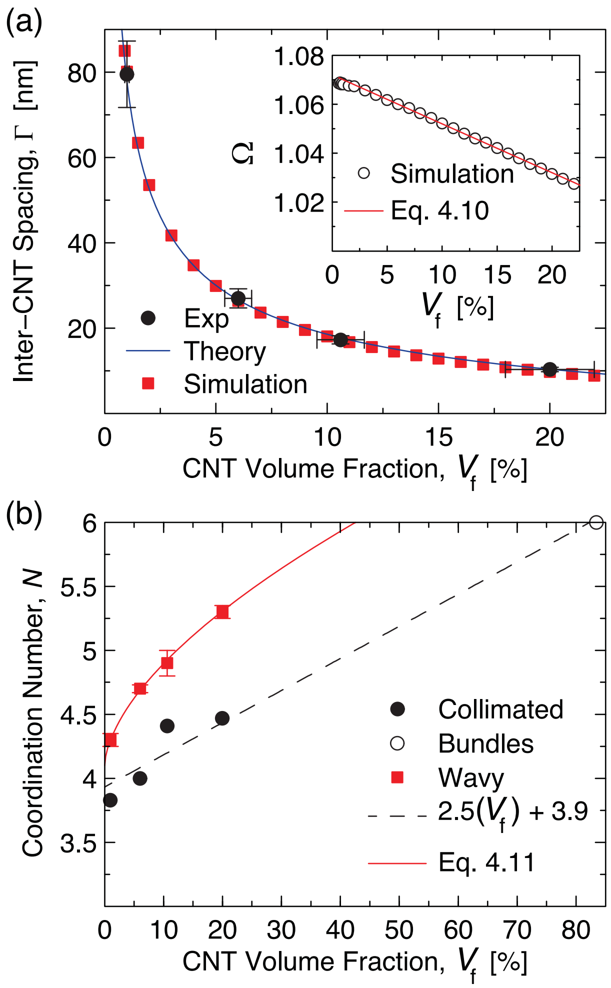

Figure 4.11: Evolution of morphology of A-CNTs as a function of their V_f. (a) Experimentally determined Γ as a function of V_f,[43] previously reported theoretical scaling of Γ with V_f for collimated A-CNTs,[43] and the simulated scaling of Γ with V_f for wavy A-CNTs. Inset: scaling of Ω with V_f. (b) The evolution of N during packing resulting from the previously reported theoretical scaling for collimated A-CNTs and their bundles,[43] and the simulated scaling for wavy A-CNTs showing that integration of CNT waviness into the theoretical framework is necessary to attain a coordination number scaling that is applicable beyond $V_\text{f} = 20\%$.

is very different from the previously reported linear scaling relation for collimated CNTs, and has the following form ($\mathbb{R}^2 = 0.9984$):

$$N(V_\text{f}) = \begin{cases} 0.2(V_\text{f})^{0.6} + 4.1, & V_\text{f} \lessapprox 40\% \\ 6, & V_\text{f} \gtrapprox 40\% \end{cases} \tag{4.11}$$

See Table 4.3 for the calculated values of N for the wavy A-CNT arrays. Eq. 4.11 indicates that at $V_\text{f} \approx 40\%$ CNTs, hexagonal ($N = 6$) packing is exhibited throughout the A-CNT arrays.

This makes sense because spatial inhomogeneities in both Γ and V_f are very significant at low ($\lesssim 10\times \rightarrow V_\mathrm{f} \sim 10\%$) densifications,[46] but becomes much less pronounced in higher densifications due to CNT-CNT confinement/proximity interactions.[29] These CNT-CNT proximity interactions, which were previously shown to have a significant influence on the A-CNT array behavior at $V_\mathrm{f} \gtrsim 5\%$,[46] will lead the A-CNTs to transition from the as-grown square ($N = 4$) packing structure to the lower energy, and more ideal, hexagonal ($N = 6$) close packing structure. Note that Eq. 4.11 is a reasoned extrapoloation beyond $V_\mathrm{f} > 20\%$ but the analysis cannot currently be validated due to lack of experimental data beyond $V_\mathrm{f} \sim 20\%$. Further work is required to quantify the impact of the CNT proximity/confinement interactions on the evolution of the packing morphology of A-CNT arrays during densification.

Table 4.2: Γ and Ω as a function of V_f, evaluated using the simulation described in Section 4.2.3.

V_f [%]	Γ [nm]	Ω []
0.6	106.44	1.0685
0.7	97.81	1.0689
0.8	90.75	1.0682
0.9	85.00	1.0686
1	80.06	1.0681
1.5	63.42	1.0676
2	53.51	1.0673
3	41.72	1.0656
4	34.69	1.0639
5	29.89	1.0618
6	26.36	1.0600
7	23.62	1.0584
8	21.41	1.0564
9	19.58	1.0544
10	18.03	1.0522
11	16.71	1.0503
12	15.55	1.0480
13	14.53	1.0461
14	13.63	1.0443
15	12.81	1.0422
16	12.08	1.0399
17	11.41	1.0379
18	10.80	1.0355
19	10.24	1.0336
20	9.72	1.0315
21	9.25	1.0294
22	8.81	1.0275
23	8.39	1.0254

Table 4.3: N estimated for A-CNT arrays as a function of V_{f}, evaluated using previously reported experimental data (see Figure 4.11).[43]

V_{f} [%]	N
1	4.30 ± 0.05
6	4.70 ± 0.03
10.6	4.90 ± 0.1
20	5.30 ± 0.05

4.4 Conclusions and Recommendations for Future Work

This Chapter presented experimental, theoretical, and simulation approaches utilized to quantify and model the evolution of the three-dimensional morphology of the CNTs that comprise A-CNT systems with packing proximity. The experimental results, based on 2D surface SEM analysis of waviness, indicate that w for the A-CNTs decreases non-linearly as a function of V_{f}, where $w \sim 0.2$ at $V_{\mathrm{f}} \approx 1\%$ CNTs and $w \sim 0.1$ at $V_{\mathrm{f}} \approx 20\%$ CNTs. Further work to elucidate the origin of the observed waviness reduction is required, and future study of the morphology of A-CNT arrays in three dimensions *via* a newly developed quantitative electron tomography technique is planned.[157] Using the developed multi-scale simulation capable of modeling $> 10^5$ CNTs with realistic stochastic morphologies, this Chapter shows that oversimplifying or neglecting the CNT waviness can lead to errors in Γ that may exceed 10%, and that the ideal hexagonal close packing is best suited for A-CNT arrays with minimal waviness, whereas square close packing ($N = 4$) works best for A-CNT arrays with noticeable waviness ($w > 0.1$). Using the scaling of Γ and w as a function of V_{f},[40,43] the simulation shows that N increases much faster than previously expected as the A-CNT arrays are being densified. Since the inter-CNT proximity effects can strongly influence the evolution of the packing morphology of A-CNT arrays, but their precise contribution is not currently known, additional work is required to quantify the impact of CNT-CNT interactions as a function of Γ. Once the CNT proximity interactions can be accurately described as a function of the inter-CNT separation, the simulation scheme developed here could be extended to predict the evolution of the CNT morphology during packing, potentially enabling the design and fabrication of higher performing devices, such as membranes for water filtration whose permeability directly relates to the morphology,[70,146] or CNT architectures with tunable mechanical behavior, where the waviness governs the stiffness of the CNTs.[40]

In the next Chapter, the morphology information presented here, along with the simulated A-CNT arrays with realistic stochastic CNT morphologies, are used to analyze the underlying physical mechanisms that govern the mechanical behavior of A-CNT arrays during elastic deformation.

Chapter 5

Elastic Modeling of Aligned Carbon Nanotube Arrays

To predict the mechanical behavior of A-CNT arrays comprised of CNTs that cannot be approximated using a highly simplified collimated morphology, the elastic response of A-CNTs with stochastic three-dimensional morphologies must be modeled and analyzed. Although the mechanical properties of A-CNT arrays were modeled previously in a number of ways, these existing models could not properly account for the random morphology of the CNTs that comprise aligned arrays, and this Chapter presents the methodology used to utilize the three-dimensional morphology information of the CNTs that comprise the simulated A-CNT arrays (from Chapter 4) to evaluate the effective axial elastic modulus of A-CNT arrays as a function of packing proximity. Using this model, the mechanical behavior of A-CNT arrays can be predicted, and the orders of magnitude enhancement of stiffness previously observed during densification can be explained from the underlying physics, enabling more precise tuning of the elastic properties of A-CNTs. This is achieved by evaluating the compliance contribution of the four deformation mechanisms of a wavy CNT: extension, shear, bending, and torsion.[1]

5.1 Compliance Prediction of A-CNT Arrays

As briefly mentioned above, this Chapter presents a mechanics framework that utilizes 3D A-CNT morphology information to model the elastic behavior of A-CNT arrays. In this Section, previously reported results for experimentally determined stiffness of A-CNT arrays are outlined, and recent developments that enable better prediction of the stiffness of A-CNT arrays through the incorporation of more representative descriptions of the CNT morphology into mechanical models are discussed.

---

[1] Parts of this Chapter previously appeared in Ref. 40

Early modeling efforts have shown that while the intrinsic Y, or wall modulus, of CNTs can be > 1 TPa in tension,[30–33,118] deviations from the normally assumed straight cylindrical column structure of the CNTs can lead to orders of magnitude reductions in stiffness coefficients of A-CNTs.[158,168,169] These reductions in stiffness could originate from the large anisotropy in the axial E_{eff} of a CNT, where Y has a value similar to the in plane modulus of graphene,[180] but G can be as low as 0.1 GPa,[118] a value similar to the transverse shear modulus of turbostratically stacked graphene/graphite.[116,117] Previous work has ascribed the very low E_{eff} of A-CNTs to compression induced buckling of A-CNTs, but buckling can only account for $\sim 10\times$ reduction in E_{eff} ($\rightarrow E_{\text{eff}} \sim 10 - 100$ GPa),[102,181] and not the 4 to 6 orders of magnitude reductions in E_{eff} reported for A-CNT arrays ($\rightarrow E_{\text{eff}} \sim 1 - 100$ MPa).[38,102,181–189] See Figure 5.1 for an illustration of A-CNTs buckling under compression (Figure 5.1a), and the resulting stress-strain curve and E_{eff} for A-CNTs (Figure 5.1b). To explain the order of magnitude overpredictions of E_{eff} in A-CNTs, more recent studies have developed model that are capable of better approximating the A-CNT morphology, and have shown that waviness is the primary morphological effect responsible for the large reduction in the stiffness of CNTs in A-CNT arrays.[102]

However, while recent work has shown that more representative descriptions of the A-CNT array morphology can account for the large reductions previously reported for E_{eff} of A-CNTs,[102] these results were obtained using a highly idealized sinusoidal CNT geometry and contained de-

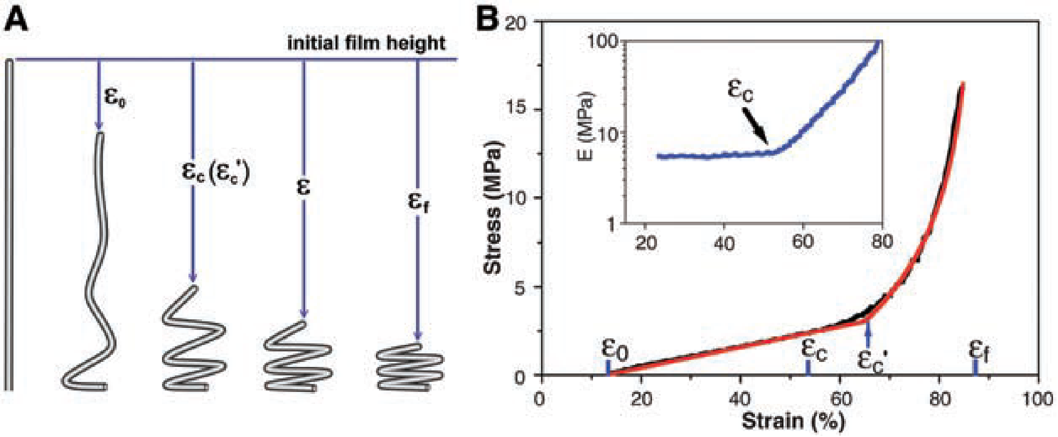

Figure 5.1: Elastic behavior of A-CNTs under compression as presented by Cao et al.[181] (a) Illustration of the buckling modes of A-CNTs. (b) Resulting stress-strain curve and E_{eff} for A-CNTs.

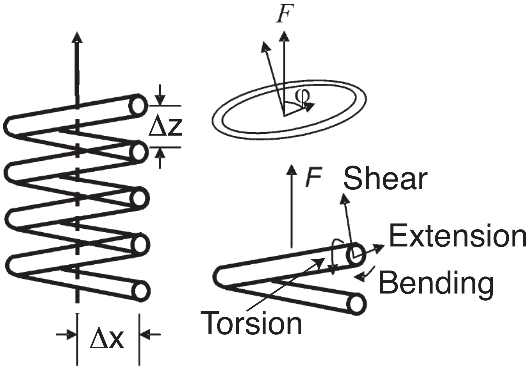

Figure 5.2: Deformation mechanisms of a carbon nanocoil as presented by Chen et al.[47]

formation mechanisms, meaning that the physics underlying the CNT mechanical behavior were not explored in detail. The deformation mechanisms that contribute to the elastic response of wavy A-CNTs were previously explored in detail for a similar one-dimensional carbon system, the carbon nanocoil, and showed that there are significant contributions by the torsion and shear mechanisms that are normally neglected.[47,190] However, while these results are applicable to the simple helix geometry that carbon nanocoils exhibit, wavy A-CNTs exhibit a more complicated three dimensional morphology that cannot be adequately described using simple geometrical models. In this Chapter, the three-dimensional descriptions of the A-CNT array morphology are used to study the contribution of (axial) stretching, shear, bending, and torsion on the deformation of wavy CNTs, explaining that the observed large reductions in stiffness of CNT arrays originate from the deformation mechanisms (torsion and shear) dominated by the low G exhibited by A-CNTs.

This Section reviewed the experimentally determined underwhelming E_{eff} of A-CNTs, and discussed how incorporation of representative descriptions of the 3D morphology of A-CNTs can enable more accurate prediction of their E_{eff}. In the remainder of this Chapter, the analysis utilized to evaluate the mechanical behavior of A-CNT arrays from their 3D morphology is presented, and the scaling of E_{eff} as a function of CNT packing proximity is discussed.

5.2 Modeling of A-CNT Mechanical Behavior

As briefly discussed in the previous Section, the stiffness of a wavy CNT is analyzed using the principle of virtual work, similar to a previous study of the deformation of a carbon nanocoil.[47] In this analysis, four deformation mechanisms are considered: extension, shear, bending, and torsion. See Figure 5.3 inset for an illustration of the four modes that contribute to the deformation of a wavy

CNT. Similar to the previous analysis,[47] one unit cell, which is defined as a segment bound by two nodes in the z direction, is used to evaluate the contribution of the four deformation modes. However, unlike the previously explored helical carbon nanocoils,[47] the wavy CNTs simulated here are stochastic, *i.e* a random walk in three dimensions, such that the geometry of the unit cell in the $x-y$ plane needs to be determined numerically for each node of a wavy CNT instead of being defined analytically as would be the case for other deterministic descriptions of waviness, *e.g.* sine waves or helices. The correlations used to define the unit cell are presented in Section 5.2.1, the morphology dependent effective A-CNT compliance and E_{eff} of A-CNTs are discussed in Section 5.2.2, and a guide for applying this mechanical analysis to other NF systems is presented in Section 5.3.

5.2.1 Unit Cell Analysis

Using Δr and Δz as defined in Chapter 4, the extension ($\xi_{\text{extension}}$), shear (ξ_{shear}), bending (ξ_{bending}), and torsion (ξ_{torsion}) contributions can be derived from the correlations previously reported for a carbon nanocoil and are as follows:[47]

$$\xi_{\text{extension}} = \left(\frac{\Delta z^2}{\Delta r^2 + \Delta z^2}\right)\left(\frac{L_{\text{3D}}}{YA}\right) = \left(\frac{\zeta(w)^2}{4\chi(w)^2 + \zeta(w)^2}\right)\left(\frac{L_{\text{3D}}}{YA}\right) \tag{5.1a}$$

$$\xi_{\text{shear}} = \left(\frac{\Delta r^2}{\Delta r^2 + \Delta z^2}\right)\left(\frac{L_{\text{3D}}}{GA}\right) = \left(\frac{4\chi(w)^2}{4\chi(w)^2 + \zeta(w)^2}\right)\left(\frac{L_{\text{3D}}\alpha}{GA}\right) \tag{5.1b}$$

$$\xi_{\text{bending}} = \left(\frac{\Delta r^2 \Delta z^2}{\Delta r^2 + \Delta z^2}\right)\left(\frac{L_{\text{3D}}}{YI}\right) = \left(\frac{\chi(w)^2\zeta(w)^2\lambda^2}{4\chi(w)^2 + \zeta(w)^2}\right)\left(\frac{L_{\text{3D}}}{YI}\right) \tag{5.1c}$$

$$\xi_{\text{torsion}} = \left(\frac{\Delta r^4}{\Delta r^2 + \Delta z^2}\right)\left(\frac{L_{\text{3D}}}{GJ}\right) = \left(\frac{4\chi(w)^4\lambda^2}{4\chi(w)^2 + \zeta(w)^2}\right)\left(\frac{L_{\text{3D}}}{GJ}\right) \tag{5.1d}$$

where $L_{\text{3D}} = \tau(w)_{\sin}\Delta z$ and represents the arc length of the CNT between the two nodes in the z direction (see Chapter 4 for the scaling of $\tau(w)_{\sin}$ with w), A is the cross-sectional area of the CNTs defined by the inner ($D_{\text{i}} \approx 5$ nm) and outer ($D_{\text{o}} \approx 8$ nm)[28,45] diameters which are representative of the CNTs studied here and in Ref. 29, I and J are the area and polar (*i.e.* torsion) moments of inertia of a hollow solid (i.e. no nested walls) cylinder, and α is the shear coefficient for a multiwalled CNT (MWCNT) that has the following form:[118]

$$\alpha = \frac{7 + 6\nu\left(1 + (D_{\text{i}}/D_{\text{o}})^2\right)^2 + (20 + 12\nu)(D_{\text{i}}/D_{\text{o}})^2}{6(1+\nu)\left(1 + (D_{\text{i}}/D_{\text{o}})^2\right)^2} \tag{5.2}$$

where ν is the Poisson ratio with an assumed value of $\nu \sim 0.3$ ($\rightarrow \alpha \approx 1.3$ for the CNTs studied here). Using these correlations, the mechanical behavior of CNTs with waviness defined by the mean and uncertainty in w (see Chapter 4) is studied *via* an array of 10^5 simulated CNTs, and the physical origin of the scaling of the CNT array stiffness as a function of CNT proximity is evaluated in the next Sections.

5.2.2 A-CNT Array Effective Modulus from Compliance Contribution of Deformation Modes

Using Eq. 5.1 and V_f, $K(w)$ and $E_\mathrm{cnt}(w)$ can be defined as follows:

$$K(w) = (\xi_\mathrm{extension} + \xi_\mathrm{shear} + \xi_\mathrm{bending} + \xi_\mathrm{torsion})^{-1} \tag{5.3a}$$

$$E_\mathrm{cnt}(w) = K(w)\left(\frac{L_\mathrm{3D}}{A}\right)V_\mathrm{f} \tag{5.3b}$$

5.3 Guide for Applying This Simulation Framework to Other Aligned Nanofiber Systems

The 3D morphology and mechanical behavior of other A-CNT arrays, and NF arrays in general, can be predicted using the simulation framework presented here by following the steps outlined below:

Part I 3D morphology initialization

1. Determine the CNT geometry (*i.e.* inner and outer diameters), and the value and/or range of V_f that will be used in the study. These parameters can either be assumed, or be experimentally/theoretically evaluated.
2. Evaluate the average minimum and maximum inter-CNT separations (Γ_min and Γ_max). This can be done by assuming a packing coordination (either square or hexagonal close packing), or preferably using the model previously developed for quantifying the packing morphology of CNTs.[43,46] These values are evaluated using the CNT outer diameter and V_f, and are used to define the confining area of each CNT.
3. Approximate w of the CNTs. This can be done by either assuming the value and/or scaling of w with V_f, or by experimentally evaluating the evolution of w with packing

proximity (as detailed in Chapter 4). If the average tortuosity (τ) of the CNTs is known instead of w, τ can be converted to w (see Chapter 4).

4. Initialize the confining box of each CNT starting at the first node. For simplicity, place the first node in the middle of the confining area, and define the separation of each node of each CNT in the $x-y$ place using Γ_{min} and Γ_{max}.
5. Place the second node using the position of the first node, and a small $x-y$ plane displacement evaluated using the waviness amplitude λ (λ is set as the average inter-CNT separation here), w, and a normally distributed random number with a value ranging from 0 to 1 (*e.g.* 'rand' in MATLAB). The displacement of the second node in the z direction should be evaluated using the number of nodes that comprise each λ (*i.e.* the simulation resolution, where 20 nodes for each λ was used in this study).
6. Repeat this process until all the nodes for each CNT are generated. If a node falls outside of the confining area, place that node at the boundary.
7. Evaluate the average arc length ($\equiv \tau$) of each CNT in the array, and adjust the node displacement in the z direction until $\tau = \tau(w)_{\text{sin}}$.
8. Sample and record the average $x-y$ ($\rightarrow \Delta r$) and z ($\rightarrow \Delta z$) displacements for $\lambda/2$, and evaluate the coefficients $\chi(w)$ and $\zeta(w)$.

Part II effective axial elastic modulus prediction

1. Input the CNT geometry, intrinsic moduli, and morphology parameters into Eqs. 5.1 and 5.3.
2. Solve numerically at each V_{f} by sampling the stiffness of each CNT (*i.e.* using the unit cells that comprise the CNT and their respective τ), and average over the entire CNT array.
3. Repeat for the entire V_{f} range.

5.4 Results and Discussion

In this Section, the contribution of the deformation modes to the effective A-CNT axial compliance is presented (see Section 5.4.1), and the scaling of $E_{\text{cnt}}(w)$ as a function of packing proximity is discussed (see Section 5.4.2).

5.4.1 Deformation Mode Contribution to Effective A-CNT Compliance

Contributions of the extension, shear, bending, and torsion deformation modes (see Figure 5.3 for illustration) to the effective compliance of A-CNT arrays as a function of w can be found in Figure 5.3 ($V_f \sim 1\%$ CNTs) and Figure 5.4 ($V_f \sim 5\%$, 10%, 20%, and 40% CNTs). As Figure 5.3 shows, at the experimentally measured $w \approx 0.2 \pm 0.1$ (from Chapter 4) for ~ 1 vol. % CNTs, the torsion mechanism by far dominates the effective compliance of A-CNT arrays, with the shear deformation mechanism a distant second. As Figure 5.4a and Figure 5.4b show, the shear and torsion deformation mechanisms both dominate (with approximate equal contribution) the effective A-CNT array compliance at the measured w for $V_f \sim 5\%$ and 10%. Finally, Figure 5.4c and Figure 5.4d demonstrate that at high V_f ($\gtrsim 20\%$) the shear deformation mechanism by far dominates the effective compliance of A-CNT arrays, with the torsion deformation mechanism a distant second. These results show that the very low G ($\rightarrow Y/G \sim 10^3$) of A-CNT arrays leads to significant stiffness losses due to shear and torsion deformations, and that the bending deformation mechanism is not a source of significant stiffness losses in this specific A-CNT system.

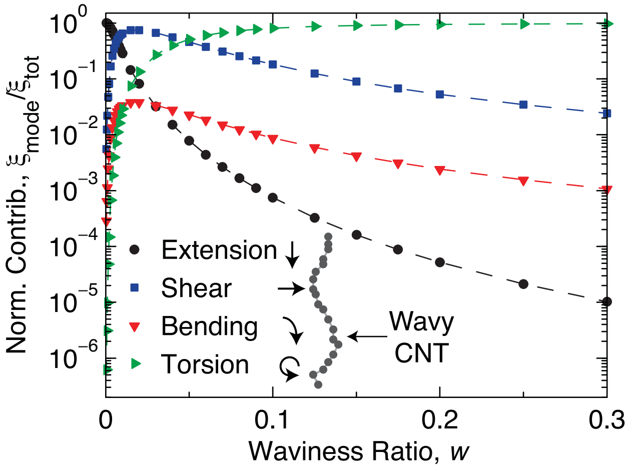

Figure 5.3: Illustration and scaling of the compliance contribution ($\rightarrow \xi_{mode}/\xi_{tot}$ where $\xi_{tot} = \sum \xi$) of the four deformation modes as a function of the waviness ratio (w) at CNT volume fraction (V_f) of $V_f = 1\%$ CNTs.

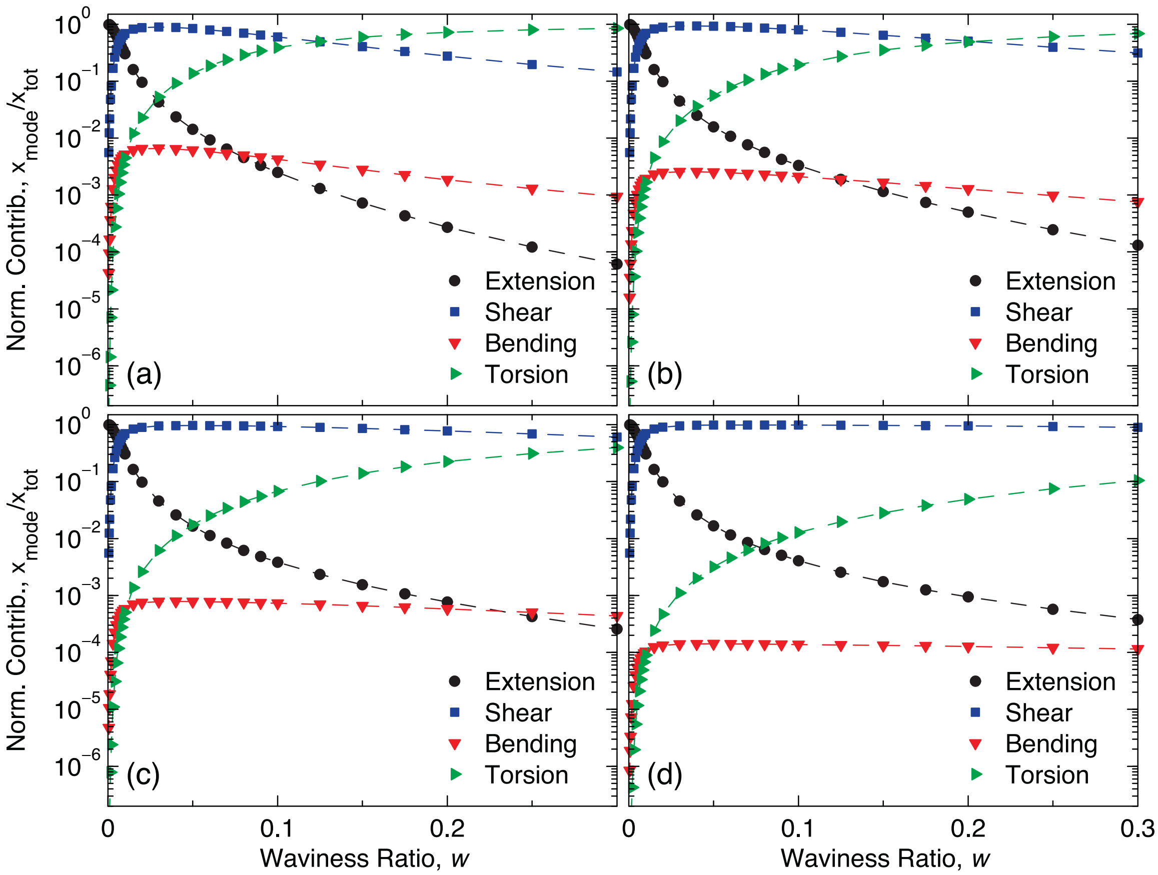

Figure 5.4: Contribution of extension, shear, bending, and torsion deformation mechanisms (see Eq. 5.1 to the effective compliance ($\rightarrow \xi_{\text{mode}}/\xi_{\text{tot}}$ where $\xi_{\text{tot}} = \sum \xi$) of wavy CNTs as a function of the waviness ratio (w) and CNT volume fraction. (a) Deformation mode contributions for CNTs with $V_{\text{f}} \approx 5\%$. (b) Deformation mode contributions for CNTs with $V_{\text{f}} \approx 10\%$. (c) Deformation mode contributions for CNTs with $V_{\text{f}} \approx 20\%$. (d) Deformation mode contributions for CNTs with $V_{\text{f}} \approx 40\%$.

5.4.2 A-CNT Array Effective Modulus Scaling

See Figure 5.5a for a plot of the ratio of the axial modulus scaling of wavy CNTs ($\rightarrow E_{\text{cnt}}(w)$) from Eq. 5.3 normalized by the modulus of collimated CNTs ($\rightarrow E_{\text{cnt}}(0)$) for $G \sim 1$ GPa. As Figure 5.5a demonstrates, CNT waviness significantly impacts their mechanical properties, and leads to a two orders of magnitude drop in modulus ($\rightarrow E_{\text{cnt}}(w)/E_{\text{cnt}}(0) \gtrsim 10^{-2}$) at $w \sim 0.05$ and three orders of magnitude drop in modulus ($\rightarrow E_{\text{cnt}}(w)/E_{\text{cnt}}(0) \gtrsim 10^{-3}$) at $w \gtrsim 0.2$ for CNTs with $D_{\text{o}} \sim 8$ nm. This large change in $E_{\text{cnt}}(w)$ is attributed to the small value of G in the CNTs, which is more than three orders of magnitude smaller than Y, and leads the shear (see Eq. 5.1b) and torsion (see Eq. 5.1d) deformation modes to contribute $\gtrsim 98\%$ of the effective compliance of the wavy CNTs at $w \gtrsim 0.05$ (see Section 5.4.1). Since the A-CNTs studied here are treated as non-interacting and

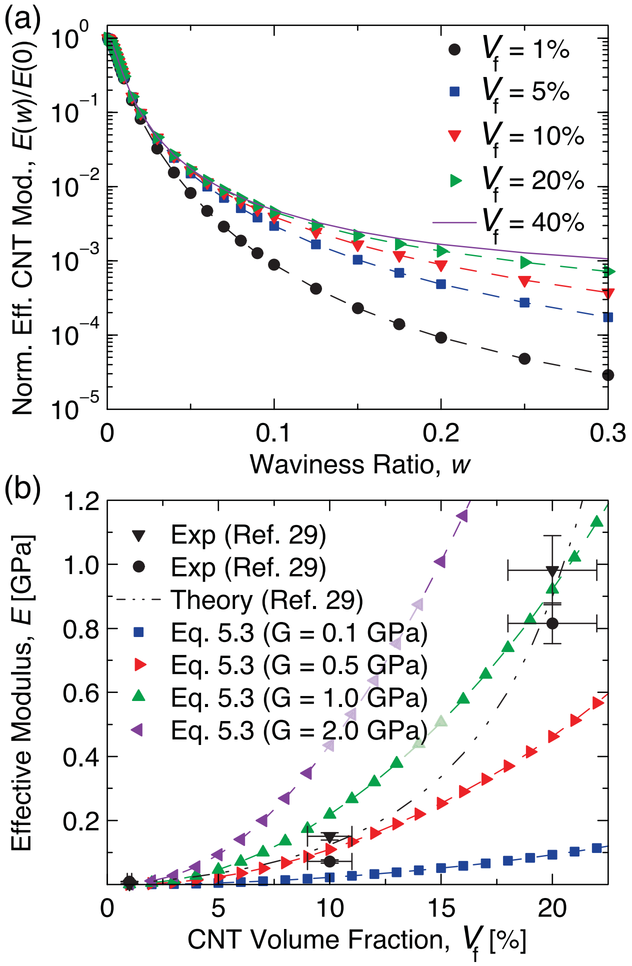

Figure 5.5: Elastic response of wavy aligned CNTs. (a) Plot of the effective axial modulus of wavy CNTs ($E_{\mathrm{cnt}}(w)$) normalized by the intrinsic modulus of straight CNTs ($E_{\mathrm{cnt}}(0)$) as a function of w and V_{f} indicating that waviness can lead to orders of magnitude reductions in modulus. (b) Plot comparing the scaling of the effective modulus with V_{f} ($\rightarrow E_{\mathrm{cnt}}(V_{\mathrm{f}})$) for the 10^5 simulated wavy CNTs (via Eq. 5.3) to the previously reported experimental and theoretical scaling of $E_{\mathrm{cnt}}(V_{\mathrm{f}})$.[29] This plot shows that the shear modulus (G) of the CNTs, which dominates the torsion and shear deformation mechanisms, governs the scaling of $E_{\mathrm{cnt}}(V_{\mathrm{f}})$.

cannot escape their confining volumes, the size of the confining box was considered by varying V_{f} from 1% CNTs to 40% CNTs. As Figure 5.5a illustrates, the as-grown CNT arrays ($V_{\mathrm{f}} \approx 1\%$ CNTs), which have waviness characterized by the largest local curvature and experience a larger torsion contribution ($\gtrsim 50\%$ of the effective CNT compliance at $w \gtrsim 0.05$, see Figure 5.3), exhibit the largest reductions in effective modulus due to waviness, *e.g.* $E_{\mathrm{cnt}}(w)/E_{\mathrm{cnt}}(0) \gtrsim 10^{-4}$ at $w \sim 0.20$, while densified CNTs ($V_{\mathrm{f}} \gtrsim 5\%$ CNTs), which have incrementally smaller local curvature and exhibit a larger shear contribution ($\gtrsim 80\%$ of effective compliance at $w \gtrsim 0.02$, see Section 5.4.1), are relatively less sensitive to waviness and see smaller reductions in the CNT effective stiffness with w, *e.g.* $E_{\text{cnt}}(w)/E_{\text{cnt}}(0)$ for $V_{\text{f}} \approx 40\%$ CNTs is $\gtrsim 3\times$ larger than $E_{\text{cnt}}(w)/E_{\text{cnt}}(0)$ for $V_{\text{f}} \approx 5\%$ CNTs at $w \gtrsim 0.10$. Using the scaling of w with V_{f} ($\rightarrow w(V_{\text{f}})$), Eq. 5.3 can be used to predict the mechanical behavior of CNT arrays as a function of their V_{f} ($\rightarrow E_{\text{cnt}}(V_{\text{f}})$). See Figure 5.5b for a plot of $E_{\text{cnt}}(V_{\text{f}})$ for 0.1 GPa $\lesssim G \lesssim$ 2 GPa evaluated using 10^5 simulated wavy CNTs ($\rightarrow$ standard error of $\lesssim 0.5\%$). As Figure 5.5b demonstrates, the value of G has a very strong impact on $E_{\text{cnt}}(V_{\text{f}})$, where $G \approx 0.9 \pm 0.3$ GPa agrees very well with the previously reported experimental values of $E_{\text{cnt}}(V_{\text{f}})$ that were approximated using two nanoindentation tip geometries (spherical and Berkovich).[29] In the previous study, the observed large increase in stiffness was explained through a first order theoretical model for collimated ($\rightarrow w = 0$) CNTs that uses the average inter-CNT separation at a certain V_{f} ($\rightarrow$ ranging from 10 nm to 80 nm), and the minimum inter-CNT separation (~ 5 nm) that is controlled by CNT proximity effects, to approximate $E_{\text{cnt}}(V_{\text{f}})$ given a starting point of $E_{\text{cnt}}(V_{\text{f}} = 1\%) \sim 4$ MPa. While the results of the previously reported theoretical model are in good agreement with the results of the simulated wavy CNTs with $G \approx 0.9 \pm 0.3$ GPa reported here (see Figure 5.5b), the simulation results give a clear physical origin for the observed mechanical behavior of the CNT arrays, *i.e.* deformation occurs mostly through shear and torsion, whereas the theoretical model, which had no access to information relating the CNT waviness to their elastic properties,[29] could not provide the morphological origin of the observed behavior. These results illustrate that the inclusion of a representative description of the CNT waviness is necessary to properly describe their mechanical behavior from the underlying physics.

5.5 Conclusions and Recommendations for Future Work

This Chapter presented a modeling framework that allows the integration of the 3D morphology information into mechanical property prediction for A-CNT arrays. Modeling results indicate that the CNT waviness, quantified *via* w, is responsible for more than three orders of magnitude reduction in the effective axial A-CNT array stiffness. Also, by including information on the V_{f} scaling of both the mean value and statistical uncertainty of the CNT waviness, the simulation is able to replicate the experimentally measured axial A-CNT array elastic modulus,[29] and show that the observed non-linear enhancement of the array stiffness as a function of the CNT close packing originates from the low G of the CNTs which governs the shear and torsion deformation mechanisms. Additionally, the modeling results show that, while the bending deformation mechanism is normally assumed to dominate the effective compliance contribution in A-CNT systems, shear and torsion actually dominate in the experimental regime of waviness. Also, once additional information on the morphology of A-CNT arrays in three dimensions in available, the CNT-CNT electrostatic interactions in the small ($\lesssim 10$ nm) and intermediate ($\sim 10 - 100$ nm) regimes, which may not be purely van der Waals in nature but lead to bundle formation and significant moisture adsorption in ambient conditions,[46] will be analyzed, and their contribution to the elastic response of A-CNT arrays will be modeled.

In the next Chapter, the mechanical analysis presented here, along with the 3D morphology information from Chapter 4, are used to study the mechanical behavior of an A-PNC.

Chapter 6

Aligned Carbon Nanotube Polymer Matrix Nanocomposites

To predict the mechanical behavior of A-PNCs made using CVD grown A-CNT arrays, where neglecting or assuming that the A-CNT waviness is of a simple function form is not adequate. Though the effective elastic modulus of A-PNCs was modeled both analytically and numerically in many previous studies, these previous works all approximated the waviness of the CNTs that comprise the A-PNCs using unrepresentative sinusoidal and/or helical functional forms, and this Chapter presents the approach used to combine the effective stiffness contribution of the stochastic waviness A-CNT array (from Chapter 5) with that of the polymeric matrix to calculate the effective A-PNC axial elastic modulus scaling with V_{f}.

This Chapter presents the modeling approach used to predict the effective elastic modulus of A-PNCs using the mechanical behavior of A-CNT arrays quantified in Chapter 5, and a constant elastic modulus for the polymeric matrix material. This is achieved by applying rule of mixtures, and by assuming that the polymeric matrix effectively eliminates the torsion deformation mechanism of the CNTs that comprise the A-PNCs.[1]

6.1 Elastic Axial Stiffness Prediction for A-PNCs

As briefly mentioned above, this Chapter presents a mechanics framework that utilizes 3D A-CNT morphology information to model the elastic behavior of A-PNCs. In this Section, previously reported results for experimentally determined stiffness of A-PNCs are reviewed, and recent developments that enable better prediction of the effective stiffness of A-PNCs through the incorporation of more representative descriptions of the CNT morphology into mechanical models are discussed.

---

[1] Parts of this Chapter previously appeared in Ref. 42 and Ref. 191

CNTs were the subject of many previous studies on polymer nanocomposites comprised of aligned (e.g. A-CNT arrays)[50,158,192–196] and unaligned (e.g. CNT powders)[156,168–172,195–213] CNT morphologies. The results of these previous studies, which used pure analytical (e.g. Mori-Tanaka model used in conjunction with the classic Eshelby solution),[170,192,193,197,198,200–202] pure numerical (e.g. finite element models coupled with experiments),[195,203] or hybrid approaches of continuum micromechanics,[168,169,171,172,205–209] are in overall agreement that any curvature (i.e. waviness) of the CNTs significantly reduces their effective reinforcement modulus when compared to idealized straight (i.e. collimated) CNTs. Also, previous work on A-PNCs has demonstrated that the CNT waviness could lead to composite moduli that are more than an order of magnitude lower than the ones predicted by rule of mixtures analysis of collimated CNTs.[50,158] See Figure 6.1 for a plot comparing the experimentally determined E_{pnc} from Ref. 158 (Figure 6.1a) and Ref. 50 (Figure 6.1b) showing that rule of mixtures for $Y > 100$ GPa ($\rightarrow Y/E_{\text{pm}} > 50$) does not lead to accurate predictions of the E_{pnc} scaling with V_{f}. Additionally, as noted by Chapter 4, the waviness

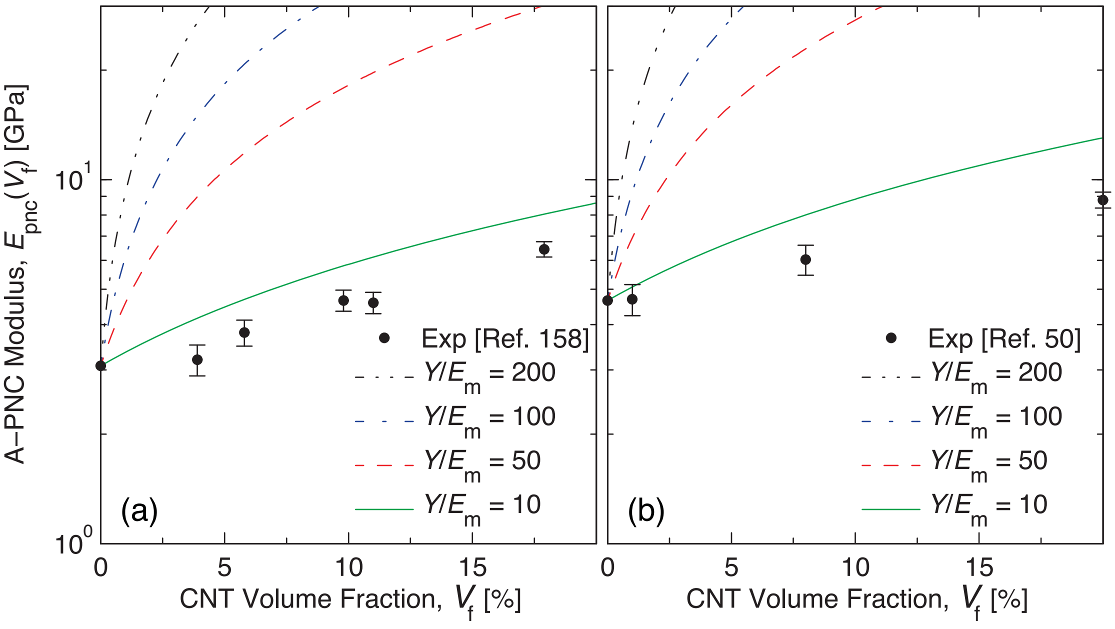

Figure 6.1: Experimentally determined and rule of mixtures predicted V_{f} scaling of E_{pnc}. (a) Plot comparing the experimental scaling of $E_{\text{pnc}}(V_{\text{f}})$ to the values predicted by rule of mixtures for $E_{\text{pm}} \approx 3.1$ GPa showing the large overpredictions of rule of mixtures.[158] (b) Plot comparing the experimental scaling of $E_{\text{pnc}}(V_{\text{f}})$ to the values predicted by rule of mixtures for $E_{\text{pm}} \approx 4.7$ GPa showing again the orders of magnitude overpredictions of E_{pnc} by rule of mixtures.[50]

of the CNTs is significantly reduced when V_f is increased.[43,157,158] However, existing theoretical and numerical models can only describe the CNT waviness using rudimentary approaches, such as assuming a sinusoidal or helical functional forms,[168–172,179] and cannot account for the scaling of w, a common measure for quantifying waviness, with V_f.

As discussed in the previous Chapter, oversimplifications of the CNT morphology lead to non-representative predicted stiffness contributions of the CNTs to the effective elastic modulus of the A-PNCs,[40,102] thereby hindering property prediction capabilities. Additionally, while more complete descriptions of the CNT morphology, *e.g.* the ones presented in Chapter 4, are slowly becoming available, such information cannot be readily integrated into existing theoretical models that rely on simple CNT geometries to create meshes/RVEs. In this Chapter, the three-dimensional descriptions of the A-CNT array morphology are used to directly study the contribution of extension, shear, bending, and torsion to the effective compliance of CNTs in A-PNCs using an analysis similar to that of Chapter 5, and to show that the observed A-PNC stiffness enhancement reported for high V_f A-PNCs depends on E_pm and is strongly influenced by the waviness of the underlying A-CNTs. In the remainder of this Chapter, the analysis utilized to evaluate the mechanical behavior of A-PNCs from their 3D morphology is presented, and the scaling of E_pnc as a function of CNT packing proximity is discussed.

6.2 Modeling of A-PNC Elastic Behavior

This Section presents the modified scaling of w (from Chapter 4) used to simulate the morphology of the A-CNTs that comprise A-PNCs (see Section 6.2.1), and the modifications to the mechanical analysis (from Chapter 5) that were made to accommodate the presence of a polymeric matrix (see Section 6.2.2).

6.2.1 Waviness Evolution

As discussed in Chapter 4, the waviness of the A-CNT arrays as a function of V_f ($\rightarrow w(V_\mathrm{f})$) was previously evaluated from SEM images of the cross-sectional morphology of A-CNT arrays using a simple sinusoidal amplitude-wavelength ($\rightarrow a/\lambda$) definition of w.[40] The results presented in Chapter 4 show that CNT confinement leads both the mean values and standard errors of w to decrease significantly from $\approx 0.20 \pm 0.02$ at $V_\mathrm{f} \approx 1\%$ CNTs to $\approx 0.10 \pm 0.01$ at $V_\mathrm{f} \approx 20\%$ CNTs, and that the following scaling relation for $w(V_\mathrm{f})$ is representative:[40,42]

$$w(V_\mathrm{f}) = \Lambda(-0.04967(V_\mathrm{f})^{0.3646} + 0.2489 \pm (-0.0852(V_\mathrm{f})^{0.2037} + 0.2100)/\sqrt{n}). \tag{6.1}$$

where $n = 30$ CNTs,[40] and Λ is a scaling factor.[42] Λ physically represents the impact of polymer infusion, and subsequent curing, on the morphology evolution of the CNTs that comprise the A-PNC, and has a value of $0 \leq \Lambda \leq 1$, where $\Lambda = 1$ indicates no change in CNT morphology (i.e. waviness of CNTs that comprise the A-PNC is the same as a pure CNT array), and $\Lambda < 1$ indicates that polymer infusion reduces the CNT waviness. $w(V_\mathrm{f})$ from Eq. 6.1 will be used in the remainder of this Chapter to both evaluate the impact of waviness on the mechanical properties of the A-PNCs, and to approximate the influence of polymer wetting on the waviness of the CNTs.

6.2.2 Mechanical Modeling and Effective CNT Modulus

The stiffness of wavy CNTs is analyzed using the principle of virtual work similar to the analysis presented in Chapter 5 for the elastic behavior of wavy A-CNT arrays,[40] which was based on a previous study of the deformation of carbon nanocoils.[47] Since the polymer matrix will restrict the movement of the CNTs during deformation, the analysis used here assumes that deformation *via* torsion is minimal, consistent with the findings of a recent study of A-PNC deformation during compression,[214] and thereby consists of three primary deformation mechanisms: extension, shear, and bending. An illustration of the three modes that contribute to the deformation of a wavy CNT in the A-PNC can be found in Figure 6.2. The compliance contributions of $\xi_\mathrm{extension}$, ξ_shear, and ξ_bending can be used with V_f to evaluate $K(w)$, $E_\mathrm{cnt}(w)$, and $E_\mathrm{pnc}(V_\mathrm{f})$ from rule of mixtures as follows:

$$\xi_\mathrm{extension} = \left(\frac{\Delta z^2}{\Delta r^2 + \Delta z^2}\right)\left(\frac{L_\mathrm{3D}}{YA}\right) \tag{6.2a}$$

$$\xi_\mathrm{shear} = \left(\frac{\Delta r^2}{\Delta r^2 + \Delta z^2}\right)\left(\frac{L_\mathrm{3D}\alpha}{GA}\right) \tag{6.2b}$$

$$\xi_\mathrm{bending} = \left(\frac{\Delta r^2 \Delta z^2}{\Delta r^2 + \Delta z^2}\right)\left(\frac{L_\mathrm{3D}}{YI}\right) \tag{6.2c}$$

$$K(w) = (\xi_\mathrm{extension} + \xi_\mathrm{shear} + \xi_\mathrm{bending})^{-1} \tag{6.2d}$$

$$E_\mathrm{cnt}(w) = K(w)\left(\frac{L_\mathrm{3D}}{A}\right) \tag{6.2e}$$

$$E_\mathrm{pnc}(V_\mathrm{f}) = E_\mathrm{cnt}(w(V_\mathrm{f}))V_\mathrm{f} + E_\mathrm{pm}(1 - V_\mathrm{f}) \tag{6.2f}$$

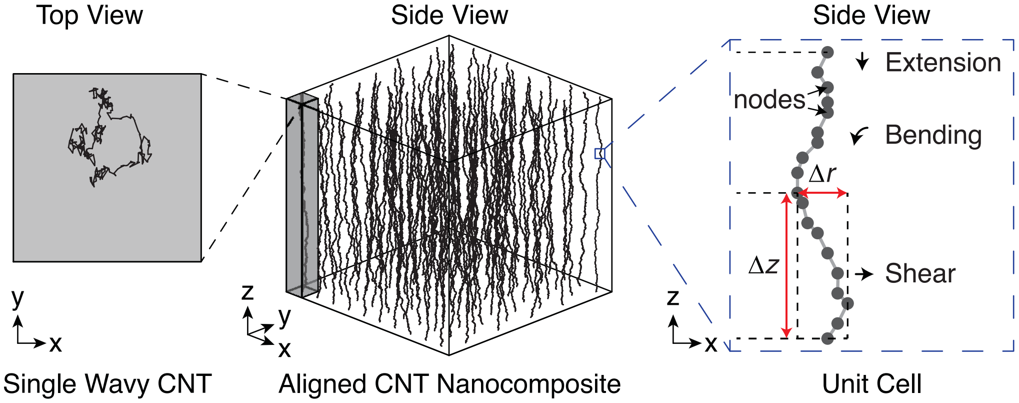

Figure 6.2: Top view of a simulated carbon nanotube (CNT) illustrating the two-dimensional random walk that comprises the waviness (left), side view of an aligned carbon nanotube polymer matrix nanocomposite (A-PNC) comprised of simulated wavy CNTs (center), and illustration of the unit cell used in the morphology and mechanical property analysis (right) showing the three CNT deformation modes that contribute to the elastic response of the wavy CNTs in the A-PNC.

where L_{3D} is the arc length of the two nodes in the z direction ($\rightarrow L_{3D} = \tau(w)\Delta z$ where $\tau(w)$ is the average CNT tortuosity defined by w using a sinusoidal waviness scheme),[40] E_{pm} is the elastic modulus of the polymer matrix, Y and G are the intrinsic moduli of the CNTs, A is the cross-sectional area of the CNTs (hollow cylinder geometry), I is the area moment of inertia of a hollow cylinder exhibiting D_i and D_o of the CNTs, and α is the shear coefficient.[118] Similar to Chapter 5, A and I are evaluated using $D_i \sim 5$ nm and $D_o \sim 8$ nm,[28,45] which are representative of the CNTs studied here and in Refs. 158 and 50. The analysis carried out here assumes that the Y of the CNTs is constant, and has a value of ~ 1 TPa,[12,30] while G (shear modulus of the CNTs) is governed by the elastic properties of the polymeric matrix, where $G \approx 1$ GPa when $G > E_{pm}$, and $G \approx E_{pm}$ when $G \leq E_{pm}$. Since previous morphology characterization of the polymeric matrix in the A-PNCs found no evidence that CNT confinement leads to polymer morphology changes characteristic of the formation of an interphase region,[22,50] Eqs. 6.2a−6.2f assume that the polymer matrix and wavy CNTs are perfectly bound (i.e. perfect load transfer). Previous work in Ref. 215 showed that when the interphase size is very small and the CNT-polymer interfacial strength is $\gtrsim 150$ MPa, as reported by recent studies,[117,216,217] the assumption of perfect bonding will have a very small impact on the predicted effective modulus of the A-PNCs. Also, another important feature of the simulated CNT arrays used in this study is that their CNT-CNT interactions, such as the van der Waals (vdW) interactions used in recent modeling effort,[139,147,173] are not included explicitly, but are instead integrated into the randomness of the CNTs in the arrays which implicitly accounts for fluctuations in their electrostatic interactions.[40] This avoids the assumption of an idealized electrostatic potential (e.g. vdW) that may not accurately describe the behavior of CNTs with native defects and adsorbed species.[46] The main difference between the current method, and modeling efforts that include electrostatic interactions, is that CNT arrays simulated here might have fewer CNT-CNT junctions, *i.e.* a more uniform local V_f, but since the CNTs in the A-PNCs are bound by the polymer matrix and cannot freely move, such an effect will be very small when averaged over a sample size of 10^5 CNTs.[40] Since this simulation framework can be used to study CNT arrays with V_f up to 40% CNTs (see Chapter 4),[40] a value near the maximum V_f achievable *via* mechanical densification of chemical vapor deposition grown ~ 8 nm outer diameter CNTs,[29] the results of this analysis will be physical for the entire range of experimentally accessible V_f of the A-PNCs studied here, although to date only V_f up to 20% has become available.

6.3 Results and Discussion

In this Section, the contribution of the deformation modes to the effective A-PNC compliance is presented (see Section 6.3.1), and the scaling of $E_\mathrm{pnc}(w)$ as a function of packing proximity is discussed (see Section 6.3.2).

6.3.1 Deformation Mode Contribution to Axial Effective A-PNC Compliance

The elastic response of a CNT in the A-PNC is governed by the longitudinal, *i.e.* Y, and shear, *i.e.* G, effective CNT moduli. Since G for the CNTs that comprise the A-PNC will likely not exceed the inter-plane modulus of graphite (~ 30 GPa), or be much smaller than $G \sim 1$ GPa previously reported for wavy CNTs,[40] Y/G was varied from $Y/G = 10$ to 1000 to represent the full of range of expected CNT effective stiffness contributions. See Figure 6.3 for the compliance contributions of each deformation mode ($\rightarrow \xi_\mathrm{mode}/\xi_\mathrm{tot}$ where $\xi_\mathrm{tot} = \sum \xi$). Figure 6.3a illustrates that for $Y/G = 10$, 100, 250, and 1000, extension governs the elastic response of the CNTs at $w < 0.03$ by contributing $> 50\%$ of the effective CNT compliance. However, at $w > 0.03$, the anisotropy of Y and G determines the deformation mechanism that dominates the elastic response, where $Y/G = 10$ leads to bending contributing $> 50\%$ of the effective CNT compliance (Figure 6.3c), while at $Y/G = 100$, 250, and 1000 the shear deformation mechanism contributes $> 50\%$ of the effective CNT compliance (Figure 6.3b). Also, while bending is the most important mode for $Y/G < 100$, Figure 6.3b demonstrates that the shear contribution to the effective CNT compliance is $> 10\%$, meaning that previous analyses that only focused on bending and extension may yield predicted A-PNC moduli that are not representative.[168,169] While recent simulation results are overall in agreement that the longitudinal stiffness of CNT arrays and their composites will be diminished by orders of magnitude as CNT waviness/curviness is increased,[102,171,172,195,202,209,213] this Section shows that the observed large stiffness losses originate from the large compliance contribution of the shear deformation mode governed by G (see Figure 6.3b), and that this effect can be mitigated by either choosing a stiffer matrix material ($\rightarrow$ smaller Y/G) or by decreasing the CNT waviness ($\rightarrow$ smaller w).

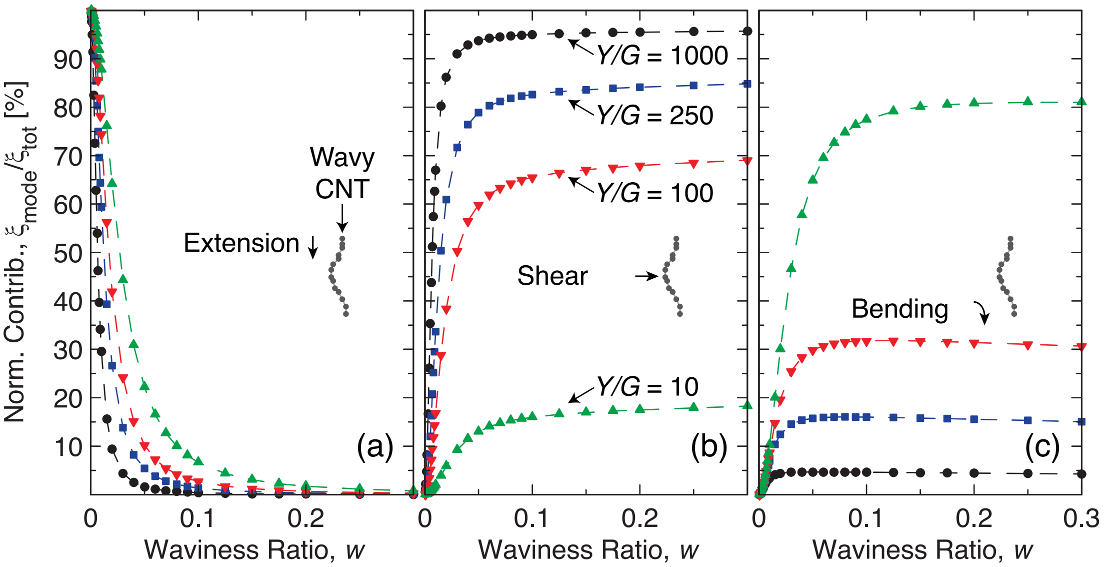

Figure 6.3: Contribution of extension, shear,and bending deformation mechanisms (see Eq. 6.2a) to the effective compliance ($\rightarrow \xi_{\text{mode}}/\xi_{\text{tot}}$ where $\xi_{\text{tot}} = \sum \xi$) of wavy CNTs that comprise the A-PNC as a function of the waviness ratio (w) and ratio of the intrinsic CNT longitudinal and shear moduli ($\rightarrow Y/G$) for $Y/G = 1000$ (●), $Y/G = 250$ (■), $Y/G = 100$ (▼), and $Y/G = 10$ (▲). (a) Extension mode contributions. (b) Shear mode contributions. (c) Bending mode contributions.

6.3.2 A-PNC Array Effective Modulus Scaling

As Figure 6.4 demonstrates, waviness has a strong impact on the effective CNT stiffness, where $w \gtrsim 0.05$ leads to $E_{\text{cnt}}(w)$ reductions $> 10\times$, and $w \gtrsim 0.3$ leads to $> 50\times$ reductions in $E_{\text{cnt}}(w)$. Additionally, Figure 6.4 shows that as the value of Y/G is reduced, which could also be achieved by using a stiffer polymeric matrix where $E_{\text{pm}} > G$ (e.g. $E_{\text{pm}} = 5$ GPa will reduce Y/G from 1000 to 200), $E_{\text{cnt}}(w)$ is enhanced by orders of magnitude. Using the scaling of $E_{\text{cnt}}(w)$, and the evolution of w with the CNT volume fraction (V_{f}) that was recently reported[40], the effective stiffness of A-PNCs with a variety of CNT V_{f} ($\rightarrow E_{\text{pnc}}(V_{\text{f}})$) can be predicted.

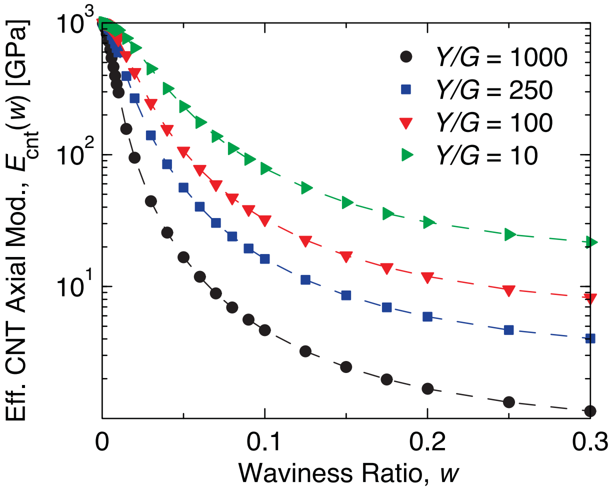

Figure 6.4: Plot of the effective modulus of wavy CNTs ($E_{\mathrm{cnt}}(w)$) as a function of the waviness ratio (w) demonstrating that waviness can lead to orders of magnitude reductions in stiffness.

$E_{\mathrm{pnc}}(V_{\mathrm{f}})$ was evaluated *via* Eqs. 6.2a–6.2f up to 20% CNTs, and was compared to the experimental and FEA results of two recent studies of A-PNCs comprised of ~ 8 nm diameter CNTs.[50,158] In both studies, E_{pm} was larger than the intrinsic G recently evaluated for these wavy A-CNTs (~ 1 GPa, see Chapter 5 for details), which means that the polymeric matrix effectively reinforces the CNTs in their transverse direction, and that CNTs contribute little to the PNC shear modulus such that $G \approx E_{\mathrm{pm}}$, an assumption consistent with previous FEA analyses of A-PNCs. See Figure 6.5a for $E_{\mathrm{pnc}}(V_{\mathrm{f}})$ evaluated experimentally, *via* FEA, and using the current simulation for $E_{\mathrm{pm}} = 3.1$ GPa ($\rightarrow Y/G \approx 323$) from Ref. 158, and Figure 6.5b for $E_{\mathrm{pnc}}(V_{\mathrm{f}})$ approximated by experiments, FEA, and the current simulation scheme for $E_{\mathrm{pm}} = 4.7$ GPa ($\rightarrow Y/G \approx 213$) from Ref. 50. Since polymer infusion might reduce the waviness of the CNTs, $E_{\mathrm{pnc}}(V_{\mathrm{f}})$ is evaluated for $w(V_{\mathrm{f}})$ that is scaled by $0.4 \leq \Lambda \leq 1.0$ (see Eq. 6.1). As Figure 6.5a demonstrates, the scaling of $w(V_{\mathrm{f}})$ has a very strong impact on $E_{\mathrm{pnc}}(V_{\mathrm{f}})$, where $\Lambda \approx 0.75$ ($\rightarrow\approx 25\%$ reduction in $w(V_{\mathrm{f}})$) agrees very well with the previously reported experimental values of $E_{\mathrm{pnc}}(V_{\mathrm{f}})$.[158] As Figure 6.5b demonstrates, scaling of w has a pronounced impact on $E_{\mathrm{pnc}}(V_{\mathrm{f}})$, where $\Lambda \approx 0.9$ ($\rightarrow\approx 10\%$ reduction in $w(V_{\mathrm{f}})$) agrees very well with the previously reported experimental values of $E_{\mathrm{pnc}}(V_{\mathrm{f}})$.[50]

It is hypothesized that capillary infusion affects both the waviness as well as the bundling, *i.e.* the number of CNT junctions that govern electron transport,[45,70,218] and the average separation of the A-CNTs, causing an effective reduction in waviness as suggested by the scaling of $E_{\mathrm{pnc}}(V_{\mathrm{f}})$ report here. In the previous studies, the observed enhancement in stiffness was explained through FEA performed on wavy CNTs described *via* a sinusoidal functional form of the waviness (See

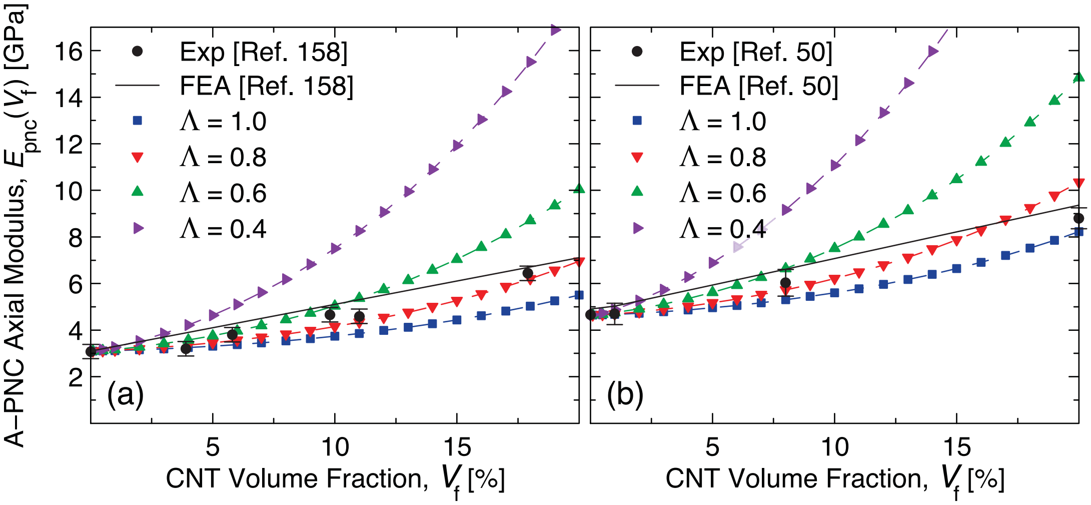

Figure 6.5: Axial modulus scaling with V_{f} for A-PNCs. (a) Plot comparing the scaling of $E_{\mathrm{pnc}}(V_{\mathrm{f}})$ as a function of the CNT morphology (via Eq. 6.1 $\rightarrow w(V_{\mathrm{f}})$ and Eqs. 6.2a−6.2f) to a previously reported experimental and FEA scaling of $E_{\mathrm{pnc}}(V_{\mathrm{f}})$ where the effective shear modulus of the CNTs is $G \approx 3.1$ GPa.[158] This plot shows that including the evolution of w with V_{f} better represents observed scaling of $E_{\mathrm{pnc}}(V_{\mathrm{f}})$, and that A-CNT infusion with a polymer to form A-PNCs reduces $w(V_{\mathrm{f}})$ by $\approx 25\%$ ($\rightarrow \Lambda \approx 0.75$). (b) Plot comparing the scaling of $E_{\mathrm{pnc}}(V_{\mathrm{f}})$ as a function of the CNT morphology (via Eq. 6.1 and Eqs. 6.2a−6.2f) to a previously reported experimental and FEA scaling of $E_{\mathrm{pnc}}(V_{\mathrm{f}})$ where $G \approx 4.7$ GPa.[50] This plot demonstrates that a $\approx 10\%$ reduction in $w(V_{\mathrm{f}})$ ($\rightarrow \Lambda \approx 0.9$) during A-PNC synthesis can best represent the previously observed scaling of $E_{\mathrm{pnc}}(V_{\mathrm{f}})$.

Figure 6.5).[50,158] In Ref. 158, the FEA results illustrated that the waviness of the CNTs in the A-PNCs appears to decrease significantly as V_{f} is increased, but since the previous simulation could only analyze CNTs with a constant w,[158] the scaling of E_{pnc} with V_{f} could not be accurately reproduced. The ability of the simulation scheme reported here to use representative descriptions of the magnitude and evolution of the stochastic CNT waviness when modeling E_{cnt} can lead to more accurate predictions of the mechanical behavior of A-PNCs (via E_{pnc}) as a function of the CNT morphology (via w) and packing (via V_{f}).

6.4 Conclusions and Recommendations for Future Work

This Chapter presented a modeling framework that allows the integration of the 3D morphology information of A-CNT arrays into mechanical property prediction for A-PNCs. Modeling results indicate that the CNT waviness, quantified *via* w, is responsible for more than three orders of magnitude reduction in the effective CNT axial elastic modulus. Also, by including information on both the uncertainty and V_{f} scaling of the waviness, the simulation is able to replicate the experimentally measured E_{pnc},[50,158] and outperform the mechanical property predictions of previous FEA models that were only capable of analyzing CNTs with a constant w. Additionally, the simulation indicates that the presence of a polymer matrix reduces the waviness of the A-CNTs in the A-PNC by $\approx 10\% - 25\%$ when compared to the waviness of pure A-CNT arrays. Further work to elucidate the origin of the observed waviness reduction is required, and future study of the morphology of A-CNT arrays and A-PNCs *via* three-dimensional quantitative electron microscopy is planned.[157] Also, once additional information on the three-dimensional morphology of A-CNT arrays and A-PNCs is available, the full elastic constitutive relations (beyond the important axial stiffness) of these architectures will be analyzed and simulated. Using this simulation framework, more accurate material property predictions for CNT and other nanofiber based architectures may become possible, potentially enabling the design and fabrication of next-generation multifunctional materials with controlled properties.

In the next Chapter, the modified mechanical analysis presented here, along with the 3D morphology information from Chapter 4, are used to study the mechanical behavior of an A-CMNC.

Chapter 7

Carbon Matrix and Aligned Carbon Nanotube Carbon Matrix Nancomposites

To predict the mechanical behavior of A-CMNCs made using the pyrolysis of A-PNCs, where the matrix properties cannot be assumed to remain constant as a function of processing, the stiffness contribution of A-CNT arrays must be combined with the structure-property relations of a PyC matrix with evolving nanostructure. Although there are a large number of studies from the last several decades that relate the structure of PyCs to their mechanical properties, many of these previous works do not include sufficient information about the structure and morphology of the graphitic cystallites that comprise their PyCs. The incomplete characterization of most previously studied PyCs hinders the development of structure-mechanical property relations that are generalizable to PyCs synthesized using a variety of precursor carbon sources and processing techniques. Through extensive characterization of the graphitic crystallite geometry and bonding character and their effect on the mechanical behavior of the PyCs and resulting A-CMNCs, this Chapter presents the approach used to combine the effective stiffness contribution of the A-CNT array (from Chapter 5) with that of a PyC matrix with evolving mechanical properties to approximate the A-CMNC elastic modulus scaling with V_f. Using these results, the elastic properties of A-CMNCs can be engineered to maximize their performance in lightweight applications, potentially enabling the design and manufacture of aerospace structures with reduced mass, enhanced hardness, and wider temperature operating regimes.

This Chapter presents the modeling approach utilized to predict the effective axial elastic modulus of A-CMNCs using the mechanical behavior of A-CNT arrays quantified in Chapter 5, and PyC matrix contribution quantified *via* the structure-mechanical property relations that are established through their experimentally determined crystallite dimensions (L_a and L_c), and Vickers hardness (H_V). Similar to the analysis performed on A-PNCs in Chapter 6, the modeling approach detailed here utilizes rule of mixtures to couple the contributions of the A-CNTs and PyC matrix, and assumes that the PyC matrix effectively eliminates the torsion deformation mechanism of the CNTs that comprise the A-CMNCs.

7.1 Structure and Mechanical Properties of PyCs and A-CMNCs Derived *via* Polymeric Precursors

As briefly mentioned above, this Chapter develops structure-mechanical property relations of the PyC matrix and presents a mechanics framework that utilizes 3D A-CNT morphology information to model the elastic behavior of A-CMNCs. In this Section, previously reported experimental results for the structure and properties of PyCs is reviewed, and the current state-of-the-art in A-CMNCs made *via* both carbon deposition and polymer-derived ceramics processing is discussed.

Previous studies on the synthesis of A-CMNCs, made *via* the typical synthesis routes of polymer derived ceramics,[219–222] demonstrated that CNT confinement leads to higher hardness, but were not able to analyze the reinforcement mechanism.[26,27] Since the mechanical properties of the PyC matrix of the A-CMNCs likely contribute significantly to the stiffness of the nanocomposites, evaluation of the dependence of the mechanical behavior of the PyCs on processing is the first step towards quantification of the CNT reinforcement mechanism. Since the mechanical properties of PyCs are a function of the nano/microstructure, which strongly depends on the pyrolyzation process including temperature (T_p), the evolution of nanostructure and mechanical behavior of the PyCs as a function of T_p must be understood. The original chemical structure of the polymeric precursor can strongly influence the evolution of the resulting PyC, and based on early work reported in Ref. 223, there are two kinds of PyCs: low density (LD) also known as 'non-graphitizing' PyCs; and high density (HD) also known as 'graphitizing' PyCs. The main difference between LD and HD PyCs is that, although they both form graphitic crystallites characterized by L_a, from the (100) and (110) 3D lattice planes (*i.e. via* the [100] and [110] Miller indices also known as $hk\ell$), and L_c, from the (002) lattice plane (*i.e. via* the [002] $hk\ell$), the graphitic crystallites in HD have a narrower orienta-

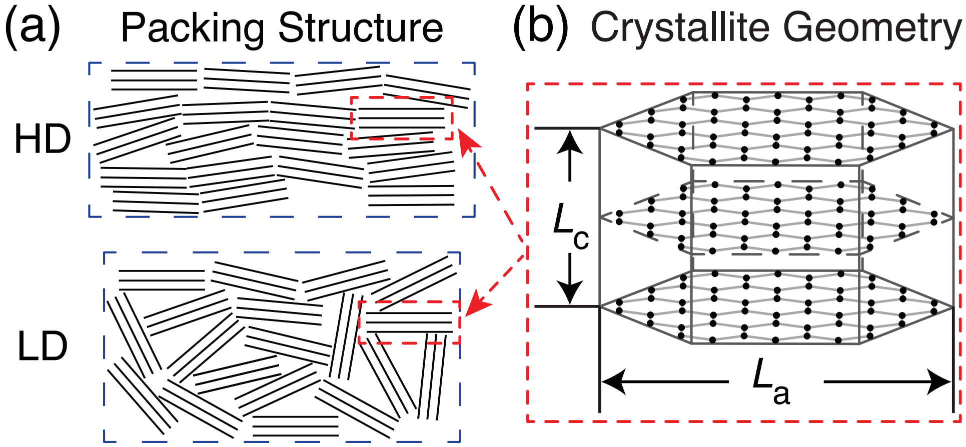

Figure 7.1: Structure and geometry of the graphitic crystallites that comprise PyC. (a) Illustration of exemplary LD and HD packing structures of graphitic crystallites in PyC where a $\sim 15\%$ increase in density from LD to HD is typical. (b) Illustration of L_a and L_c used to approximate the size and geometry of the crystallites that comprise PyCs, and their relationship with the [100] and [001] $hk\ell$ lattice directions that orthogonal to the (100) and (002) lattice planes. Note: for the illustrated 3-layer crystallite, L_c is twice the inter-layer separation.

tion distribution, *i.e.* texture, and exhibit significant L_c growth at $T_\mathrm{p} \lesssim 2000°\mathrm{C}$, *i.e.* the crystallites in HD PyCs have a lower aspect ratio characterized by $L_\mathrm{a}/L_\mathrm{c}$ than the crystallites that comprise LD PyCs.[223] See Figure 7.1 for an illustration of the nanostructure of LD and HD PyCs along with the relevant graphitic crystallite geometries quantified *via* L_a and L_c that originate from the (100) and (002) lattice planes. These differences that distinguish HD PyCs from LD PyCs still hold at $T_\mathrm{p} \gtrsim 3000°\mathrm{C}$,[223] and have a strong impact on how graphitic crystallites of HD and LD PyCs evolve when processed at both high ($T_\mathrm{p} \gtrsim 1500°\mathrm{C}$) and low ($T_\mathrm{p} \lesssim 1500°\mathrm{C}$) temperatures.

There are a number of characterization tools that can be used to study the structural evolution of PyCs as a function of processing. The most common approach is to approximate L_a and L_c for carbon materials through x-ray diffraction (XRD). To calculate the average equivalent L_a and L_c of the graphitic crystallites that comprise the PyCs, the (100) and (002) peaks of the XRD pattern are used in conjunction with the Scherrer equations as follows:[224–226]

$$L_\mathrm{c} = \frac{0.89\lambda_\mathrm{xrd}}{\beta_{002}\cos(\theta_{002})} \tag{7.1a}$$

$$L_\mathrm{a} = \frac{1.84\lambda_\mathrm{xrd}}{\beta_{100}\cos(\theta_{100})} \tag{7.1b}$$

where λ_xrd is the wavelength of the incident x-ray radiation (normally ~ 0.154 nm corresponding to a Cu source), β_{002} and β_{100} are the full width at half maximum of the (002) and (100) peaks, and θ_{002} and θ_{100} are the positions of the (002) and (100) peaks. The peak position and full width at half maximum of the (110), θ_{110} and β_{110}, can also be used in Eq. 7.1a (*i.e.* instead of θ_{100} and β_{100}, respectively) to yield an independent and supplemental approximation of L_a, but the (110) peak may not appear in the XRD pattern until the PyC has gone through graphitization at very high temperature ($T_\mathrm{p} > 3000^\circ$C),[227] and may therefore be unavailable for PyCs synthesized at low T_p. Another geometry parameter for the structure of the graphitic crystallites is the (002) inter-layer separation (d_{002}) that is determined using the Bragg's law as follows:

$$n_\mathrm{xrd}\lambda_\mathrm{xrd} = 2d_{002}\sin\left(\theta_{002}\right) \tag{7.2}$$

where n_xrd is an integer that corresponds to the number of (002) layers the incident radiation traveled before being reflected ($\rightarrow n_\mathrm{xrd} = 1$ is normally assumed since that corresponds to highest reflection probability). Using XRD, the general geometry of the graphitic crystallites can be approximated, but another technique needs to be used to discern the bonding character of the graphitic crystallites of the PyCs: Raman spectroscopy.

Raman spectroscopy is a widely used non-destructive technique for studying defects and disorder in carbon materials.[62,228–230] The two characteristic peaks used to analyze carbon materials are the D-band normally found at $\sim 1335 - 1350$ cm^{-1} which is representative of defects/disorder in the (002) plane, and the G-band found at $\sim 1580 - 1600$ cm^{-1} which corresponds to the in-plane sp^2 bond stretching.[62,228–232] A common way to analyze Raman spectra and discern whether one material/sample is more or less graphitic than another is to evaluate the intensity ($I_\mathrm{D}/I_\mathrm{G}$) and/or area ($A_\mathrm{D}/A_\mathrm{G}$) ratios of the D- and G-bands of the Raman spectrum.[228,229,233,234] These quantities, *i.e.* $I_\mathrm{D}/I_\mathrm{G}$ and $A_\mathrm{D}/A_\mathrm{G}$, can also be utilized to approximate L_a using the following previously proposed scaling relations:[228,233,234]

$$L_\mathrm{a} = 4.4\left(\frac{I_\mathrm{D}}{I_\mathrm{G}}\right)^{-1} \tag{7.3a}$$

$$L_\mathrm{a} = 2.4\times10^{-10}\lambda_\mathrm{raman}^4\left(\frac{A_\mathrm{D}}{A_\mathrm{G}}\right)^{-1} \tag{7.3b}$$

$$L_\mathrm{a} = \sqrt{\frac{1}{0.55}\left(\frac{I_\mathrm{D}}{I_\mathrm{G}}\right)} \tag{7.3c}$$

where λ_raman is the laser excitation wavelength used during Raman spectroscopy (normally $\sim 500 - 800$ nm for most studies). Eqs. 7.3a– 7.3c are only approximate, and can be further classified into two types by utilizing the previously proposed three-stage model of the transformation of graphite into diamond-like tetrahedral amorphous carbon (see Figure 7.2 for an illustration of the model).[228,229] The three stages of the previously reported model consist of the following transformations:[228,229] (1) graphite → nanocrystalline (NC) graphite; (2) NC graphite → amorphous carbon (a-C); (3) a-C → tetrahedral amorphous carbon (ta-C). For the bulk of graphitic materials, including polymer derived PyCs, the two most applicable stages are stages 1 and 2,[229,235] and each stage has a correlation of I_D/I_G and/or A_D/A_G (they are sometimes used interchangeably in the literature) to estimate L_a from Raman spectroscopy. For stage 1, which is the most heavily studied, the most widely accepted correlation is $L_a \propto A_D/A_G$, *i.e.* Eq. 7.3a and Eq. 7.3b.[228,229,233,234,236]

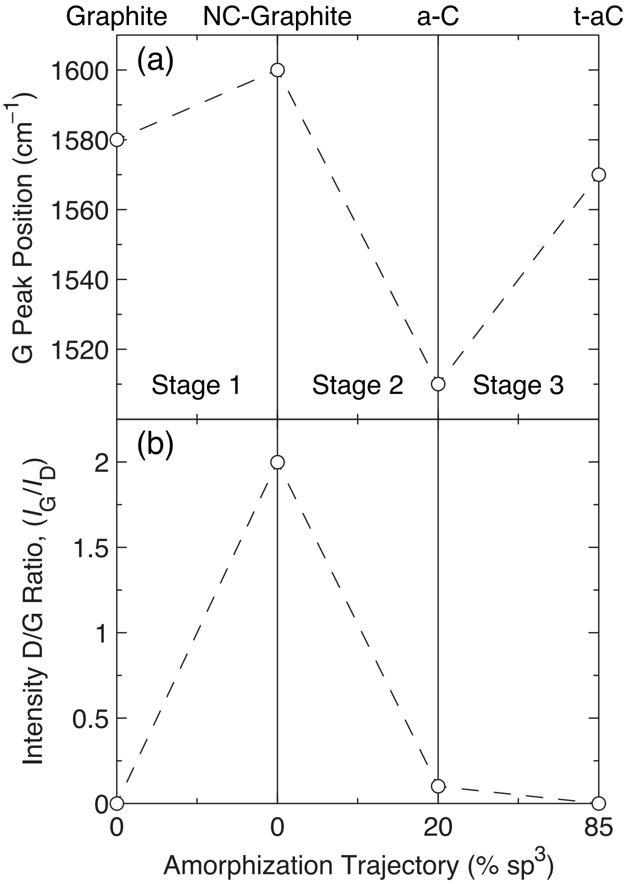

Figure 7.2: Illustration of the previously proposed mechanism of graphite transformation into defective diamond consisting of three stages:[228,229] (1) graphite → nanocrystalline (NC) graphite; (2) NC graphite → amorphous carbon (a-C); (3) a-C → tetrahedral amorphous carbon (ta-C). (a) Position of the G band as a function of amorphization stage (sp^3) character demonstrating that the maximum G peak position occurs between stages 1 and 2. (b) Inverse of the ratio of the intensities of the G and D bands (I_G/I_D) illustrating that the minimum value of I_G/I_D occurs between stages 1 and 2. Reproduced from Ferrari and Robertson.[228]

However, for small values of L_a, corresponding to a large number of defects, the linear relationship proposed for stage 1 will eventually fail,[228,229,235] and previous studies proposed the use of $L_a \propto \sqrt{A_D/A_G}$ for $L_a \lesssim 3$ nm.[225,228,229] As shown by Figure 7.2, the I_D/I_G (and A_D/A_G) hits a maximum at the intersection of stage 1 and stage 2, and decreases on either side of the maximum, the analysis of an additional parameter is needed to determine whether the PyCs are in stage 1 or 2: the half width half maximum of the D- and G-bands (γ_D and γ_G, respectively). Recent work indicates that γ_D and γ_G will decrease as the PyCs becomes more graphitic and the typical defect separation within the (002) plane of the graphitic crystallites (L_D) decreases.[235,237] This decrease in γ_D and γ_G corresponds to the PyC approaching stage 1 (more order, larger L_D) from stage 2 (less order, smaller L_D), where I_D/I_G and A_D/A_G increase towards their maximum that occurs at the onset of stage 1.[228,235,237] By combining the evolution of I_D/I_G and A_D/A_G with the scaling of γ_D and γ_G as a function of T_p, a wide variety of information can be extracted about the defects present in the graphitic crystallites that comprise the PyCs, but Raman spectroscopy is not suitable to determine the functional groups present in the PyCs. Given the PyC transformation, functional groups can provide additional insight into the process.

One of the most widely utilized techniques to analyze the functional groups present in carbon materials is x-ray photoelectron spectroscopy (XPS). However, although XPS is very adept at analyzing the functional groups present on the surface of carbon materials,[238] *e.g.* carbon fibers,[239] XPS is not sufficiently sensitive to minor structural features and cannot analyze the chemical structure on the bulk level.[239,240] XPS measurements are also very time consuming.[240] To overcome these challenges of XPS, another versatile and powerful analysis method for evaluating the chemical structure of carbon materials can be used: Fourier transform infrared (FTIR) spectroscopy.[238] FTIR can only provide qualitative information about the chemistry of carbon materials, and cannot determine the chemical composition of the sample surface. FTIR can, on the other hand, detect very small chemical changes that arise due to pyrolysis, making FTIR potentially useful for discerning the evolution of functional groups present in throughout the entire volume, as opposed to just the surface, of the PyCs as a function of T_p, and subsequently the development of the PyC structure-mechanical property relations.

Since high-temperature processing enables the migration of defects in the graphitic crystallites that comprise the PyCs,[177] evaluation of the mechanical behavior of the PyCs as a function of processing (here we choose T_p) is of interest. Because the PyCs studied here were previously shown to have $> 60\%$ porosity,[26–28] the mechanical properties reported in this Chapter were estimated using a microscale indentation technique known as the Vickers microhardness test, which enables the quantification of the Vickers hardness (H_V) of the material. Recent studies of the mechanical behavior of defective graphene indicates that the presence of lattice vacancies leads to reduced stiffness,[110,190,243] and that processing that evolves the microstructure of the PyCs from stage 2 to stage 1, such as higher T_p, will lead to significantly higher elastic moduli and strengths.[110] However, previous works on LD and HD PyCs processed at T_p up to 2000°C showed that the mechanical properties of the PyC can either be enhanced or diminished depending on the T_p.[241,242,244] Based on the data presented in these previous works, this non-monotonic scaling of the mechanical properties of studied PyCs as a function of T_p might originate from changes in L_a and L_c, but the large spread and lack of obvious trend in the reported data likely prevented the development of a unified scaling relation that relates the crystallite structure and morphology to the observed H_V results. See Figure 7.3 for the previously reported H_V results for LD and HD PyCs as a function of L_a and L_c. Additionally, conflicting simulation results reported in the literature for size effects in graphene flakes have not helped provide a robust explanation for the observed experimental H_V for PyCs.[245–247] This confusion originates from both the incomplete characterization

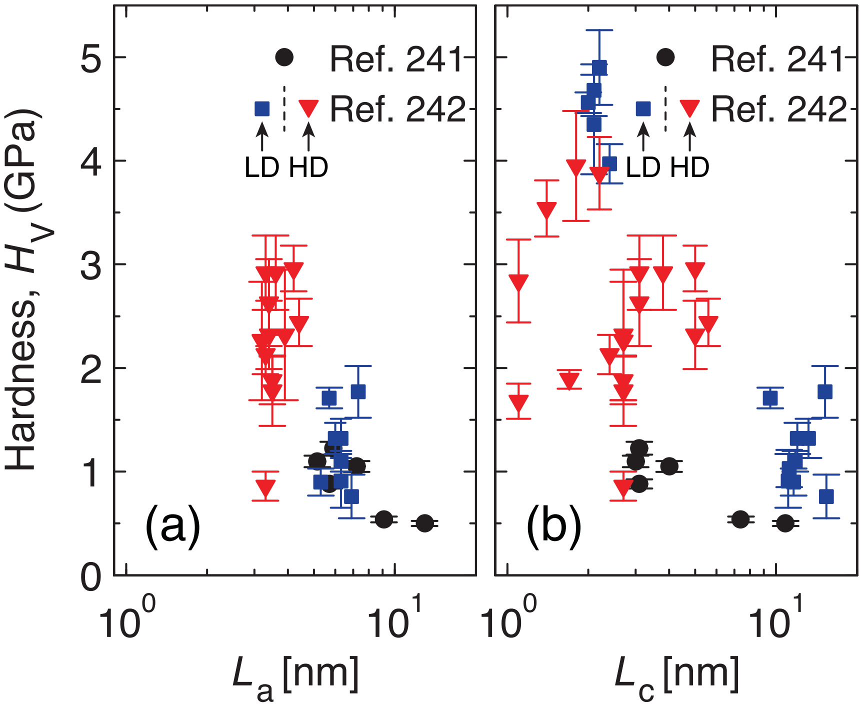

Figure 7.3: Previously reported scaling of H_V for LD (●, and ■) and HD (▼) PyCs as a function of L_a, (a), and L_c, (b), showing the wide spread and a lack of a robust trend.[241,242]

of the morphology and structure of the graphitic crystallites that comprise the PyCs and the lack of understanding of the physical mechanism that dominates the PyC mechanical behavior, since the stiffness constants that govern the elastic response of layered carbon materials can vary by orders of magnitude depending on the structure and morphology (especially inter-layer bonding character) of the graphitic crystallites.[116] In this Chapter, morphological, structural, and chemical information collected during the PyC experimental characterization is used to develop a scaling relation that couples L_{a}, L_{c}, and d_{002} to the H_{V} evolution as a function of T_{p} observed here and in Ref. 241 and Ref. 242.

Recent studies on have demonstrated that A-CMNCs can be manufactured using either carbon vapor infiltration,[248–251] or through vapor/liquid phase polymer infiltration pyrolysis (*i.e.* polymer-derived carbon).[252–257] The presence of A-CNTs was recently found to assist with the graphitic crystallite formation in PyCs,[257,258] which was attributed to interphase formation,[259] and as V_{f} was increased, *i.e.* higher degree of CNT confinement, L_{a} in the graphitic crystallites was found to increase.[254,255,257] Additionally, thermal treatment with $T_{\mathrm{p}} > 2000°\mathrm{C}$ showed that significant graphitization of the PyC matrix is possible,[256,257,259,260] *i.e.* the mixture of hexagonal, rhombohedral, and turbostratic/amorphous carbon phases were ‘healed’ to form predominantly hexagonal graphite.[259] Mechanical property characterization indicated that A-CMNCs can outperform the current state-of-the-art high temperature carbon-based engineering material,[256,257] carbon fiber reinforced carbon (C/C), and that as T_{p} is increased (*i.e.* graphitization occurred), the mechanical properties of the A-CMNCs were degraded.[256,257,259] However, the E_{eff} results for A-CMNCs reported in Ref. 256 and Ref. 257 were quantified *via* uniaxial tensile testing, where strains to failure of $\lesssim 1\%$ were observed (*i.e.* brittle failure).[256,257] While E_{eff} for superhard brittle materials, *e.g.* diamond and cubic boron nitride (c−BN), was successfully approximated *via* tension in previously reported simulations,[261–266] experimental characterization of E_{eff} *via* tensile testing may not yield representative results since such brittle materials, especially c−BN,[265] have a high propensity to cleave along preferred crystallographic directions,[262–266] and/or may have tensile deformation mode that involve individual bond-breaking events that lead to significantly diminished strength under tension like in cubic boron carbon nitride ($\mathrm{BC_2N}$).[266] This means that while the E_{eff} results presented in Ref. 256 and Ref. 257 might be representative, E_{eff} estimated using compression techniques, *e.g.* especially indentation,[267] will be more reliable.[262–269] Additionally, Ref. 267 showed that a conversion factor of $\sim 10\times$ can be used to approximate the (compression) E_{eff} of superhard materials from their indentation hardness.[267] See Figure 7.4 for the previously reported

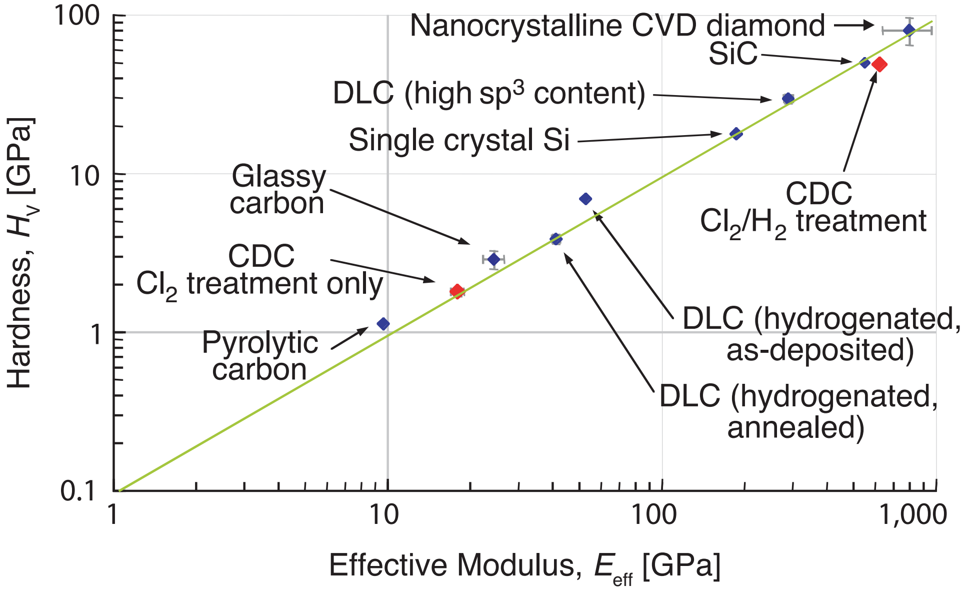

Figure 7.4: Previously reported scaling of hardness (H_{V}), estimated *via* nanoindentation, to the effective modulus (E_{eff}) of a variety of carbon and silicon based materials as presented Gogotsi et al.[267]

scaling of the hardness, estimated *via* nanoindentation, to the E_{eff} of a variety of PyC, glassy carbon, silicon carbide (SiC), carbide-derived carbon (CDC), diamond-like carbon (DLC), nanocrystalline diamond, single crystal silicon (Si) as presented by Gogotsi et al.[267] Using this conversion factor, the hardness results of PyCs and A-CMNCs, estimated *via* Vickers microhardness ($\rightarrow H_{\mathrm{V}}$), can be directly compared to other superhard materials and their composites, and the physics underlying the reinforcement of the PyCs with A-CNTs in the A-CMNCs can be explored.

This Section reviewed the previously reported experimental results for the structure and mechanical property characterization of PyCs, and the current state-of-the-art in A-CMNCs made *via* both carbon deposition and polymer-derived ceramics was discussed. In the remainder of this Chapter, characterization and analysis utilized to establish the structure-property relations of PyCs is presented, and the experimentally and theoretically evaluated scaling of E_{cmnc} (axial effective modulus of the A-CMNC) as a function of CNT packing proximity is discussed.

7.2 Synthesis and Processing Techniques

A-CNT arrays were grown *via* a previously described thermal catalytic chemical vapor deposition (CVD) process using ethylene as the carbon source.[19–22] The CNTs were grown on 1 cm × 1 cm Si substrates forming A-CNT arrays that are $\sim$ 1 mm tall, and are composed of multiwalled CNTs that have an average outer diameter of $\sim$ 8 nm ($3-7$ walls with an inner diameter of $\sim$ 5 nm and intrinsic CNT density $\rho_{\text{cnt}} \sim 1.7$ g/cm^3),[28,44] $\Gamma \sim 80$ nm,[43] and $V_f \sim 1\%$ CNTs.[44] A post-growth H_2 anneal[48] is used to weaken the attachment of the CNTs to the catalyst layer, which enables the easy delamination of the A-CNT forest from the Si substrate using a standard lab razor blade, thereby allowing further CNT processing to be performed in their free-standing state.

Fabrication of A-PNC precursors *via* vacuum assisted wetting was performed by first gently depositing free-standing CNT forests into hollow cylindrical plastic molds, ensuring that the primary axis of the CNTs in the forest was orthogonal to the plane of the mold. The A-CNT forest was then infused with a de-gassed phenolic resin (Durite SC-1008, Momentive Specialty Chemicals, Inc.) at 40°C under vacuum for $\sim$ 24 hr, forming the A-PNC precursors.[26–28] No attempt to remove adsorbed water[46] was made. The polymer precursors were then cured for 6 hr at 80°C at atmospheric pressure.[26–28] Re-infusion of A-CMNCs with polymer resin (for *in situ* pyrolysis only) was done by immersing the A-CMNCs that were pyrolyzed once in a diluted phenolic resin (with 40% by mass acetone) for $\sim$ 72 hr in acetone, and then curing for 30 min at 80°C at atmospheric pressure.[27] Pure phenolic resin samples were prepared by first pouring the de-gassed resin into a square rubber mold, and then curing at 80°C for 6 hr at atmospheric.

The samples were then heat treated to transform the phenolic resin into PyC, and to potentially form new wall defects in the CNTs, while enabling the native CNT wall defects to migrate and annihilate.[177] The CNTs, phenolic resin, and A-PNCs were pyrolyzed both *in situ* and *ex situ*: *in situ* pyrolysis was performed using a high temperature x-ray diffraction holder at atmospheric pressure in an He environment; and *ex situ* pyrolysis was performed using a commercial hot wall tube furnace (STT-1600, from SentroTech Corp.) with a 89 mm (3.5 in) inner diameter SiC tube in an Ar environment. *In situ* pyrolysis was performed at a ramp rate of 10°C/min at the following T_p and hold times (t_{hold}) of $t_{\text{hold}} = 2$ hr for PyCs and A-CNTs, and $t_{\text{hold}} = 2$ hr for A-CMNCs: 600°C (PyCs, A-CMNCs, and A-CNTs), 800°C (PyCs and A-CNTs), 1000°C (PyCs, A-CMNCs, and A-CNTs), and 1500°C (A-CNTs only). Three samples were pyrolyzed at each T_p. *Ex situ* pyrolysis was performed at a ramp rate of 4°C/min (furnace maximum) at the following T_p and $t_{\text{hold}} = 30$ min for both PyCs and A-CMNCs: 600°C, 800°C, 1000°C, 1200°C, and 1400°C. Five samples were pyrolyzed at each T_p.

7.3 Structure-Mechanical Property Characterization and Modeling

In this Section, characterization to evaluate the graphitic crystallite geometry and morphology (Section 7.3.1.1), bonding character (Section 7.3.1.2), and chemical structure (Section 7.3.1.3) are detailed, and the mechanical behavior characterization (Section 7.3.2.1) and modeling (Section 7.3.2.2 and Section 7.3.2.3) approaches are discussed.

7.3.1 Structure and Morphology Characterization

Here, the XRD, Raman spectroscopy, and FTIR spectroscopy experimental methods are presented.

7.3.1.1 XRD Analysis

XRD was used to analyze the structural evolution of the A-CNTs, phenolic resin, and A-PNCs during the heat treatments as outlined in Section 7.2. XRD analysis during the *in situ* pyrolysis approach was done *via* the *in situ* high temperature holder of a Rigaku SmartLab x-ray diffractometer operating with Cu Kα radiation. The operating parameters for the *in situ* pyrolysis approach were 45 kV and 200 mA, and the step scanning interval was 0.02° ($2\theta_\mathrm{xrd}$). PANalytical X'Pert Pro was used to analyze samples processed using *ex situ* pyrolysis. For the *ex situ* pyrolysis approach, Cu K_α radiation was passed through a 2° anti-scattering slit with a 0.04 rad Soller slit in X'celerator mode. The XRD experiment for the *ex situ* pyrolysis approach was performed at 45 kV and 40 mA with a scanning step interval of 0.02° ($2\theta_\mathrm{xrd}$). $\mathrm{LaB_6}$ was used as the standard material for all measurements.

7.3.1.2 Raman Spectroscopy Analysis

For both the *in situ* and *ex situ* pyrolysis approaches, Raman spectra were collected using a LabRam HR800 Raman microscope (Horiba Jobin Yvon) with 532 nm (2.33 eV) laser excitation through a 10× objective (N.A. 0.25). Several spots on each PyC and A-CMNC sample were studied to ensure that representative data was used when calculating the $I_\mathrm{D}/I_\mathrm{G}$ and $A_\mathrm{D}/A_\mathrm{G}$. To facilitate the analysis of the defect information provided by Raman spectroscopy, the Raman spectra were fit using two Lorentzian distributions corresponding to the graphitic D-band (centered at $\omega_\mathrm{D} \sim 1350$ cm^{-1}), a-C

G-band (centered at $\omega_{\mathrm{G,a-C}} \sim 1500$ cm^{-1}), and the Breit-Wigner-Fano distribution that corresponds to the graphitic G-band (centered at $\omega_{\mathrm{G}} \sim 1590$ cm^{-1}).[228,270,271] Background corrected Raman spectra, characterized by the Raman shift (ω) and intensity ($I(\omega)$), were fit using the following expression:

$$I(\omega) = I_{\mathrm{D}}\left(\frac{\gamma_{\mathrm{D}}^2}{(\omega-\omega_{\mathrm{D}})^2+\gamma_{\mathrm{D}}^2}\right) + I_{\mathrm{G,a-C}}\left(\frac{\gamma_{\mathrm{G,a-C}}^2}{(\omega-1500)^2+\gamma_{\mathrm{G,a-C}}^2}\right) + I_{\mathrm{G}}\left(\frac{\left(1+\frac{\omega-\omega_{\mathrm{G}}}{q\gamma_{\mathrm{G}}}\right)^2}{1+\left(\frac{\omega-\omega_{\mathrm{G}}}{\gamma_{\mathrm{G}}}\right)^2}\right) \tag{7.4}$$

where I_{D} and $I_{\mathrm{G,a-C}}$ are the Raman intensities of the Lorentzian distributions that fit the graphitic D-band and a-C G-band, respectively, and I_{G} and q are the Raman intensity and coupling coefficient of the Breit-Wigner-Fano (BWF) band that fits the graphitic G-band.[228,270,271] The fitting expression detailed in Eq. 7.4 yielded very good agreement ($\mathbb{R}^2 > 0.99$) with the experimental Raman spectra of PyCs and A-CMNCs at 1000 cm^{-1} $\leq \omega \leq$ 1800 cm^{-1}, and $I_{\mathrm{D}}/I_{\mathrm{G}}$ was evaluated simply using the I_{D} and I_{G} from the Lorentzian and BWF fits of the D- and G-bands, while $A_{\mathrm{D}}/A_{\mathrm{G}}$ was evaluated using the areas of the Lorentzian and BWF fits of the D- and G-bands (A_{D} and A_{G}, respectively). A_{D} and A_{G} were evaluated as follows:

$$A_{\mathrm{D}} = \int_{\omega_{\mathrm{D}}-\omega_{\mathrm{int}}}^{\omega_{\mathrm{D}}+\omega_{\mathrm{int}}} I_{\mathrm{D}}\left(\frac{\gamma_{\mathrm{D}}^2}{(\omega-\omega_{\mathrm{D}})^2+\gamma_{\mathrm{D}}^2}\right)\mathrm{d}\omega \tag{7.5a}$$

$$A_{\mathrm{G}} = \int_{\omega_{\mathrm{G}}-\omega_{\mathrm{int}}}^{\omega_{\mathrm{G}}+\omega_{\mathrm{int}}} I_{\mathrm{G}}\left(\frac{\left(1+\frac{\omega-\omega_{\mathrm{G}}}{q\gamma_{\mathrm{G}}}\right)^2}{1+\left(\frac{\omega-\omega_{\mathrm{G}}}{\gamma_{\mathrm{G}}}\right)^2}\right)\mathrm{d}\omega \tag{7.5b}$$

where $\omega_{\mathrm{int}} = 125$ cm^{-1} and corresponds to half the width of the Raman shift integration regime centered around ω_{D} and ω_{G}. The approximate values of $I_{\mathrm{D}}/I_{\mathrm{G}}$, $A_{\mathrm{D}}/A_{\mathrm{G}}$, γ_{D}, and γ_{G} are presented in Section 7.4.1.2.

7.3.1.3 FTIR Analysis

FTIR was performed for both the *in situ* and *ex situ* pyrolysis approaches using a FTIR6700 Fourier Transform Infrared Spectrometer (Thermo Fisher Scientific, Inc.), and the chemical structure was analyzed using the OMNIC software (Thermo Fisher Scientific, Inc.). The attenuated total reflection mode technique was used to study the chemistry of a cured phenolic resin baseline, and the KBr pellet method was employed in transmission mode to study the A-CNTs, PyCs, and A-CMNCs. All

FTIR signal was transformed to absorbance mode during the analysis. An average of 32 scans with a resolution of 8 cm^{-1} were taken for each sample, and 3 samples were tested at each T_p.

7.3.1.4 Theoretical Framework for Matrix Density Scaling with Crystallite Geometry

Since knowing the evolution of the PyC matrix density (ρ_pyc) as a function of the crystallite geometry is useful for robust development of the PyC structure-property relations, a geometric model was developed to estimate the impact of of L_a and L_c on ρ_pyc. This was achieved by defining a unit cell that encompasses two graphitic crystallites, their orientation angle (θ_oa), and the subtended ultramicropores that form due to crystallite orientation, or lack thereof (see Figure 7.5a for an illustration of the unit cell as a function of θ_oa, illustrating an exemplary 'open structure' that is characteristic of LD PyCs). This defines a simple geometric relation for ρ_pyc:

$$\rho_\mathrm{pyc} = \rho_\mathrm{g}\left(\frac{1}{1+0.5\left(\frac{L_a}{L_c}\right)\sin(\theta_\mathrm{oa})\cos(\theta_\mathrm{oa})}\right) \tag{7.6}$$

where ρ_g is the density of single crystal graphite ($\rightarrow \rho_\mathrm{g} \sim 2.25$ g/cm^3), and $0^\circ \leq \theta_\mathrm{oa} \leq 45^\circ$. $\theta_\mathrm{oa} = 0^\circ$ physically represents an ideal graphene/graphite structure, where the crystallites are perfectly aligned, while $\theta_\mathrm{oa} = 45^\circ$ represents an isotropic LD PyC (*i.e.* 'open') structure, where the crystallites are completely randomly oriented. See Figure 7.5 for the scaling of ρ_pyc as a function of θ_oa for a variety of L_a/L_c. Analysis of the predictions Eq. 7.6 when compared to experimental ρ_pyc values is presented in Section 7.4.1.4. While the different crystallite orientation defined by θ_oa may

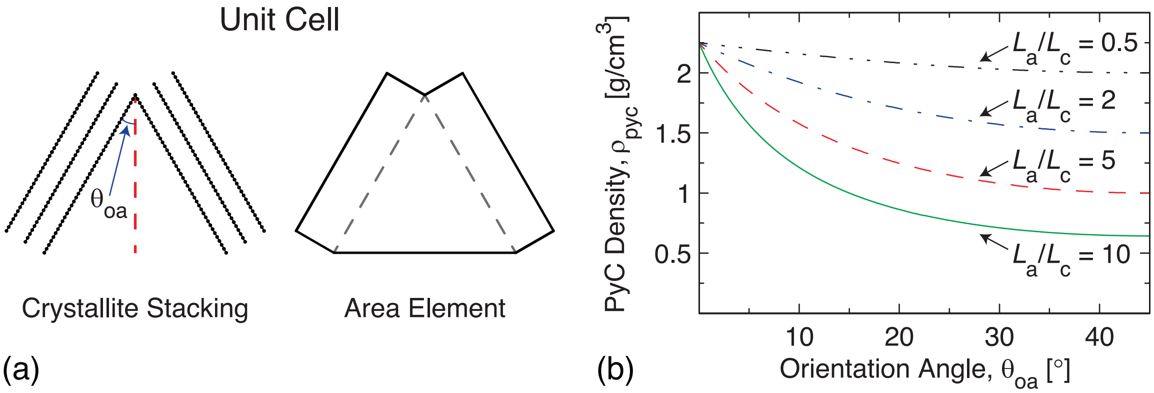

Figure 7.5: Theoretical framework and model predictions for the PyC matrix density (ρ_pyc). (a) Illustration of the crystallite stacking and unit cell representing the structure of an LD PyC exhibiting an 'open structure'. (b) Plot of ρ_pyc as a function the crystallite orientation angle (θ_oa) for a variety of crystallite geometries (L_a/L_c).

not be the most energetically favored states found in close packed PyCs, a mixture of many cyrstallite orientations can more realistically model a disordered PyC that is far from the ideal structure expected for single crystal graphite.

7.3.2 Hardness Scaling

Here, the experimental Vickers microhardness technique is outlined (see Section 7.3.2.1), and the PyC (see Section 7.3.2.2) and A-CMNC (see Section 7.3.2.3) mechanical behavior modeling approaches are discussed.

7.3.2.1 Experimental Vickers Microhardness Evaluation

Vickers microhardness testing was done for samples synthesized *via* both the *in situ* and *ex situ* pyrolysis approaches using a LECO LM Series Microhardness Tester (LECO Corp.) by placing each mounted sample under a 50× objective magnification lens. Indentation was performed *via* a standard pyramidal diamond tip by applying 1.0 kgf ($\sim$ 9.8 N) at each spot for 15 s, and H_V was approximated at each T_p by indenting (indentation depth $\sim$ 10 μm) 5 samples at least 10 times ($\rightarrow >$ 50 measurements per T_p). H_V as a function of T_p, along with the corresponding density of (dried) PyCs and A-CMNCs can be found in Table 7.3.

7.3.2.2 Theoretical Framework for Hardness Scaling with Crystallite Size and Thickness

To model the mechanical behavior of PyCs, the relevant deformation modes that would be activated during indentation must first be discussed. As analyzed in detailed in a previous study,[116] graphitic carbons have very anisotropic elastic constants for in-plane extension (C_{11}), out-of-plane extension (C_{33}), and inter-layer shear (C_{44}). See Table 7.1 for a summary of the reported experimental and theoretical values of C_{11}, C_{33}, and C_{44}, and Figure 7.6 for their illustration. As Table 7.1 demonstrates, $C_{11} \gg C_{33} \gg C_{44}$, especially for turbostratic carbons where $C_{11} > 3000 \times C_{44}$ and

Table 7.1: Experimental and theoretical values of in-plane (C_{11}), out-of-plane (C_{33}), and inter-layer shear (C_{44}) elastic constants for graphene/graphite as reported by Savini et al.[116]

Graphite Type	Approach	C_{11} [GPa]	C_{33} [GPa]	C_{44} [GPa]
Hexagonal (ABA)	Experimental	1109 ± 16	39 ± 7	5.0 ± 3.0
	Theoretical	1109	$29 - 42$	$4.5 - 4.8$
Turbostratic	Experimental	1060 ± 20	37 ± 1	$0.18 - 0.35$
	Theoretical	1080 ± 3	$25 - 37$	$0.16 - 0.34$

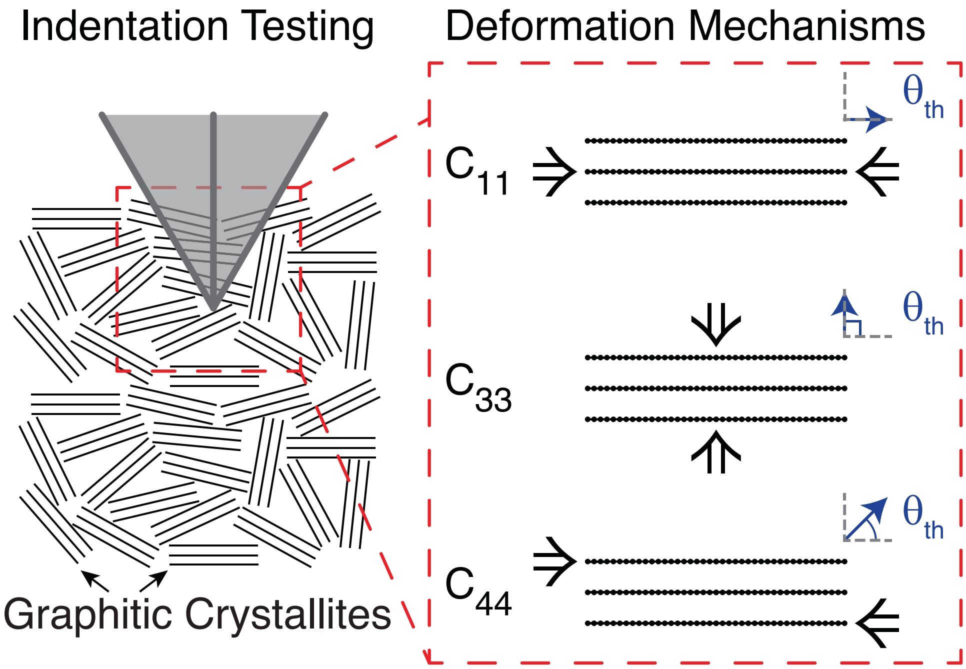

Figure 7.6: Illustration of the indentation technique utilized to experimentally quantify the mechanical behavior of the PyCs and A-CMNCs, *i.e.* *via* hardness (H_V). The inset presented illustrations of the deformation mechanisms that govern the measured H_V, and the model orientation angle (θ_{th}) where they are most relevant.

$C_{33} > 100 \times C_{44}$. This indicates that the inter-layer shear deformation mode governed by C_{44} will dominate the mechanical behavior of the graphitic crystallites ($>$ 90% effective compliance contribution) that comprise the PyC matrix, while the deformation modes governed by C_{11} and C_{33} will contribute $<$ 10% of the effective compliance of the PyCs, especially when the crystallite orientation angle $\theta_{th} \sim 45°$ (*i.e.* isotropic crystallite orientation). Additionally, Table 7.1 illustrates that C_{44} is strongly dependent on the crystallite morphology, since bernal stacked (ABAB) graphite has a 10× larger C_{44} than turbostratic graphite. This means that knowledge of d_{002} is essential, since $d_{002} \approx 0.34$ nm is normally ascribed to ABAB graphite ($C_{44} \sim 4.5$ GPa), while $d_{002} > 0.35$ nm is usually classified as turbostratic graphite/carbon ($C_{44} \sim 0.35$ GPa). Also, since it was recently shown that the presence of inter-layer bonds can increase the pulling force needed for inter-layer shear ($\propto C_{44}$) by $> 3\times$ in graphene and CNTs,[113] meaning that the crystallite area ($\propto L_a^2$), which correlates the number of inter-layer bonds in a graphitic crystallite to the defect density, should also scale the effective hardness measured *via* indentation. Finally, since the inter-layer shear strain is a function of L_c, L_c^2 (by dimensional analysis) should also scale the effective hardness measured *via* indentation. The following general and reduced forms of the scaling of the theoretical indentation hardness ($H_{\mathrm{V,th}}$) as a function of L_a, L_c, C_{11}, C_{33}, C_{44}, and θ_{th} are proposed:

$$H_{\mathrm{V,th}} \propto \left(\frac{\cos(\theta_{\mathrm{th}})}{C_{11}} + \frac{\sin(\theta_{\mathrm{th}})}{C_{33}} + \frac{\sin(2\theta_{\mathrm{th}})}{C_{44}} \left(\frac{L_c}{L_a}\right)^2 \right)^{-1} \tag{7.7a}$$

$$\hookrightarrow H_{\mathrm{V,th}} \propto C_{44} \left(\frac{L_a}{L_c}\right)^2 \tag{7.7b}$$

where the approximation of Eq. 7.7a made in Eq. 7.7b is reasonable for $10^\circ \leq \theta_{\mathrm{th}} \leq 80^\circ$, and fails at $10^\circ > \theta_{\mathrm{th}}$, where the C_{11} in-plane deformation dominates, and at $80^\circ < \theta_{\mathrm{th}}$, where the C_{33} out-of-plane deformation dominates. Analysis of the $H_{\mathrm{V,th}}$ predictions from Eq. 7.7b are discussed and compared to experimental H_{V} values in Section 7.4.2.1.

7.3.2.3 Effective Axial A-CMNC Modulus *via* 3D A-CNT Morphology

As discussed in Chapter 6, the waviness of the A-CNT arrays as a function of V_{f} that was previously evaluated from SEM images of the cross-sectional morphology of A-CNT arrays using a simple sinusoidal amplitude-wavelength ($\rightarrow a/\lambda$) definition of w could be reduced due to polymer infusion.[42,191] The previously proposed relationship to re-scale $w(V_{\mathrm{f}})$ in A-PNCs where the waviness is reduced as in that polymer infusion is as follows (from Chapter 6):

$$w(V_{\mathrm{f}}) = \Lambda(-0.04967(V_{\mathrm{f}})^{0.3646} + 0.2489 \pm (-0.0852(V_{\mathrm{f}})^{0.2037} + 0.2100)/\sqrt{n}). \tag{7.8}$$

where Λ is a scaling factor that physically represents the impact of polymer infusion, and subsequent curing, on the morphology evolution of the CNTs that comprise the A-CMNCs.[42,191] Since A-CMNCs are made *via* the pyrolysis of A-PNC precursors, the previously evaluated $\Lambda \approx 0.76 \pm 0.04$ for A-PNCs,[191] which represents a $\approx 24 \pm 4\%$ reduction in the waviness of the original A-CNT arrays, is used throughout this Chapter to model the mechanical behavior of A-CMNCs as a function of V_{f}. Note that this is an approximation as the polymers are not the same, but no information is available to draw a distinction between polymer types.

The stiffness of the wavy A-CNTs that comprise the A-CMNCs is analyzed using the principle of virtual work similar to the analysis presented in Chapter 6 for the elastic behavior of the wavy A-CNT that comprise the A-PNCs.[40,42] Since the PyC matrix will restrict the movement of the CNTs during deformation, similar to the polymer matrix in A-PNCs studied in Chapter 6, the analysis used here assumes that deformation *via* torsion is minimal and consists of three primary deformation mechanisms: extension, shear, and bending. The compliance contributions of $\xi_{\mathrm{extension}}$, ξ_{shear}, and

ξ_{bending} can be used with V_f to evaluate $K(w)$, $E_{\text{cnt}}(w)$, as discussed in Chapter 6. Using rule of mixtures, $E_{\text{cmnc}}(V_f)$ can be evaluated as follows:

$$E_{\text{cmnc}}(V_f) = E_{\text{cnt}}(w(V_f))V_f + E_{\text{cm}}(1 - V_f) \tag{7.9}$$

where L_{3D} is the arc length of the two nodes in the z direction ($\rightarrow L_{3D} = \tau(w)\Delta z$ where $\tau(w)$ is the average CNT tortuosity defined by w using a sinusoidal waviness scheme),[40] E_{cm} is the elastic isotropic modulus of the carbon matrix that is converted from the experimentally determined H_V using a conversion factor of $\sim 10 \pm 2\times$,[267] Y and G are the intrinsic moduli of the CNTs, A is the cross-sectional area of the CNTs (hollow cylinder geometry), I is the area moment of inertia of a hollow cylinder exhibiting D_i and D_o of the CNTs, and α is the shear coefficient.[118] Similar to Chapters 5 and 6, A and I are evaluated using $D_i \sim 5$ nm and $D_o \sim 8$ nm,[28,45] which are representative of the CNTs studied here. The analysis carried out here assumes that the Y of the CNTs is constant, and has a value of ~ 1 TPa,[12,30] while G is governed by the elastic properties of the polymeric matrix, where $G \approx 1$ GPa when $G > E_{\text{cm}}$, and $G \approx E_{\text{cm}}$ when $G \leq E_{\text{cm}}$. Additionally, since H_V evolves as a function of V_f, the V_f evolution of E_{cm} is included in Eq. 7.9. Also, like in Chapter 6, perfect load transfer between the CNTs and PyC matrix is also assumed here, and this approximation is further analyzed in Section 7.4.1. Additionally, like in Chapters 5 and 6, the CNT-CNT interactions are not included explicitly in the current analysis, but are instead integrated into the randomness of the CNTs in the arrays which implicitly accounts for fluctuations in their electrostatic interactions.[40] As discussed previously, this leads to simulated A-CNT arrays with a more uniform local V_f,[40,41] but since the CNTs in the A-CMNCs are bound by the polymer matrix and cannot freely move, such an effectany effect from this will be very small when averaged over a sample size of 10^5 CNTs.[40,41] Since this simulation framework can be used to study CNT arrays with V_f up to 40 vol. % CNTs (see Chapter 4),[40] a value near the maximum V_f achievable *via* mechanical densification of chemical vapor deposition grown ~ 8 nm outer diameter CNTs,[29] the results of this analysis will be physical for the entire range of experimentally accessible V_f of the A-CMNCs studied here.

7.4 Results and Discussion

Here, the results of the experimental characterization and modeling of the crystallite geometry (see Section 7.4.1.1), bonding character (see Section 7.4.1.2), chemical structure (see Section 7.4.1.3), and apparent density (see Section 7.4.1.4) are presented, and the processing-dependent structure-property relations of the PyC matrix are established (see Section 7.4.2.1) and applied to quantify the hardness scaling of the A-CMNCs as a function of V_f (see Section 7.4.2.2).

7.4.1 PyC Structure and Morphology

7.4.1.1 Graphitic Crystallite Size and Thickness Scaling

The XRD patterns for the *in situ* and *ex situ* pyrolysis approaches can be found in Figure. 7.7 (*in situ*) and Figure 7.8 (*ex situ*) and are summarized in Table 7.2. As Figure 7.7a (*in situ*) and Figure 7.8a (*ex situ*) illustrate, the diffraction patterns (smoothed using 64-point and 32-point moving averages for Figure 7.7a and Figure 7.8a, respectively) of phenolic resin transforming into PyC exhibit two main peaks of interest: the first is observed at $18^\circ \lessapprox 2\theta \lessapprox 22^\circ$ and belongs to the (002) plane;[221,272] the second is observed at $2\theta \approx 43^\circ$ and belongs to the (100) plane.[221,272] The translation of the (002) peak and large changes in intensity of the (100) peak (relative to the (002) peak) are indicative of a decrease in average crystallite curvature (*i.e.* fluctuation of the d_{002}) and a turbostratic stacking order.[272] Turbostratic stacking order is further supported by the evolution of d_{002} as a function of T_p, as shown in Table 7.2 and Figure 7.8c (*ex situ*), which show that although d_{002} decreases with T_p, d_{002} plateaus at $d_{002} \sim 0.37$ nm and a $d_{002} \lesssim 0.34$ nm value indicative of bernal (*i.e.* ABAB) stacked graphite is not observed. Additionally, the (002) peak may also be related to both annihilation of native defects and an increase in L_c of the graphitic crystallites.[272] These results indicate that while higher T_p leads to lower crystallite curvature and disorder, the crystallites are still not truly graphitic in nature through $T_p = 1400^\circ$C, since the (002) peak is at $2\theta < 26.5^\circ$ ((002) peak position for graphite), and that the glassy crystallite arrangement that is expected for phenol-formaldehyde undergoing pyrolysis likely holds.[273] The diffraction patterns also exhibit a broad low-angle peak at $2\theta = 16.5^\circ$, which is attributed to adjacent chains of linear polymer, and was not analyzed further.[274] Using the (002) and (100) peaks, the geometry of the graphitic crystallites that comprise the PyCs can be studied further.

As Table 7.2 and Figure 7.8b (*ex situ*) illustrate, both L_a and L_c increase with increasing T_p up to $T_p \sim 1000^\circ$C (the maximum T_p for the *in situ* experiment), where the *ex situ* pyrolysis results indicate that L_a plateaus at $L_a \sim 6.3$ nm while L_c continues increasing past $L_c \sim 2$ nm. These values of L_a and L_c indicates that the PyCs studied here are non-graphitizing LD PyCs ($\rightarrow L_a/L_c = 2-3$) that suggests an 'open structure'.[223,242] Phenolic resin is classified as a resole (*i.e.* a hard carbon)

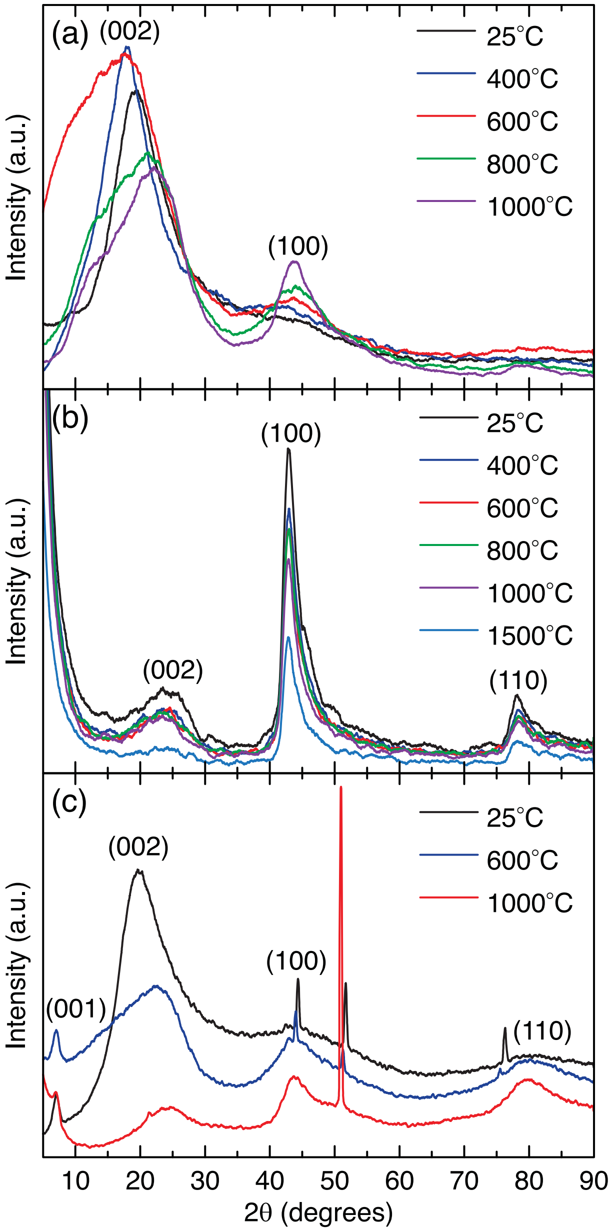

Figure 7.7: XRD analysis results for *in situ* pyrolysis of PyCs, A-CNTs, and A-CMNCs as a function of T_p. (a) XRD patterns of phenolic resin pyrolysis (transforming into PyC) showing the evolution of the (002) and (100) peaks. (b) XRD patterns of A-CNTs heated up to 1500°C demonstrating that heat treatments at $\lesssim$ 1000°C lead to little change in the original CNT structure. (c) XRD patterns of A-PNC precursors transforming into A-CMNCs.

and will therefore not yield graphite even after experiencing temperatures in excess of 2000°C, but rather will produce vitreous (glassy) carbons.

The results of the XRD analysis of A-CNTs undergoing thermal treatment *in situ* are summarized in Figure 7.7b. The XRD patterns (smoothed using a 64-point moving average) confirm the

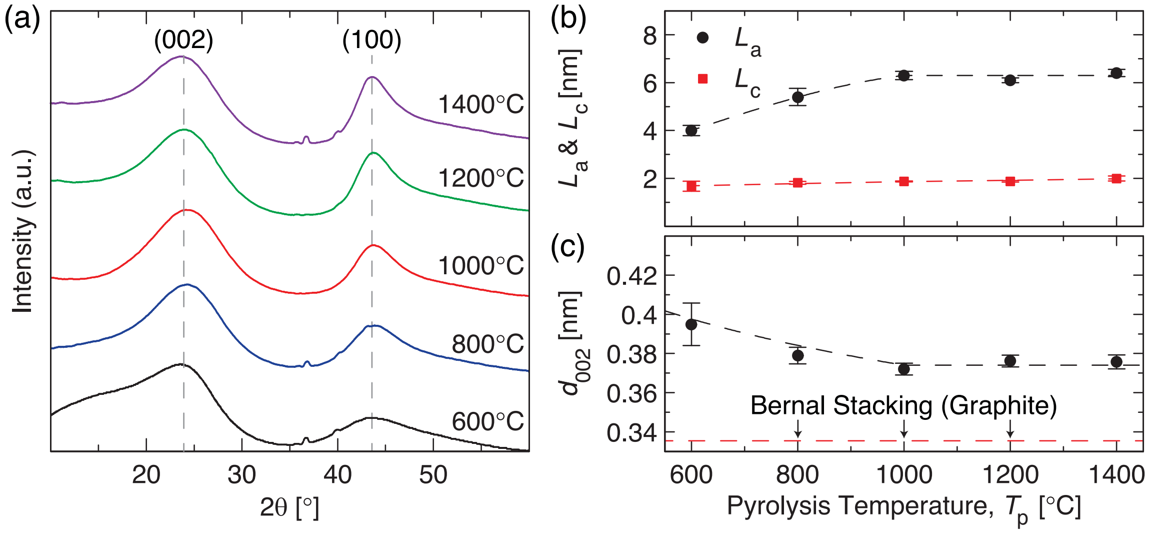

Figure 7.8: XRD analysis results for *ex situ* pyrolysis of PyCs as a function of the pyrolysis temperature (T_p). (a) XRD patterns showing the evolution of the (002) and (100) peaks as a function of T_p. (b) L_a and L_c as a function of T_p. (c) d_{002} evolution as a function of T_p.

graphitic nature of the CNTs. Assuming an AB (Bernal) graphitic stacking, the major peaks of the XRD pattern are identified as (002), (100) and (110) at $2\theta \approx 26°$, 42°, and 78° respectively (these peaks may shift slightly in comparison to the reference graphite pattern).[97,275,276] However, recent work has called into question whether the CNT structure most closely resembles AB (hexagonal) graphitic stacking, and an AA′ (orthorhombic) stacking was suggested instead. Such a change in reference pattern would cause the $(hk\ell)$ plane indexes for the peaks at ~ 42° and 78° to be transformed to (020) and (200) respectively.[97,180,277] Since the information required to determine the stacking order in the CNTs was not available for this study, AB stacking was assumed for the re-

Table 7.2: Crystallite geometry estimated from XRD that includes L_a (via Eq. 7.1a), L_c (via Eq. 7.1b), and d_{002} (via Eq. 7.2) with standard deviation as a function of pyrolysis temperature (T_p) for the *in situ* and *ex situ* pyrolyzation approaches.

T_p [°C]	Approach	PyCs			A-CMNCs		
		L_a [nm]	L_c [nm]	d_{002} [nm]	L_a [nm]	L_c [nm]	d_{002} [nm]
25	*in situ*	2.69 ± 0.43	1.11 ± 0.08	0.376 ± 0.004	–	–	–
600	*in situ*	3.52 ± 0.10	1.44 ± 0.16	0.378 ± 0.10	–	–	–
	ex situ	4.00 ± 0.22	1.67 ± 0.21	0.395 ± 0.011	6.70 ± 0.47	1.91 ± 0.01	0.390 ± 0.008
800	*in situ*	4.40 ± 0.02	1.62 ± 0.08	0.364 ± 0.100	–	–	–
	ex situ	5.40 ± 0.36	1.82 ± 0.06	0.379 ± 0.004	6.40 ± 0.58	1.80 ± 0.13	0.380 ± 0.004
1000	*in situ*	4.83 ± 0.41	2.32 ± 0.35	0.354 ± 0.100	–	–	–
	ex situ	6.30 ± 0.17	1.88 ± 0.02	0.372 ± 0.003	6.60 ± 0.16	1.81 ± 0.04	0.376 ± 0.045
1200	*ex situ*	6.10 ± 0.10	1.88 ± 0.04	0.376 ± 0.003	6.30 ± 0.22	1.95 ± 0.08	0.377 ± 0.001
1400	*ex situ*	6.40 ± 0.15	1.99 ± 0.10	0.376 ± 0.004	6.20 ± 0.25	2.02 ± 0.02	0.375 ± 0.004

mainder of this Chapter, and further work is planned to better quantify the stacking group most representative of the CNTs. As Figure 7.7b illustrates, there are little changes in the XRD pattern at T_p of up to 1000°C, indicating thermal stability. These results are consistent with previous Raman experiments that showed little change in the bonding character of CNTs that were heat treated using the A-CMNC pyrolyzation conditions.[27] However, at 1500°C, significant drops in intensity of the (002), (100), and (110) peaks can be seen (see Figure 7.7b). These decreases in intensity might indicate the formation of new wall defects, but since this temperature is close to the limit of stability of divacancies in graphite ($\propto$ 1400°),[177] the more likely explanation is that the CNTs are starting to experience thermal break-down/decomposition. Further work is necessary to determine mechanism responsible for the observed intensity drop.

As Figure 7.7c (*in situ*) and Figure 7.9a (*ex situ*) illustrate, the XRD patterns (smoothed using a 24-point and 32-point moving averages for Figure 7.7c and Figure 7.9a, respectively) for the pyrolysis of A-CMNCs with $V_f \sim 1\%$ CNTs have features exhibited by both the PyCs (see Figure 7.7a) and the A-CNTs (see Figure 7.7b). The broadening in the (002) peak is similar to the pattern of the phenolic resin at $T_p = 25°$ and PyCs at $T_p = 600°C$. The (002) peak is also shifted towards a higher angle, which is an indicator of a possible increase of crystallinity of the PyC matrix. At $T_p \lesssim 600°$ and at $2\theta \approx 42°$, the overlap of the (100) peaks of the PyC and CNTs can be observed. The overlap of a broad (100) peak (contributed by the PyC, see Figure 7.7a) with a sharp (100) peak

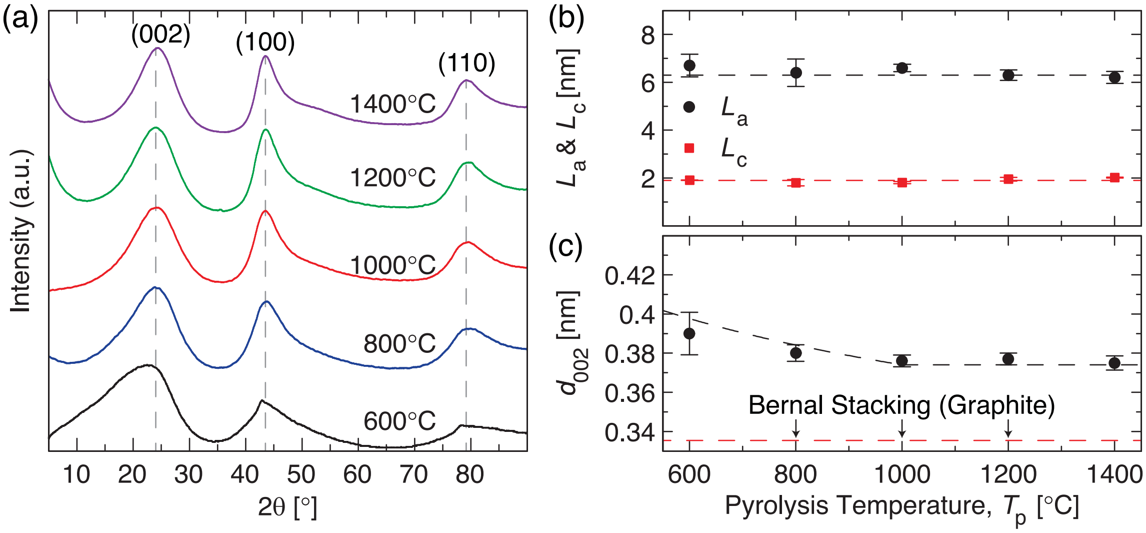

Figure 7.9: XRD analysis results for *ex situ* pyrolysis of A-CMNCs as a function of T_p. (a) XRD patterns showing the evolution of the (002), (100), and (110) peaks as a function of T_p. (b) L_a and L_c as a function of T_p. (c) d_{002} evolution as a function of T_p.

(contributed by the A-CNTs, see Figure 7.7b) could make any structure calculations (*e.g.* L_a and L_c) difficult, especially using the lower resolution instrument used for the *in situ* approach, emphasizing the importance of peak fitting. A similar situation seems to occur at a temperature of $T_p \lesssim 600^\circ$ and at $2\theta \approx 78^\circ$, where a very broad peak contributed by the PyC seems to be overlapping with the sharp peak contributed by the A-CNTs (see Figure 7.7a and Figure 7.7b). However, at $T_p \gtrsim 800^\circ$, there is no distinguishable overlap in the peaks at $2\theta \approx 42^\circ$, and 78°, indicating that the presence of the A-CNTs facilitated the formation and growth of the graphitic crystallites of the A-CMNCs, since the pure PyC pattern does not exhibit a discernible (110) peak (see Figure 7.7a). This is consistent with recent findings in similar A-CMNC systems that observed that the PyC matrix structure becoming more crystalline sooner (*i.e.* at lower T_p) when A-CNTs are present.[256,259] Additionally, evaluation of the L_a, L_c, and d_{002} as a function of T_p (Figure 7.9b and Figure 7.9c, respectively) show that although the A-CNTs help facilitate the formation of the graphitic crystallites, *i.e.* L_a and L_c hit the plateau of $L_a \sim 6.3$ nm and $L_c \sim 2$ nm as observed for PyCs (Figure 7.8b) at a much lower $T_p \sim 600^\circ$C, the scaling of d_{002} as a function of T_p for the crystallites in PyC matrix of the A-CMNCs exactly mirrors the scaling observed for the pure PyCs in Figure 7.8c. This means that although the CNTs help the graphitic crystallites self-organize and grow in L_a, the crystallites that comprise the PyC matrix of the A-CMNCs are not more graphitic in nature than the ones found in the pure PyCs (*i.e.* they are still turbostratic). However, the presence of additional peaks in the A-CMNCs (*i.e.* the (001) peak) that were not seen in the patterns of either pure A-CNTs or PyCs indicates that other bond characters may form when the PyC is processed in the presence of A-CNTs. The additional peaks that are observed occur at $2\theta \approx 10^\circ$, and 50°. The peak that occurs at $2\theta \approx 50^\circ$ in Figure 7.7c is attributed to the LaB_6 standard, and is not included in the analysis. The peak that occurs at $2\theta \approx 10^\circ$ in Figure 7.7c is attributed to C$-$O (*i.e.* graphite oxide) bonding, which has a very distinct (001) peak at that location.[278,279]. This (001) peak is not seen in Figure 7.9a, since the A-CMNCs studied *via ex situ* pyrolysis were only infused once, whereas the *in situ* pyrolysis study examined A-CMNCs that were infused twice, meaning that the re-infusion process may introduce additional C$-$O character in the A-CMNCs that could lead to the additional mechanical reinforcement previously observed.[27] Further work is necessary to elucidate the processing step that leads to the appearance of the (001) peak, and to analyze where specifically that type of bonding occurs (near the CNT surface is a likely candidate).

7.4.1.2 Bonding Character Evolution

Representative Raman spectra for PyCs undergoing pyrolysis at 600°C $\leq T_\mathrm{p} \leq$ 1400°C, and their fitting functions (from Eq. 7.4), are presented in Figure 7.10a. There is no distinction between samples prepared using the *in situ* and *ex situ* approaches since no statistically significant differences between the two batches were found. As Figure 7.10a shows, the main qualitative evolution of the Raman spectra is that the D-band is increasing in intensity. This is confirmed in Figure 7.10b, where the $I_\mathrm{D}/I_\mathrm{G}$ and $A_\mathrm{D}/A_\mathrm{G}$ as a function of T_p are presented. As Figure 7.10b illustrates, $I_\mathrm{D}/I_\mathrm{G}$ and $A_\mathrm{D}/A_\mathrm{G}$ both increase as a function of T_p, which is attributed to thermally-activated defect formation. Although Raman cannot distinguish what kind of defects are forming, the XRD results indicate that the graphitic crystallites that comprise the matrix grow until $T_\mathrm{p} \sim$ 1000°C, at which point L_a and L_c are either constant or grow very slowly. This means that as T_p increases until $T_\mathrm{p} \sim$ 1000°C, the graphitic crystallites are both forming grain boundaries within the (001) family of planes (consistent with a growing L_a) and stacking additional (disordered) graphene-like layers on top of the (001) basal plane (consistent with a growing L_c), while at $T_\mathrm{p} \sim$ 1400°C the graphitic crystallites are mainly growing in the L_c direction that indicates a possible plateau in $I_\mathrm{D}/I_\mathrm{G}$ and $A_\mathrm{D}/A_\mathrm{G}$. This type of behavior is consistent with mode 2 in the amorphization trajectory, but γ_D and γ_G must be evaluated to quantify this (see Figure 7.10c). As Figure 7.10c indicates, γ_D decreases as a function of T_p

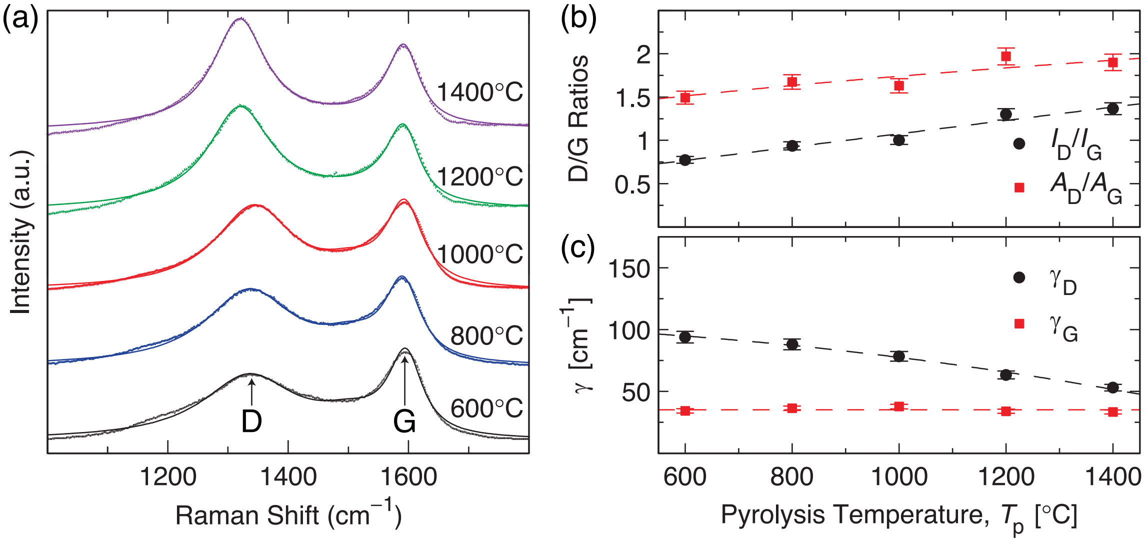

Figure 7.10: Raman spectroscopy analysis results as a function of T_p utilizing samples from both the *in situ* and *ex situ* pyrolysis approaches. (a) Raman spectra (experimental curves and fits *via* Eq. 7.4) showing the evolution of the D and G bands as a function of T_p. (b) Evolution of $I_\mathrm{D}/I_\mathrm{G}$ and $A_\mathrm{D}/A_\mathrm{G}$ as a function of T_p. (c) Scaling of γ_D and γ_G as a function of T_p.

from $\gamma_D \sim 90$ to 50 cm^{-1}, while γ_G remains constant to within the experimental uncertainty at $\gamma_G \sim 35$ cm^{-1}. This value and scaling of γ_G is in very good agreement with a recent study on PyCs that were clearly in stage 2 of the amorphization trajectory (since $\gamma_G > 15$ cm^{-1} for stage 1),[235] where $\gamma_G \sim 40$ cm^{-1} was observed for 4 nm $\lesssim L_a \lesssim$ 6 nm, and where γ_D/γ_G was seen to decrease from $\gamma_D/\gamma_G \sim 2$ to 1.4 (the range is $\gamma_D/\gamma_G \sim 2.5$ to 1.4 here) in the same L_a regime.[271] Additionally, if the PyCs studied here were indeed in stage 1, $I_D/I_G \propto L_a^{-1}$ scaling proposed by Eq. 7.3a and Eq. 7.3b would hold. However, as shown by Figure 7.11 an $I_D/I_G \propto L_a^2$ scaling is supported by the experimental data, which is the appropriate scaling previously proposed for stage 2 of the amorphization trajectory.[228,229,235] Though, direct application of the previously proposed Eq. 7.3c to the I_D/I_G (from Raman spectroscopy) and L_a (from XRD) data does not yield good agreement, which originates from the way the scaling constant of Eq. 7.3c was previously derived in Ref. 228. In Ref. 228, the scaling constant of Eq. 7.3c was evaluated by setting Eq. 7.3c equal

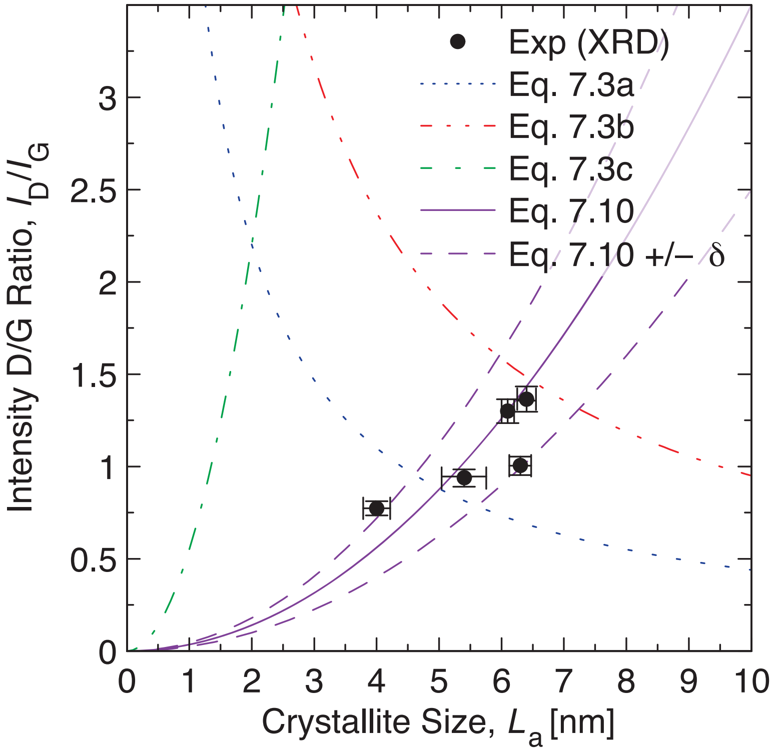

Figure 7.11: Scaling of the intensity ratio of the D- and G-bands (I_D/I_G) as a function of the crystallite size (L_a) showing that the previously proposed approximations of L_a from I_D/I_G (Eq. 7.3)[228,233,234] are not representative here. Since the $I_D/I_G \propto L_a^{-1}$ scaling proposed by Eq. 7.3a and Eq. 7.3b are not exhibited by the experimental data, whereas $I_D/I_G \propto L_a^2$ scaling proposed in Eq. 7.3c is more representative of the experimental data, Eq. 7.10, which modified the intersection point of Eq. 7.3c and Eq. 7.3b to a more realistic value ($\rightarrow L_a \approx 6.5 \pm 0.5$ nm, instead of $\sim 2-3$ nm),[228,229,235] is the only scaling relation that is able to capture the trend in the data.

to Eq. 7.3a at $L_\mathrm{a} = 2$ nm, and solving for the required scaling constant that would yield such an intersection point.[228] More recently, it was reported that stage 2 can extend to $L_\mathrm{a} \sim 3$ nm in Ref. 235 and Ref. 229 which originates from the Fermi velocity of $v_\mathrm{F} \sim 1.1 \times 10^6$ m/s and the lifetime of the photoexcited virtual electron-hole pair ($1/\omega_\mathrm{D}$) of $1/\omega_\mathrm{D} \sim 3$ fs in graphene according to the uncertainty principle,[235,280] but a very recent study proposed that $1/\omega_\mathrm{D}$ could be as high as 5 fs in PyCs,[270] while other work reported that v_F can be increased by $> 2\times$ ($\rightarrow v_\mathrm{F} \sim> 2 \times 10^6$ m/s) through doping and other effects that strengthen electron-electron interactions.[281,282] These enhancements in $1/\omega_\mathrm{D}$ and v_F corresponding to a possible stage 1 $-$ stage 2 point of $v_\mathrm{F}/\omega_\mathrm{D} = L_\mathrm{a} \gtrsim 6$ nm, and here we re-evaluate the scaling constant of Eq. 7.3c at a revised intersection point of $L_\mathrm{a} = 6 \pm 0.5$ nm. Also, since Eq. 7.3a does not take into account the laser excitation energy, the more representative Eq. 7.3b is used except the scaling constant is divided by a factor of 2× to convert Eq. 7.3b from an $A_\mathrm{D}/A_\mathrm{G}$ scaling relation to an $I_\mathrm{D}/I_\mathrm{G}$ scaling relation, as proposed by Ref. 270. Solving for the scaling factor that would unify the $I_\mathrm{D}/I_\mathrm{G} \propto L_\mathrm{a}^{-1}$ scaling proposed by Eq. 7.3b with the $I_\mathrm{D}/I_\mathrm{G} \propto L_\mathrm{a}^{2}$ proposed by Eq. 7.3c, the new transition point of $L_\mathrm{a} = 6 \pm 0.5$ nm yields the following scaling relation:

$$L_\mathrm{a} = \sqrt{\frac{1}{0.035 \pm 0.01}\left(\frac{I_\mathrm{D}}{I_\mathrm{G}}\right)} \tag{7.10}$$

where the uncertainty in the scaling factor corresponds to the uncertainty in the intersection point. As illustrated by Figure 7.11, Eq. 7.10 is able to nicely capture the observed scaling of $I_\mathrm{D}/I_\mathrm{G}$ as a function of L_a. However, the exact mechanism that leads the crossover point of stage 2 to stage 1 to shift by nearly 3 nm is not yet known, and further work by experiments, theory, and simulation is needed to pinpoint the phenomena responsible that is likely defect density related.

The evolution of the Raman spectra of the A-CMNCs as a function of V_f (up to $V_\mathrm{f} \sim 10\%$) is presented in Figure 7.12a. As Figure 7.12 demonstrates, increasing V_f does not change the bonding character of the PyC matrix significantly. This is exemplified by Figure 7.12b that shows that $I_\mathrm{D}/I_\mathrm{G}$ and $A_\mathrm{D}/A_\mathrm{G}$ do not evolve significantly as a function of V_f and stay approximately constant at $I_\mathrm{D}/I_\mathrm{G} \sim 1.3$ and $A_\mathrm{D}/A_\mathrm{G} \sim 1.7$. Additionally, Figure 7.12c demonstrates that γ_D and γ_G are also approximately constant at $\gamma_\mathrm{D} \sim 50$ cm^{-1} and $\gamma_\mathrm{G} \sim 35$ cm^{-1}, which indicates that the A-CMNCs are in the exact same place in the amorphization trajectory regardless of V_f. This is consistent with the XRD findings for A-CMNCs (see Figure 7.9) that show that while the presence of the A-CNTs within the PyC matrix of A-CMNCs helps the graphitic crystallites grow and self-organize

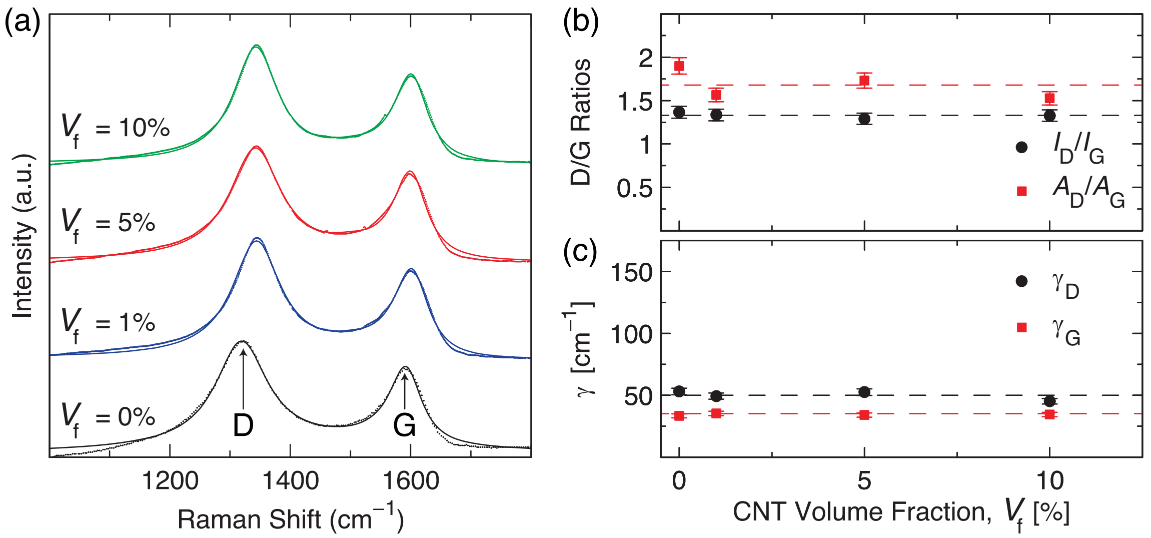

Figure 7.12: Raman spectroscopy analysis results for A-CMNCs as a function of the CNT volume fraction (V_f). (a) Raman spectra (experimental curves and fits *via* Eq. 7.4) showing the evolution of the D and G bands as a function of V_f. (b) Evolution of I_D/I_G and A_D/A_G as a function of V_f. (c) Scaling of Γ_D and Γ_G of the D and G bands as a function of V_f.

(quantified *via* L_a), the graphitic nature of the crystallites that form in the PyC matrix of the A-CMNCs is comparable to graphitic nature of the crystallites that form in the pure PyCs (quantified *via* d_{002}). Such a result indicates that processing parameter that governs the graphitic nature of the crystallites that comprise the PyC matrix is T_p, and not V_f. Further work to explore whether higher CNT confinement (*i.e.* higher V_f) leads to a modification of the graphitic nature of the PyC matrix is needed to expand on these preliminary findings.

7.4.1.3 Chemical Structure Evolution

Representative FTIR patterns for the *in situ* and *ex situ* pyrolysis approaches can be found in Figure. 7.13 (*in situ*) and Figure 7.14 (*ex situ*). As Figure 7.13a shows the cured phenolic resin ($T_p \sim 25$°C) exhibits a band found at ~ 1600 cm^{-1} that is an indicator of aromatic in-ring stretching,[283] a band at ~ 1233 cm^{-1} due to phenolic $-$OH and C$-$O stretching, a band at ~ 1374 cm^{-1} belonging to $-$OH functional groups,[284] and bands characteristic of the methylene (=CH$_2$) functional group at ~ 913 cm^{-1} and ~ 1474 cm^{-1} indicative of the formation of the methylene links during the curing process, and bands at ~ 818 cm^{-1} and ~ 756 cm^{-1} characteristic of ortho-disubstituted and meta-disubstituted aromatic compounds.[285] As Figure. 7.13a and Figure 7.14a demonstrate, during pyrolysis, the chemical structure of the PyCs is evolving toward a polyaromatic structure.[286] Evidence is shown in the ~ 1636 cm^{-1} peak, which originates from the C=C stretch-

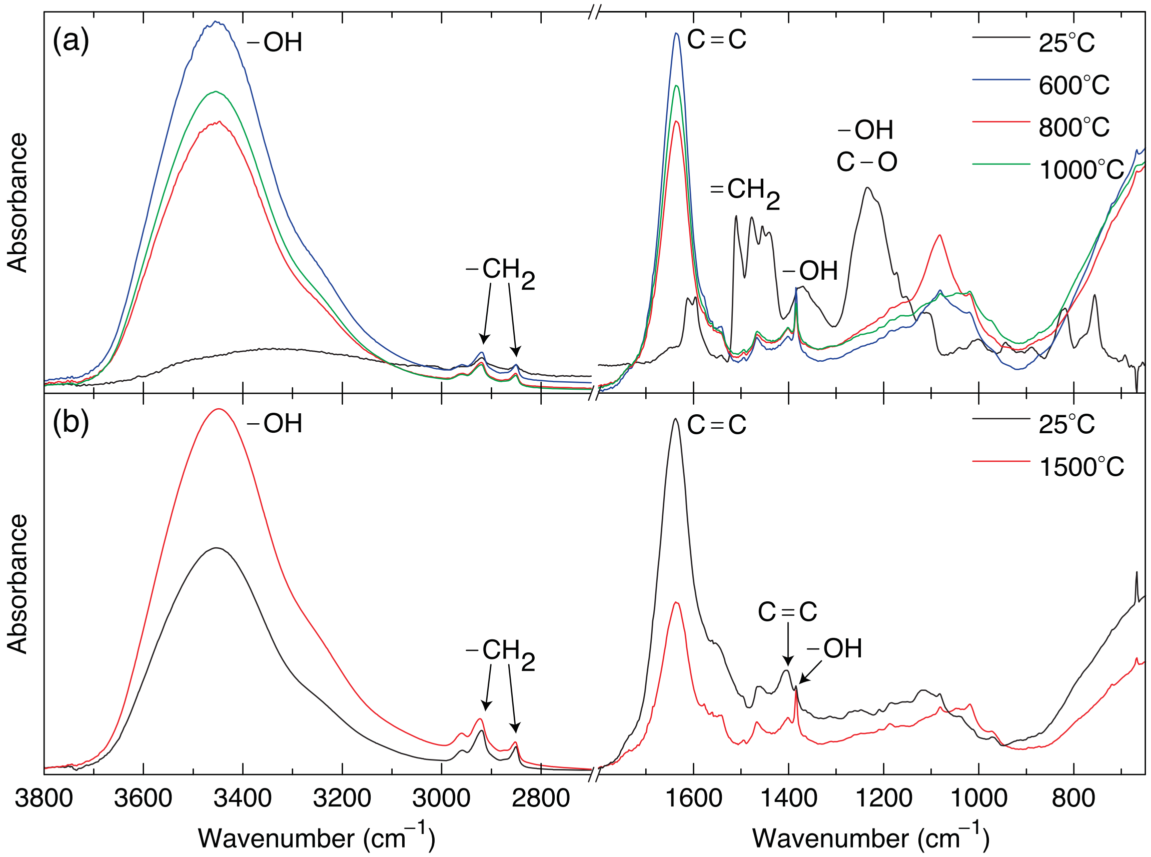

Figure 7.13: Representative FTIR spectra for *in situ* pyrolysis of PyCs and A-CNTs. (a) FTIR spectra for cured phenolic resin transforming into PyC for T_p up to 1000°C illustrating that −OH groups are present on the surface of the PyCs, and that $C-O_2$, H_2O and methylene groups are released as byproducts of the pyrolyzation leading the bands at 1233 cm^{-1} and 1474 cm^{-1} to disappear, and a band corresponding to a more complex polyaromatic system to appear at 1636 cm^{-1}. (b) FTIR spectra of A-CNTs before and after thermal treatment at $T_p = 1500$°C demonstrating that −OH groups are present on the surface of the CNTs, as observed previously,[46] and that the CNTs that comprise the A-CNTs are highly thermally stable since no chemical structure alterations are seen at < 1800 cm^{-1}.

ing in the aromatic rings. The broadening of the $\sim$ 1636 cm^{-1} band is also attributed to C−O in the benzophenone groups.[244] Having both peaks around $\sim$ 1374 cm^{-1} and $\sim$ 1636 cm^{-1} could also indicate the presence of C−O stretching originating from carboxyl groups. The changes in the aromatic parts (675-900 cm^{-1}) as a function of the pyrolysis temperatures can be traced back to the proportion of −CH groups present in the condensed aromatic structures, and those found in the phenyl ring.[286] This indicates that the changes are related to the interaction between the phenolic groups, which results in further cross-linking *via* ether bridges. The band observed at $\sim$ 3455 cm^{-1} is an indicator of −OH stretching in the samples after pyrolization. The presence of an −OH band is characteristic of a thermoset resin such as phenol-formaldehyde. In general, thermoset resins

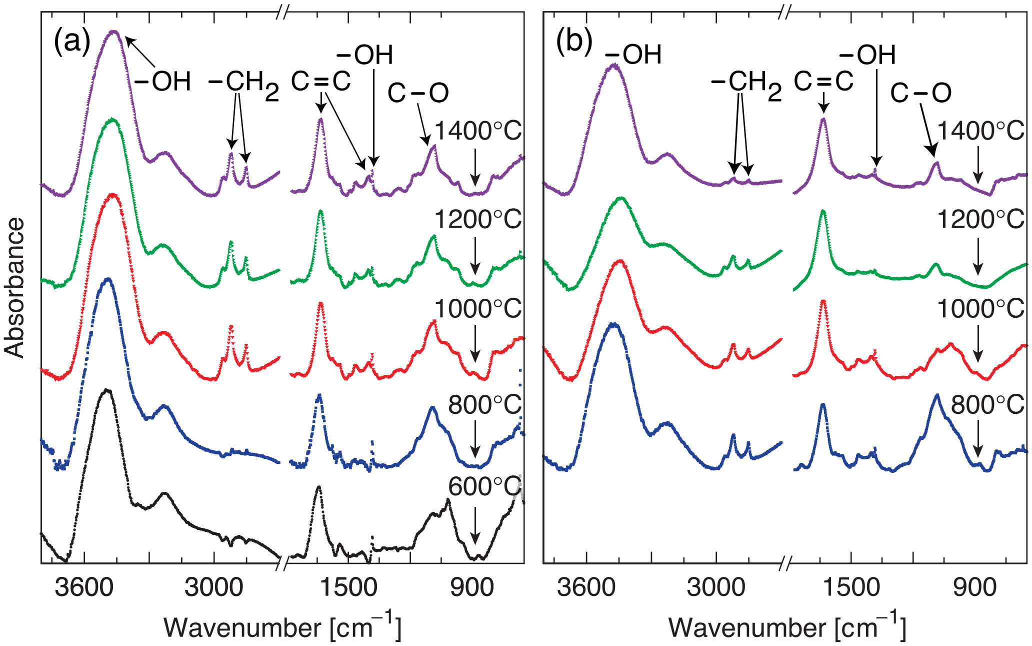

Figure 7.14: Representative FTIR spectra for *ex situ* pyrolysis of PyCs and A-CMNCs as a function of the pyrolysis temperature (T_p). (a) FTIR spectra for PyCs as a function of T_p up to 1400°C. (b) FTIR spectra of A-CMNCs as a function of T_p up to 1400°C showing slight changes in the chemical structure of A-CMNCs as a function of T_p.

absorb more water than thermoplastic resins,[287] and elevated temperatures may influence the rate of moisture absorption in polymers in a complex manner.[288] A similar situation may also occur in composites materials that contain thermoset resins as the matrix.[289] Further analysis must be done to understand the relation between temperature and moisture absorption, specifically in phenolic resins, since it is currently not well understood.[290,291]

FTIR was also performed on A-CNTs before and after *in situ* thermal processing (See Figure 7.13b). No great alteration in the CNT chemical structure were observed.[9] The band at ~ 1403 cm^{-1} and ~ 1640 cm^{-1} are due to in-ring stretching of the aromatic carbons. The difference in peak broadening and intensity may indicate that small amount of defects are forming in the CNT walls as the temperature increases.[292] This argument is due to the bands at ~ 2851 cm^{-1} and ~ 2920 cm^{-1} which show nearly insignificant $-\mathrm{CH_2}$ alterations. An $-\mathrm{OH}$ stretching band is observed at ~ 3454 cm^{-1} for A-CNTs before and after *in situ* thermal processing, which agrees with recent findings that indicate the presence of water on the surface of CNTs in ambient conditions.[46] These FTIR results indicate that the chemical structure of the A-CNTs that comprise the A-CMNCs will not evolve significantly in the $600°\mathrm{C} \leq T_\mathrm{p} \leq 1400°\mathrm{C}$ regime studied here.

Additional insight into the chemical structure of A-CMNCs is provided in Figure 7.14b for

A-CMNCs prepared *via* the *ex situ* pyrolysis approach. As Figure 7.14 illustrates, the FTIR spectra of PyCs (Figure 7.14a) and A-CMNCs (Figure 7.14b) are very similar, and exhibit clear $-$OH stretches from water at ~ 3400 cm^{-1} and ~ 650 cm^{-1}. The band at ~ 1640 cm^{-1} suggests significant C$=$C bonding throughout both the PyCs and A-CMNCs. Also, inorganic carbonate C$-$O and O$-$C$-$C stretches at $\sim 1100-1130$ cm^{-1} suggest significant oxygen presence throughout the material as expected, and indicated by the A-CMNC XRD pattern. It is possible that the oxygen serves as a coupling agent between the CNTs and the PyC crystallites, but further work is required to elucidate the role oxygen plays in the PyC matrix of the A-CMNCs. Although FTIR indicates the possibility of small chemical changes as T_p increases, this chemical structure evolution is consistent with the XRD findings, *i.e.* that the A-CMNC structure is not affected within the T_p regime studied here. However, since FTIR cannot quantify the differences in the A-CMNC chemical structure as a function of T_p, further study *via* the more quantitative XPS technique is needed.

7.4.1.4 Apparent Density Scaling

The experimentally determined ρ_pyc of the PyCs studied here (see Table 7.3), along with the previously reported ρ_pyc from Ref. 241 and Ref. 242, are summarized as a function of L_a/L_c and

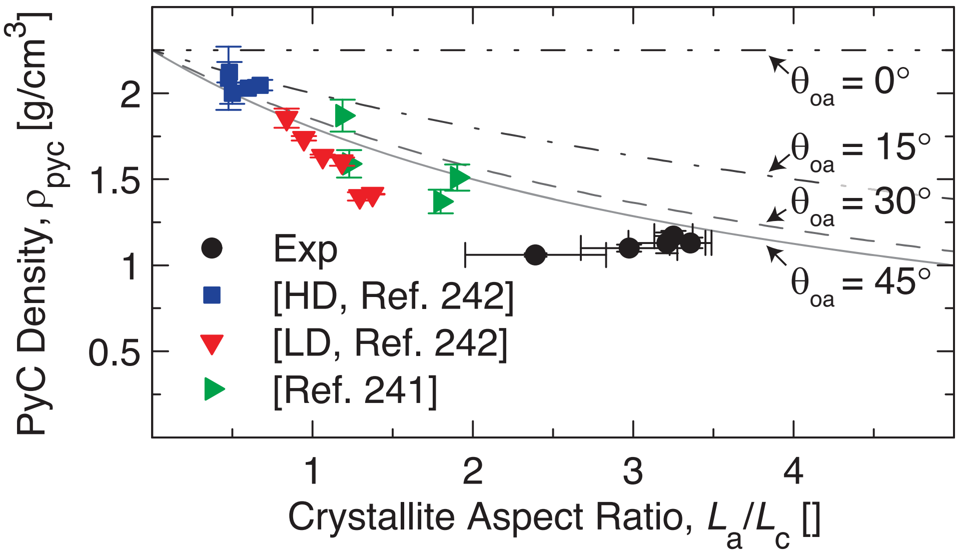

Figure 7.15: Evolution of PyC density, ρ_pyc (from Eq. 7.6), as a function of crystallite geometry, L_a/L_c, and orientation angle, θ_oa. The predictions of Eq. 7.6 agree very well with previous data on ρ_pyc for HD PyCs (from Zhang et al.[242]), but overestimates ρ_pyc for LD PyCs (from the current work, Yajima et al.[241], and Zhang et al.[242]) due to the presence of a significant amount of > 100 nm diameter pores in such PyCs.

θ_{oa} in Figure 7.15. As Figure 7.15 indicates, there is good agreement between predicted (from Eq. 7.6) and reported ρ_{pyc} for HD PyCs from Ref. 242, which was previously observed to have $15^\circ \lesssim \theta_{\mathrm{oa}} \lesssim 30^\circ$.[242] However, the predictions of Eq. 7.6 diverge noticeably from the experimentally determined ρ_{pyc} of the LD PyCs studied in Ref. 242. This can be attributed to both the degree of graphitization of the PyCs, *i.e.* LD PyCs with $L_a/L_c \lesssim 1$ were shown to have $\theta_{\mathrm{oa}} \sim 30-35^\circ$ corresponding to an error of $\lesssim 10\%$ when comparing the predicted ρ_{pyc} to the reported values,[242,293] and the population of > 100 nm large pores present in the PyC matrix, which was previously shown to be very significant.[294] This means that Eq. 7.6, in addition to the XRD, Raman spectroscopy, and FTIR spectroscopy results, can help discern whether the PyC exhibits an LD or HD structure, as long as additional information on the porosity of the PyC matrix is considered. Applying Eq. 7.6 to other LD PyCs, such as the PyCs studied here and in Ref. 241, shows that there are likely significant matrix porosities in both PyC systems, and that the PyCs studied here annihilate the excess matrix porosity as T_{p} increases. This is emphasized by the evolution of ρ_{pyc} as a function of L_a/L_c, which increases from $L_a/L_c \sim 2.4$ at $T_{\mathrm{p}} = 600$°C to $L_a/L_c \sim 3.3$ at $T_{\mathrm{p}} = 1400$°C, while ρ_{pyc} changes very little. Such an evolution indicates that the graphitic crystallites in the PyCs studied here are growing at the expense of the porosity, which is indicative of the crystallites becoming more interconnected. Such a structural evolution would correspond to enhanced PyC mechanical properties, which are quantified and modeled in Section 7.4.2.1.

Table 7.3: Experimental and theoretical (from Eq. 7.6 and Eq. 7.7b) values of hardness (H_{V}) and apparent density (ρ_{pyc}) for PyCs as a function of pyrolysis temperature (T_{p}), and the experimental specific hardness using the H_{V}/ρ and H_{V}/ρ^2 design parameters for comparison with other superhard materials. Since the current theoretical model for ρ_{pyc} is not capable of accounting for porosity in the PyCs, the predicted ρ_{pyc} values are significantly higher than those measured experimentally, thereby leading to the theoretical H_{V}/ρ and H_{V}/ρ^2 to be far lower than their experimental equivalents.

T_{p} [°C]	Approach	H_{V} [GPa]	ρ_{pyc} [g/cm^3]	H_{V}/ρ [GPa $\times$ cm^{3}g^{-1}]	H_{V}/ρ^2 [GPa $\times$ cm^{6}g^{-2}]
600	Experimental	2.10 ± 0.06	1.06 ± 0.01	1.98 ± 0.08	1.87 ± 0.09
	Theory	2.01 ± 0.75	1.41 ± 0.10	1.43 ± 0.64	1.01 ± 0.53
800	Experimental	3.20 ± 0.06	1.10 ± 0.02	2.91 ± 0.11	2.64 ± 0.15
	Theory	3.08 ± 0.62	1.29 ± 0.06	2.39 ± 0.59	1.85 ± 0.55
1000	Experimental	4.00 ± 0.06	1.13 ± 0.03	3.54 ± 0.15	3.13 ± 0.21
	Theory	3.93 ± 0.29	1.22 ± 0.02	3.22 ± 0.29	2.64 ± 0.28
1200	Experimental	3.70 ± 0.06	1.17 ± 0.03	3.16 ± 0.13	2.70 ± 0.18
	Theory	3.68 ± 0.28	1.24 ± 0.02	2.97 ± 0.27	2.39 ± 0.26
1400	Experimental	3.50 ± 0.06	1.13 ± 0.06	3.10 ± 0.22	2.74 ± 0.34
	Theory	3.62 ± 0.54	1.25 ± 0.04	2.90 ± 0.5	2.32 ± 0.50

7.4.2 Mechanical Behavior Scaling

7.4.2.1 Pyrolysis Temperature Dependence

The scaling of H_V as a function of T_p is presented in Figure 7.16 (and Table 7.3). As Figure 7.16 demonstrates, H_V for the PyCs increases from $H_\mathrm{V} \sim 2.1$ GPa at $T_\mathrm{p} = 600°\mathrm{C}$ to $H_\mathrm{V} \sim 4.0$ GPa at $T_\mathrm{p} = 1000°\mathrm{C}$, and then subsequently decreases to $H_\mathrm{V} \sim 3.5$ GPa at $T_\mathrm{p} = 1400°\mathrm{C}$. See Table 7.3 for the experimentally and theoretically determined H_V and ρ_pyc as a function of T_p. While this non-monotonic scaling of H_V as a function of T_p may seem counterintuitive, Eq. 7.7b in combination with L_a, L_c, and d_{002} is able to explain this behavior. To do so, an approximation for C_{44} must first be established, and since XRD indicates that the PyCs studied here exhibit turbostratic stacking, with $d_{002} > 0.35$ nm, C_{44} can be estimated with $C_{44} \sim 0.35$ GPa. Next, the evolution of $L_\mathrm{a}/L_\mathrm{c}$ as a function of T_p needs to be examined. Using the values for L_a and L_c from XRD, $L_\mathrm{a}/L_\mathrm{c}$ is seen to increase from $L_\mathrm{a}/L_\mathrm{c} \sim 2.4$ at $T_\mathrm{p} = 600°\mathrm{C}$ to $L_\mathrm{a}/L_\mathrm{c} \sim 3.4$ at $T_\mathrm{p} = 1000°\mathrm{C}$, and then subsequently decreases to $L_\mathrm{a}/L_\mathrm{c} \sim 3.2$ at $T_\mathrm{p} = 1400°\mathrm{C}$. Using the scaling relation proposed in Eq. 7.7 and $C_{44} \sim 0.35$ GPa, the theoretical H_V evolution is: H_V increases from $H_\mathrm{V} \sim 2.0$ GPa at $T_\mathrm{p} = 600°\mathrm{C}$ to $H_\mathrm{V} \sim 3.9$ GPa at $T_\mathrm{p} = 1000°\mathrm{C}$, and then subsequently decreases to $H_\mathrm{V} \sim 3.6$ GPa at $T_\mathrm{p} = 1400°\mathrm{C}$. See Table 7.3 for details. This theoretical evolution of H_V is in very good agreement with the

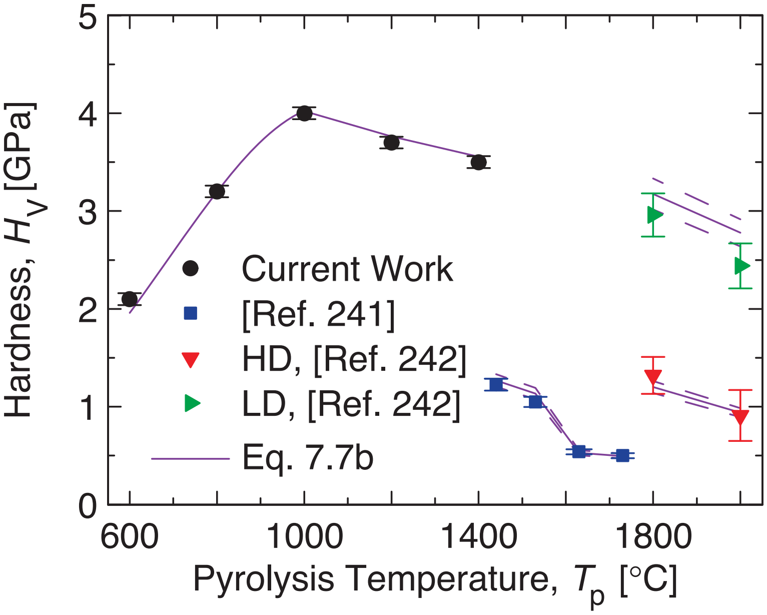

Figure 7.16: Scaling of hardness (H_V) as a function of pyrolysis temperature (T_p) for the PyCs studied here, and in previous works.[241,242] Good agreement with Eq. 7.7b indicates that the low inter-layer shear modulus of the graphitic crystallites governs the measured H_V.

experimental observations.

This analysis can be extended to H_{V} results previously reported for PyCs in Refs. 241 and 242. In Ref. 241, there were many samples studied, but only 4 different T_{p}. This means that the data from Ref. 241 is representative data that originates from the results of multiple samples. Additionally, since the results from Ref. 241 that are included in Figure 7.16 originate from samples that exhibit $d_{002} \gtrsim 0.35$ nm, C_{44} for this data set can be estimated using $C_{44} \sim 0.35$ GPa for turbostratic carbon. As Figure 7.16 demonstrates (error bars and dashed lines are guides to the eye and correspond to ±5% uncertainty in the data and Eq. 7.7b predictions, respectively), Eq. 7.7b in combination with the reported values of L_{a} and L_{c} lead to a predicted H_{V} that decreases from $H_{\mathrm{V}} \sim 1.3$ GPa at $T_{\mathrm{p}} \sim 1440°\mathrm{C}$ to $H_{\mathrm{V}} \sim 0.5$ GPa at $T_{\mathrm{p}} \sim 1730°\mathrm{C}$ in very good agreement with the reported values ($H_{\mathrm{V}} \sim 1.2$ GPa at $T_{\mathrm{p}} \sim 1440°\mathrm{C}$ and $H_{\mathrm{V}} \sim 0.5$ GPa at $T_{\mathrm{p}} \sim 1730°\mathrm{C}$, respectively). These results for Ref. 241 indicate that although increasing T_{p} will lead to larger graphitic crystallites, the PyC matrix will become significantly less stiff as a result of the observed growth in L_{c} outpacing the reported growth in L_{a}. In Ref. 242, there were more than 5 LD and HD PyC samples studied, but only 2 different T_{p}. This means that, as for the PyCs in for Ref. 241, the HD PyC and LD PyC data points from Ref. 242 are representative data that originate from the results of multiple samples. Additionally, since Ref. 242 does not include an estimate of the d_{002} of any of their samples, but their HD and LD PyCs that have $\rho_{\mathrm{pyc}} \gtrsim 1.7$ g/cm^3 agree very well with the predictions of Eq. 7.6 and have $L_a/L_c \lesssim 1$ characteristic with large degree of graphitic character within the crystallites (but not necessarily $\theta_{\mathrm{oa}} < 30°$),[223] C_{44} for the samples that fulfill these ρ_{pyc} and L_a/L_c requirements (*i.e.* all HD PyC data and two LD PyC data points) can be estimated using $C_{44} \sim 4.5$ GPa for ABAB hexagonal graphite.

As Figure 7.16 demonstrates (error bars and dashed lines are guides to the eye and correspond to reported experimental uncertainty in the Ref. 242 data and ±5% uncertainty in the Eq. 7.7b predictions, respectively), Eq. 7.7b in combination with the reported values of L_{a} and L_{c} values of the HD PyCs lead to a predicted H_{V} that decreases from $H_{\mathrm{V}} \sim 1.2$ GPa at $T_{\mathrm{p}} \sim 1800°\mathrm{C}$ to $H_{\mathrm{V}} \sim 0.9$ GPa at $T_{\mathrm{p}} \sim 2000°\mathrm{C}$ in very good agreement with the reported values ($H_{\mathrm{V}} \sim 1.3$ GPa at $T_{\mathrm{p}} \sim 1800°\mathrm{C}$ and $H_{\mathrm{V}} \sim 0.9$ GPa at $T_{\mathrm{p}} \sim 2000°\mathrm{C}$, respectively). Also, as Figure 7.16 shows (error bars and dashed lines are guides to the eye and again correspond to reported experimental uncertainty in the Ref. 242 data and ±5% uncertainty in the Eq. 7.7b predictions, respectively), Eq. 7.7b in combination with the reported values of L_{a} and L_{c} values of the LD PyCs lead to a predicted H_{V} that decreases from $H_{\mathrm{V}} \sim 3.1$ GPa at $T_{\mathrm{p}} \sim 1800°\mathrm{C}$ to $H_{\mathrm{V}} \sim 2.7$ GPa at $T_{\mathrm{p}} \sim 2000°\mathrm{C}$ in very good agreement with the reported values ($H_\mathrm{V} \sim 3.0$ GPa at $T_\mathrm{p} \sim 1800$°C and $H_\mathrm{V} \sim 2.5$ GPa at $T_\mathrm{p} \sim 2000$°C, respectively). These results for Ref. 242, like the observed trends in Ref. 241, indicate that increasing T_p will make the graphitic crystallites more graphitic in nature, and thereby diminish the stiffness of the PyC matrix and resulting A-CMNCs. Therefore, the results presented in Figure 7.16 demonstrate that in aerospace applications, where high hardness/stiffness and low density are desired, the T_p that is most likely to yield the best performing PyCs, and A-CMNCs, is $T_\mathrm{p} \sim 1000$°C for the system studied here.

Material selection for aerospace structures requires that a candidate material, *i.e.* the PyCs and

Table 7.4: Literature values of the apparent density (ρ) and hardness (H_V) for PyCs,[241,242] other carbon materials,[295] and superhard carbides, nitrides, oxides, and phosphides,[296–300] and their respective specific hardness *via* the H_V/ρ and H_V/ρ^2 design parameters.

Designation	Material	H_V [GPa]	ρ [g/cm^3]	H_V/ρ [GPa × cm^{3}g^{-1}]	H_V/ρ^2 [GPa × cm^{6}g^{-2}]
carbon	diamond	96 ± 5	3.51	27.4 ± 1.4	7.8 ± 0.4
	PyC	$0.50 - 3.0$	$1.37 - 2.12$	$0.3 - 1.4$	$0.2 - 0.7$
	graphite	$0.21 - 0.42$	$1.82 - 1.92$	$0.1 - 0.2$	$0.07 - 0.1$
	C/C	$0.15 - 0.20$	$1.67 - 1.83$	~ 0.1	~ 0.05
carbides	TiC	30 ± 2	4.93	6.1 ± 0.4	1.2 ± 0.1
	ZrC	26 ± 2	6.73	3.9 ± 0.3	0.57 ± 0.04
	$\beta-$SiC	26 ± 2	3.21	8.1 ± 0.6	2.5 ± 0.2
	NbC	18 ± 2	7.82	2.3 ± 0.3	0.29 ± 0.03
	WC	18 ± 2	15.63	1.1 ± 0.1	0.07 ± 0.01
nitrides	c$-$BN	63 ± 5	3.48	18.1 ± 1.4	5.2 ± 0.4
	$\beta-$Si$_3$N$_4$	30 ± 2	3.19	9.4 ± 0.6	3.0 ± 0.2
	TiN	20 ± 2	5.40	3.7 ± 0.4	0.69 ± 0.07
	ZrN	18 ± 1	7.09	2.5 ± 0.1	0.36 ± 0.02
	VN	15 ± 1	6.13	2.4 ± 0.2	0.40 ± 0.03
	NbN	14 ± 1	8.47	1.7 ± 0.1	0.20 ± 0.01
	AlN	12 ± 1	3.26	3.7 ± 0.3	1.1 ± 0.1
	GaN	12 ± 2	6.15	2.0 ± 0.3	0.32 ± 0.05
	InN	9 ± 1	6.81	1.3 ± 0.1	0.19 ± 0.02
oxides	SiO$_2$	33 ± 2	4.29	7.7 ± 0.5	1.8 ± 0.1
	RuO$_2$	30 ± 2	6.97	2.9 ± 0.3	0.41 ± 0.04
	Al$_2$O$_3$	20 ± 2	3.95	5.1 ± 0.5	1.3 ± 0.1
	ZrO$_2$	13 ± 2	5.68	2.3 ± 0.4	0.40 ± 0.06
	YO$_2$	7.5 ± 1	5.01	1.5 ± 0.2	0.30 ± 0.04
phosphides	BP	33 ± 2	2.90	11.4 ± 0.7	3.9 ± 0.2
	GaP	9.5 ± 1	4.14	2.3 ± 0.2	0.55 ± 0.06
	AlP	9.4 ± 1	2.85	3.3 ± 0.4	1.2 ± 0.1
	InP$_2$	5.4 ± 0.5	4.81	1.1 ± 0.1	0.23 ± 0.02

A-CMNCs studied here, be compared to all other materials available using two governing design parameters for hard lightweight materials (*i.e.* E_{eff}/ρ and E_{eff}/ρ^2).[301] Since E_{eff} can be readily converted into H_{V} *via* empirical relations,[267,298] H_{V}/ρ and H_{V}/ρ^2 can be used in a similar way compare the performance of superhard materials whose E_{eff}, which is normally evaluated using tensile testing that may not be appropriate for ceramics, may not be readily available. The experimental ρ_{pyc} and H_{V} results for the PyCs are compared to literature values for PyCs,[241,242] other carbon materials,[295] and superhard carbides, nitrides, oxides, and phosphides,[296–299] in a ρ vs. H_{V} Ashby-like chart (See Figure 7.17). See Table 7.4 for details. As Figure 7.17 demonstrates, H_{V} of the PyCs studied here, on an absolute scale, is higher than the previously reported values for PyCs, graphite, and C/C, but is significantly lower than the H_{V} of other superhard materials. However, when the H_{V}/ρ design parameter, which is used for designing lightweight materials, is utilized to compare the H_{V} values, Figure 7.17 and Table 7.4 illustrate that the performance of the PyCs pyrolyzed at $T_{\mathrm{p}} = 1000°\mathrm{C}$ ($\rightarrow H_{\mathrm{V}}/\rho \sim 3.5$ GPa $\times$ $\mathrm{cm}^3\mathrm{g}^{-1}$) become comparable to the superhard AlP, AlN, TiN, and ZrC. Additionally, when the H_{V}/ρ^2 aerospace design parameter, which is used for designing lightweight materials, is utilized to analyze the performance of the PyCs, Figure 7.17 and

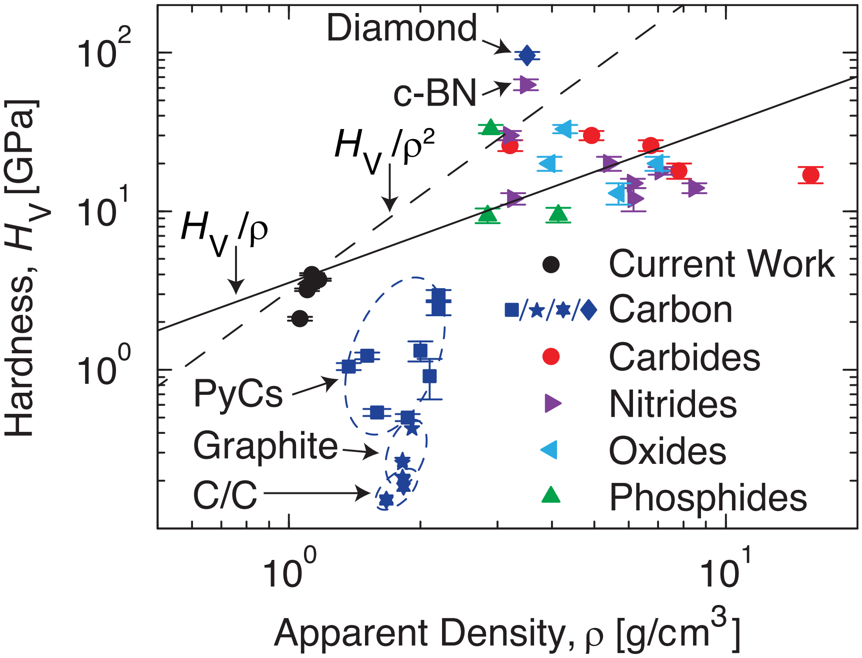

Figure 7.17: Hardness (H_{V}) as a function of apparent density (ρ) for the PyCs studied here and various other PyCs,[241,242] carbon materials,[295] and superhard materials such as carbides, nitrides, oxides, and phosphides[296–300] showing that for lightweight applications such as aerospace (*i.e.* design parameter of H_{V}/ρ^2), PyCs are among the leading candidate materials.

Table 7.4 illustrate that the PyCs pyrolyzed at $T_\mathrm{p} = 1000°\mathrm{C}$ ($\rightarrow H_\mathrm{V}/\rho^2 \sim 3.1$ GPa × cm^{6}g^{-2}) are comparable in performance to the superhard BP and $\beta-\mathrm{Si_3N_4}$, where only diamond and c-BN have higher performance. This means that through additional work on the optimization of the structure of the PyCs, these materials can become among the leading candidates for the design and manufacture of high hardness low density material structures, especially for aerospace applications.

7.4.2.2 Scaling of Axial Effective Modulus with CNT Packing Proximity

The experimental and theoretical scaling of H_V for A-CMNCs synthesized at $T_\mathrm{p} = 1400°\mathrm{C}$ are summarized in Table 7.5. This T_p was selected to maximize the chance of strong binding between the CNTs and the PyC matrix, and since XRD indicates that the PyC matrix in the A-CMNCs does not evolve significantly in the studied T_p regime, H_V of the PyC matrix would likely be the same for any A-CMNC produced at T_p ranging from $\sim 600°\mathrm{C}$ to $\sim 1400°\mathrm{C}$. As Table 7.5 illustrates, H_V increases as V_f increases, and peaks at $V_\mathrm{f} \sim 10\%$ where $H_\mathrm{V} \sim 4.3$ GPa. To compare to the results of a previous simulation study of the mechanical behavior of A-CMNCs that have an a-C matrix,[159] a previously reported empirical conversion factor of $E_\mathrm{cmnc}/H_\mathrm{V} \sim 10 \pm 2\times$ (from Figure 7.4) as shown by Figure 7.18 is used.[267] Using the experimental (axial) E_cmnc values that were converted from H_V, the model detailed in Section 7.3.2.3 was used at $Y/G \sim 30$ to study the scaling of $E_\mathrm{cmnc}(V_\mathrm{f})$ up to $V_\mathrm{f} \sim 30\%$, as presented in Figure 7.18. See Chapter 6 for the compliance

Table 7.5: Experimental and theoretical (from Eq. 7.6 and Eq. 7.7b) values of hardness (H_V) and apparent density (ρ_cmnc) of A-CMNCs as a function of the pyrolysis temperature (T_p), and the experimental specific hardness using the H_V/ρ and H_V/ρ^2 design parameters for comparison with other superhard materials.

V_f [%]	Approach	H_V [GPa]	ρ_cmnc [g/cm^3]	H_V/ρ [GPa × cm^{3}g^{-1}]	H_V/ρ^2 [GPa × cm^{6}g^{-2}]
0	Experimental	3.50 ± 0.06	1.13 ± 0.06	3.10 ± 0.22	2.74 ± 0.34
1	Experimental	3.51 ± 0.20	0.9 ± 0.1	3.9 ± 0.7	4.3 ± 1.2
	Theory	~ 3.50	1.14 ± 0.06	3.07 ± 0.16	2.69 ± 0.29
5	Experimental	3.67 ± 0.10	0.9 ± 0.1	4.1 ± 0.6	4.5 ± 1.2
	Theory	3.80 ± 0.04	1.16 ± 0.06	3.28 ± 0.20	2.82 ± 0.32
10	Experimental	4.30 ± 0.10	0.9 ± 0.1	4.8 ± 0.7	5.3 ± 1.3
	Theory	4.53 ± 0.11	1.19 ± 0.05	3.81 ± 0.25	3.20 ± 0.35
15	Theory	5.64 ± 0.21	1.22 ± 0.05	4.62 ± 0.36	3.79 ± 0.45
20	Theory	7.20 ± 0.33	1.24 ± 0.05	5.81 ± 0.48	4.68 ± 0.57
25	Theory	9.31 ± 0.53	1.27 ± 0.05	7.33 ± 0.71	5.77 ± 0.79
30	Theory	12.10 ± 0.63	1.30 ± 0.04	9.31 ± 0.77	7.16 ± 0.82

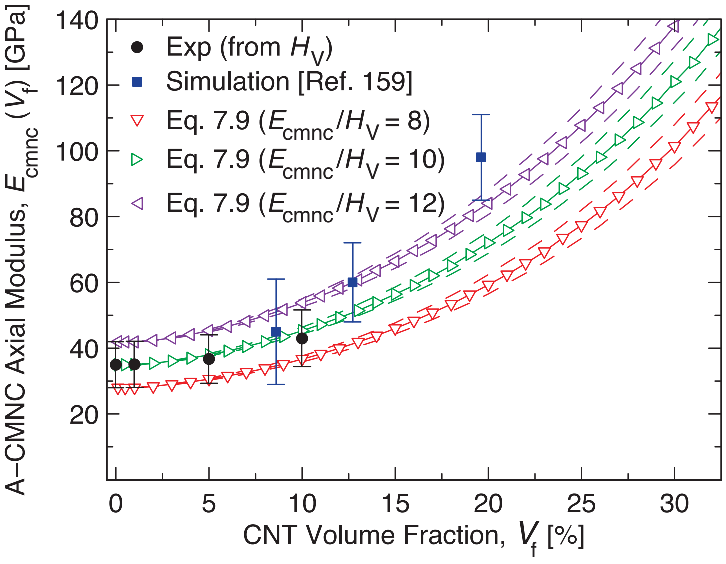

Figure 7.18: Axial modulus scaling with V_f for A-CMNCs. The scaling of $E_{\text{cmnc}}(V_f)$ as a function of the CNT morphology (via Eq. 7.9) is compared to the experimentally quantified $E_{\text{cmnc}}(V_f)$ that was converted from H_V using the previously reported empirical conversion factor of $E_{\text{cmnc}}/H_V \sim 8-12\times$.[267] Additionally, the theoretical and experimental $E_{\text{cmnc}}(V_f)$ results are compared to the results of a previous simulation study on an A-CMNC that has an a-C matrix.[159]

contributions of the extension, bending, and shear deformation mechanisms for $Y/G \sim 30$ that indicate that the shear and bending modes contribute equally and dominate the effective compliance of A-CMNCs. As Figure 7.18 demonstrates, the predictions of Eq. 7.9 have very good agreement with both the converted experimental E_{cmnc}, and the A-CMNC values previously reported in Ref. 159. Additionally, although manufacturing difficulties associated with the productions of the A-CMNCs, *e.g.* the presence of physisorbed water that fills up the inter-CNT region,[46] prevented the study of A-CMNCs at $V_f > 10\%$ for this dissertation, the predictions of Eq. 7.9 indicate that $E_{\text{cmnc}} > 100$ GPa may be possible at $V_f \gtrsim 30\%$ (see Figure 7.18). Processing improvement could enable the realization of such high values for the V_f of A-CMNCs, since the current technique used to increase the V_f of the A-CNT arrays could be used to make A-CNT arrays with $V_f > 30\%$.[29] To compare the expected A-CMNC performance as a function of V_f to other superhard materials, the theoretical scaling of the ρ_{cmnc} was evaluated using rule of mixtures (via $\rho_{\text{pyc}} \approx 1.13 \pm 0.06$ g/cm^3 and intrinsic density of CNTs $\rho_{\text{cnt}} \sim 1.7$ g/cm^3)[28], and the values predicted by Eq. 7.9 were converted back to H_V. See Table 7.5 for exemplary predicted A-CMNC H_V (converted from E_{cmnc}) values at $V_f = 1\%$, 5%, 10%, 15%, 20%, 25%, and 30% that were converted back to H_V.

Comparison of the experimental and (the converted) theoretical scaling of H_V for A-CMNCs synthesized at $T_p = 1400$°C to literature values of H_V of the materials included in Table 7.4 using the H_V/ρ and H_V/ρ^2 design parameters can be found in Figure 7.19. See Table 7.5 for the estimated specific H_V of A-CMNCs. As Figure 7.19 demonstrates, H_V of the A-CMNCs studied here, especially the predicted value for $V_f = 30\%$ fall right in the middle of the H_V of superhard materials, and is equivalent to the H_V of AlN, GaN, NbN, and ZrO_2 on an absolute scale. Using the H_V/ρ design parameter, Figure 7.19 and Table 7.5 illustrate that the A-CMNCs at $V_f = 30\%$ can outperform most of the superhard materials, and be equivalent in performance to $\beta-Si_3N_4$. Additionally, when the H_V/ρ^2 aerospace design parameter is utilized to analyze the performance of the A-CMNCs, Figure 7.19 and Table 7.5 illustrate that the A-CMNCs at $V_f = 30\%$ are predicted to be equivalent in performance to diamond, and is therefore the leading superhard material for aerospace applications. This result is significant because the PyCs studied here are thermally stable at operating temperatures $> 1000°C$ and pressures < 1 GPa (as extensively illustrated in Section 7.4.1), which is not true of either diamond, or c$-$BN (the closest alternative to diamond). Diamond was previously reported to oxidize at $\sim 600°C$, graphitize at $\sim 1400°C$, and readily react with molten ferrous materials to form soot.[300,302–305] On the other hand, c$-$BN was reported to not react with molten ferrous materials,[304–306] and have higher oxidation ($\sim 1200°C$) and 'graphitization' ($\sim 1500°C$) temperatures

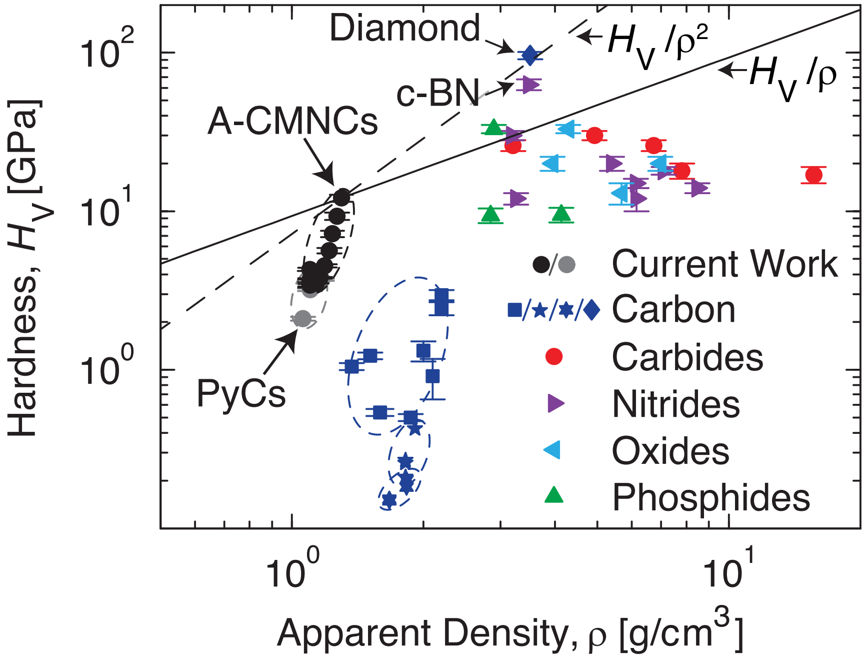

Figure 7.19: Hardness (H_V) as a function of density (ρ) for the A-CMNCs studied here and various other PyCs, carbon materials, and superhard materials as summarized in Figure 7.17. This plot shows that A-CMNCs synthesized at $V_f > 30\%$ could outperform diamond in super lightweight aerospace structure that use H_V/ρ^2 design parameter for materials selection.

than diamond,[304,305,307] but the synthesis of high performing c−BN requires the high temperature and high pressure conversion of graphite-like hexagonal BN (h−BN) phase, which can be achieved through pyrolysis,[308,309] to diamond-like c−BN.[310,311] This type of processing is too expensive and yields c−BN crystals that are too small for many high value industrial applications.[305] Additionally, synthesis of c−BN *via* CVD may enable wider application of this superhard material, but c−BN films prepared using current techniques exhibit crystallites that are very small and highly defective which diminishes their performance.[305] Since high performing A-CMNCs can be readily made *via* the pyrolysis of A-PNC precursors without the need for extreme post-processing, *i.e.* high temperature and high pressure conditions, A-CMNCs are attractive candidates for next-generation lightweight materials.

7.5 Conclusions and Recommendations for Future Work

This Chapter presented the extensive crystallite geometry, bonding character, and chemical characterization of the PyC matrix of the A-CMNCs, and the resulting experimental and theoretical structure-property relations of the A-CMNCs and their PyC matrix as a function of both T_p and V_f. The XRD results indicate that as T_p increases from $T_\mathrm{p} = 600°\mathrm{C}$ to $T_\mathrm{p} = 1000°\mathrm{C}$, L_a and L_c of the graphitic crystallites in the pure PyCs grow in magnitude noticeably, whereas L_a and L_c of the graphitic crystallites that comprise the PyC matrix of the A-CMNCs do not evolve a statistically significant amount. This indicates that the presence of the CNTs in the A-CMNCs assists the self-organization of the graphitic crystallites that comprise their PyC matrix, but since the d_{002} for pure PyCs and the PyC matrix in the A-CMNCs shows the same evolution as a function of T_p, the A-CNTs do not alter the graphitic nature of the crystallites that comprise the A-CMNC matrix. The results of Raman spectroscopy further support this conclusion, since $I_\mathrm{D}/I_\mathrm{G}$, $A_\mathrm{D}/A_\mathrm{G}$, γ_D, and γ_G which are indicative of the position of the PyCs in the amorphization trajectory show no statistically significant change as V_f increases up to $\sim 10\%$ CNTs. Additionally, the results of FTIR spectroscopy show that other than slightly less distinct C−O stretching bands, there is very little difference between the pure PyC matrix and the A-CMNCs. These results indicate that the CNT confinement effects on the graphitic crystallites that comprise the PyC matrix are very weak for $V_\mathrm{f} \leq 10\%$ A-CNTs, and are only noticeable on the ~ 10 nm scale (the same order of magnitude as the inter-CNT spacing Γ), which means that further work on higher V_f A-CMNCs is needed, and that future study of the morphology and geometry evolution of the graphitic crystallites that comprise the A-CMNC matrix in 3D *via* a newly developed quantitative electron tomography technique is necessary.[157] Also, theoretical modeling of the 2D arrangement of the graphitic crystallites in the PyCs allows ρ_{pyc} to be predicted, HD and LD PyCs to be distinguished, and the degree of porosity to be inferred. Modeling of the PyC mechanical properties indicates that C_{44} by far dominates the measured H_{V} of the PyCs, and that the evolution of L_a/L_c and d_{002} explains the observed non-monotonic scaling of H_{V} with T_{p}, where smaller d_{002} and larger L_a/L_c correspond to enhanced mechanical performance. Comparison of the H_{V} results of PyCs using the H_{V}/ρ (lightweight materials) and H_{V}/ρ^2 (super lightweight materials) design parameters shows that the performance of the PyCs studied here is average for superhard materials using the H_{V}/ρ design parameter, and among the best performing superhard materials when the H_{V}/ρ^2 design parameter is used (equivalent in performance to BP and $\beta-\mathrm{Si_3N_4}$. A-CMNC hardness results indicate that V_{f} increases enhance the A-CMNC H_{V}, and modeling indicates that A-CMNCs at $V_{\mathrm{f}} = 30\%$ could see $> 300\%$ enhancements in H_{V} when compared to the pure PyC matrix. Additionally, comparison of the experimental and theoretical H_{V} results for A-CMNCs to other superhard materials using the H_{V}/ρ and H_{V}/ρ^2 design parameters shows that the A-CMNCs perform as well as BP and $\beta-\mathrm{Si_3N_4}$ for lightweight materials, and perform similarly to diamond for super lightweight materials, such as aerospace structures. This means that A-CMNCs at $V_{\mathrm{f}} > 30\%$ could outperform all other known superhard materials, thereby making them one of the leading candidates for high hardness low density applications. Since A-CMNCs at $V_{\mathrm{f}} \geq 30\%$ could in theory be manufactured at large scales, exhibit thermal stability at temperatures $> 1400°\mathrm{C}$, and have a specific hardness that is comparable or better than the current state-of-the-art superhard materials (diamond and c$-$BN), but their experimental synthesis was not yet achieved, further work is required to improve the A-CMNC processing at $V_{\mathrm{f}} > 10\%$. Once A-CMNCs at $V_{\mathrm{f}} \geq 30\%$ can be made in large scales, next-generation high hardness, high temperature, low density aerospace architectures with enhanced performance could be designed and manufactured.

In the next Chapter, the contributions of this thesis are summarized, the results presented in Chapters 4, 5, 6, and 7 are used to recommend future paths of study, and the conclusions that can be drawn from this work are discussed.

Chapter 8

Conclusions and Recommendations

The work presented in this thesis was conducted to elucidate the impact of NF structure and morphology on the performance of aligned NF arrays, specifically A-CNT arrays, and their nanocomposites. The 3D morphology and mechanical behavior of A-CNT arrays, A-PNCs, and A-CMNCs were quantified using experimental characterization, theoretical modeling, and multi-scale simulation. The A-CNT packing structure was evaluated as a function of CNT proximity both experimentally, *via* electron microscopy, and theoretically, *via* an effective two-dimensional coordination number model. A simulation capable of modeling $> 10^5$ CNTs that comprise A-CNT arrays with 3D stochastic wavy morphologies was developed, and show that square packing is a reasonable approximation for high waviness ($w > 0.2$) while hexagonal close packing is best for low waviness ($w < 0.1$). Additionally, the 3D morphology simulation was used in conjunction with experimental results to analyze the average coordination and inter-CNT spacing of A-CNT arrays as a function of packing proximity, and indicates that the CNT waviness decreases from $w \sim 0.2$ to $w \sim 0.1$ as V_f increases from $\sim 1\%$ to $\sim 20\%$, which lead to a linear scaling of the waviness correction factor for the inter-CNT spacing in the V_f regime studied here. Mechanical property modeling using stochastic wavy 3D A-CNT morphology using an analysis originally developed for carbon nanocoils, shows that the torsion and shear deformation mechanisms of the CNTs, which are governed by the very low G of CNTs ($\rightarrow Y/G \sim 1000$), dominate their effective compliance and are responsible for the $\sim 1000\times$ stiffness enhancement previously observed for these A-CNT arrays as V_f is increased from $\sim 1\%$ to $\sim 20\%$. Extension of the stochastic wavy 3D morphology based mechanical modeling approach to A-PNCs and A-CMNCs *via* rule of mixtures indicates that the significant relative shear stiffness contribution of the matrix, which effectively eliminates the torsion deformation mechanism of the CNTs due to matrix bonding, governs the CNT reinforcement efficacy, and that the ratio of Y and the matrix modulus ($\rightarrow Y/E_{\text{pm}} \sim 300$ and $Y/E_{\text{cm}} \sim 30$ in the current work) determines the contribution of the CNT deformation mechanism to the effective axial A-CNT compliance. In-depth analysis of the geometry and morphology, bonding character, and chemical structure of the graphitic crystallites that comprise the PyC matrix as a function of processing indicates that the crystallite geometry and graphitic nature can be utilized to model their structure-mechanical property relations, and that the A-CNTs facilitate self-organization of the graphitic crystallites on the meso-scale without changing their degree of graphitization, and therefore mechanical behavior at $V_{\text{f}} \leq 10\%$. Finally, taking into account the low density of the A-CMNCs, this dissertation shows that A-CMNCs synthesized at $V_{\text{f}} > 30\%$ could overtake diamond as the top performing superhard material for super lightweight structures, such as aerospace structures.

Using these results, the property prediction tools developed in this thesis can be applied to other A-CNT systems, and should be applicable in most cases to aligned NF systems in general, and the step-by-step approach to apply the current analysis to other NF architectures was outlined. Additionally, the limitations and validity regimes of the theoretical and simulations frameworks developed in this work were identified and discussed. Finally, factors that cannot be quantified or integrated into current theory, but strongly influence the 3D CNT morphology and mechanical behavior, were identified, and paths for their future quantification were outlined.

In the remainder of this Chapter, a summary of the dissertation contributions, and the recommended paths of future study are presented.

8.1 Summary of Thesis Contributions

The major contributions and findings of this dissertation are as follows:

Development of multi-scale simulation for modeling up to 1 million CNTs with 3D stochastic wavy morphologies

Using a previously developed model that ties Γ to V_{f}, and newly developed relations that enable easy conversions of the deterministic w to τ, this dissertation presents a simulation framework that, using xyz space displacements on the nm-scale, is able to re-produce the meso-scale topology of CNTs that comprise A-CNT systems in 3D. The error scaling of this simulation in the produced A-CNT morphology is shown to scale as $1/\sqrt{n}$, and the computational efficiency of this meso-scale morphology modeling approach is exemplified by the capability of the presented simulation framework to accommodate $n > 10^5$ CNTs with run times that are < 24 hr. Additionally, this thesis contains a detailed guide that can enable the use of this simulation framework in future studies of other A-CNT arrays, and aligned NF systems in general.

CNT packing geometry and waviness evolution quantified as a function of packing proximity

Analysis *via* SEM indicates that the average waviness of A-CNT arrays undergoing mechanical densification decreases non-linearly from $w \sim 0.2$ at $V_\mathrm{f} \approx 1\%$ CNTs, the as-grown state, to $w \sim 0.1$ at $V_\mathrm{f} \approx 20\%$ CNTs, the highest CNT packing explored here. These results are significant because previous studies that did not have access to this CNT morphology trend either assumed a constant CNT waviness, *e.g.* $w = 0.25 - 0.3$, or neglected the CNT waviness altogether, *i.e.* $w = 0$. This dissertation shows that neither approximation is appropriate and should not be used in future studies. Using the 3D CNT morphology simulation, this thesis shows that using non-representative measures of the CNT waviness can lead to errors in Γ that may exceed 10%, and that the ideal hexagonal close packing ($N = 6$) is best suited for A-CNT arrays as studied here with minimal waviness ($w < 0.1$), whereas square close packing ($N = 4$) works best for A-CNT arrays with noticeable waviness ($w > 0.2$). Also, using the scaling of Γ and w as a function of V_f, it is shown that N of the CNTs increases much faster than previously expected as V_f increases, and that the CNT morphology can be adequately described using hexagonal close packing (in conjunction with waviness) at $V_\mathrm{f} \gtrsim 20\%$.

Torsion and shear deformation mechanisms govern axial elastic behavior of A-CNT arrays

The previously observed four orders of magnitude reduction in the effective A-CNT array axial stiffness at $V_\mathrm{f} \approx 1\%$ CNTs, *i.e.* ~ 1 MPa measured vs. ~ 10 GPa predicted ($\rightarrow Y \sim 1$ TPa),[29] is demonstrated to originate from the CNT waviness. Modeling indicates that the low G of the CNTs, which governs the shear and torsion deformation mechanisms, dominates the effective compliance of the A-CNTs, and that their incomplete consideration in past theoretical models leads to overpredictions of the A-CNT stiffness by *orders of magnitude*. Additionally, by including information on the V_f scaling of both the mean value and statistical uncertainty of the CNT waviness, the current analysis is able to replicate the previously reported $\sim 1000\times$ enhancement in effective axial modulus, *i.e.* from ~ 1 MPa at $V_\mathrm{f} \approx 1\%$ to ~ 1 GPa at $V_\mathrm{f} \approx 20\%$, observed for A-CNT arrays. Finally, the modeling results show that, while the bending deformation mechanism is normally assumed to dominate the effective axial compliance contribution in A-CNT systems, the bending deformation mechanism is not the dominant stiffness loss mechanism in A-CNT arrays (where $Y/G \sim 1000$).

Polymeric matrix reduces CNT waviness and enhances axial CNT reinforcement of A-PNCs by eliminating torsion

By integrating 3D morphology information of A-CNT arrays into mechanical models, this dissertation shows that the much lower than expected effective stiffness of A-PNCs originates from the tortuosity of the CNTs. Also, by including information on both the uncertainty and V_f scaling of the waviness, the simulation is able to replicate the previously reported effective stiffness of A-PNCs with $Y/E_\mathrm{m} \sim 200-300$, while outperforming the mechanical property predictions of previous FEA models that were only capable of analyzing CNTs with a constant w. Additionally, the simulation indicates that the presence of a polymer matrix reduces the waviness of the A-CNTs in the A-PNC by $\approx 10\% - 25\%$ when compared to the waviness of as-grown (having no matrix) A-CNT arrays. Using these results, mechanical modeling indicates that the effective axial modulus of CNTs in the A-PNCs evolves from $\sim$ 10 GPa to $\sim$ 30 GPa as V_f increases, which is significantly smaller than predicted by current theory.

Graphitic crystallites in PyCs do not evolve significantly between 1000 - 1400°C

It was expected that as T_p increases, the L_a and L_c of the graphitic crystallites in the pure PyCs would increase in magnitude. However, the XRD results indicate that the L_a and L_c of the graphitic crystallites in the pure PyCs only grow from $T_\mathrm{p} = 600°\mathrm{C}$ to $T_\mathrm{p} = 1000°\mathrm{C}$, and stay about the same from $T_\mathrm{p} = 1000°\mathrm{C}$ to $T_\mathrm{p} = 1400°\mathrm{C}$, the highest T_p studied here. This indicates that at $T_\mathrm{p} > 1000°\mathrm{C}$, the graphitic crystallites in the PyCs become more inter-connected, *i.e. via* sp^3 'defects', but do not have sufficient energy to self-organize into larger crystallites, which is illustrated by a plateau in L_a and L_c. Raman spectroscopy further support this explanation, since $I_\mathrm{D}/I_\mathrm{G}$ and $A_\mathrm{D}/A_\mathrm{G}$ increase with T_p, which is normally indicative of more defects being formed, while $\gamma_\mathrm{D}/\gamma_\mathrm{G}$ decreases with T_p, which shows that the PyC is moving toward becoming NC graphite in the amorphization trajectory. FTIR spectroscopy also supports this idea by showing that there is noticeable chemical evolution of the PyCs from $T_\mathrm{p} = 600°\mathrm{C}$ to $T_\mathrm{p} = 1000°\mathrm{C}$, while the spectra do not change significantly from $T_\mathrm{p} = 1000°\mathrm{C}$ to $T_\mathrm{p} = 1400°\mathrm{C}$.

Correlations that relate crystallite geometry with Raman spectroscopy require modification for these PyCs

The correlation that was originally proposed by Tuinstra and Koenig,[233] and later modified by a number authors to account for laser energy differences, is the benchmark relation used to extract quantitative information about L_a from the Raman spectrum (via $I_\mathrm{D}/I_\mathrm{G}$ and/or $A_\mathrm{D}/A_\mathrm{G}$) for graphitic materials without the need for confirmation *via* XRD or neutron scattering, but this dissertation clearly shows that such a correlation does not hold generally and also for LD PyCs studied here. To explain the observed trend of $I_\mathrm{D}/I_\mathrm{G}$ with L_a, the previously proposed scaling relation for a-C transforming into NC graphite (*i.e.* stage $2 \rightarrow 1$, see related discussion in Chapter 7) was modified to intersect with a laser energy corrected correlation based on the benchmark relation but at a much larger $L_a \sim 6$ nm (up from the original $L_a = 2-3$ nm). This is due to a longer lifetime of the photoexcited virtual electron-hole pair in the highly defective graphitic crystallites that comprise the PyCs, which could be caused by doping, *e.g.* by electron or hole donors like nitrogern and boron, or other effects that enhance electron-electron interactions. These results indicate that the Tuinstra and Koenig relation fails at $L_a > 6$ nm in highly disordered PyCs, like the ones studied here, and should therefore not be used to analyze all carbon materials without at least confirmation of the relation's applicability from XRD or neutron scattering.

Modeling of the crystallite arrangement in PyCs enables non-destructive analysis of their micro/nano-structure

Knowing the L_a and L_c of the graphitic crystallites should enable the prediction of micro/nano-structure related material properties, and this dissertation shows that a simple geometrical relation can be utilized to model the apparent density of the PyCs. Also, since the model predictions exhibit very good agreement with experimental density data for HD PyCs, but the density of LD PyCs is noticeably overpredicted, this correlation can be used to easily and non-destructively distinguish PyCs that exhibit the HD crystallite arrangement from those that exhibit the LD crystallite ordering. Additionally, this model could be used to approximate the amount of > 100 nm pores present in the PyCs and their specific surface area without the need for undertaking surface area analysis studies.

Non-monotonic hardness scaling of PyCs is governed by the inter-layer shear modulus and crystallite geometry

Since the C_{44} ($\rightarrow C_{44} \sim 0.3-5$ GPa) inter-layer shear constant for graphitic materials is orders of magnitude smaller than the in-plane C_{11} ($\rightarrow C_{11} \sim 1$ TPa) and out-of-plane C_{33} ($\rightarrow C_{33} \sim 30-40$ GPa) extension stiffness constants, the model developed in this dissertation shows that C_{44} by far dominates the measured H_V of the PyCs. Additionally, modeling indicates that the evolution of L_a/L_c and d_{002} explains the observed non-monotonic scaling of H_V with T_p, where smaller d_{002} and larger L_a/L_c correspond to enhanced hardness and stiffness. These results indicate that although increasing T_p can lead to more graphitic crystallites, which increases their C_{44}, this higher T_p will also lead to much smaller aspect ratio crystallites (*i.e.* L_a/L_c decreases), which makes them more sensitive to inter-layer shear deformation. This means that although pyrolysis at higher temperatures can lead to more graphite-like PyCs, their mechanical performance will be diminished. Such an insight helps dispel the confusion in the literature that surrounds why some PyCs become more compliant as T_p increases, while others remain superhard, and this has to do directly with the evolution of their average L_a, L_c, and d_{002}.

A-CNTs lead to meso-scale evolution of the PyC matrix, but atomic structure of the crystallites is unchanged

As the XRD results illustrate, the L_a and L_c of the graphitic crystallites that comprise the PyC matrix of the A-CMNCs do not evolve significantly as T_p increases from $T_\mathrm{p} = 600°\mathrm{C}$ to $T_\mathrm{p} = 1400°\mathrm{C}$. This indicates that the presence of the CNTs in the A-CMNCs helps with the self-organization of the graphitic crystallites that comprise their PyC matrix, but since the d_{002} for pure PyCs and the PyC matrix in the A-CMNCs shows the same evolution as a function of T_p, the A-CNTs do not alter the graphitic nature of the crystallites that comprise the A-CMNC matrix. The results of Raman spectroscopy further support this hypothesis, since $I_\mathrm{D}/I_\mathrm{G}$, $A_\mathrm{D}/A_\mathrm{G}$, γ_D, and γ_G which are indicative of the position of the PyCs in the amorphization trajectory show no statistically significant change as V_f increases up to $\sim 10\%$ CNTs. Additionally, the results of FTIR spectroscopy show that other than a slightly less distinct $\mathrm{C{-}O}$ stretching bands, there is very little difference between the pure PyC matrix and the A-CMNCs. These results indicate that the CNT effects on the graphitic crystallites that comprise the PyC matrix are very weak, and are only noticeable on the ~ 10 nm scale (the same order of magnitude as the inter-CNT spacing Γ) for A-CNT $V_\mathrm{f} \leq 10\%$.

A-CMNCs could outperform diamond in high hardness low density aerospace structures

The experimental A-CMNC hardness results indicate that V_f increases enhance the A-CMNC H_V, and modeling indicates that A-CMNCs at $V_\mathrm{f} = 30\%$ could see $> 300\%$ enhancement in H_V and axial stiffness when compared to the pure PyC matrix. Additionally, comparison of the experimental and theoretical H_V results for A-CMNCs to other superhard materials using the H_V/ρ (lightweight materials) and H_V/ρ^2 (super lightweight materials) design parameters shows that the A-CMNCs perform as well as BP and $\beta{-}\mathrm{Si_3N_4}$ for lightweight materials, and perform similarly to diamond for super lightweight materials, such as aerospace structures. This means that A-CMNCs at $V_\mathrm{f} > 30\%$ (note that only $V_\mathrm{f} \leq 10\%$ was achieved in this thesis) could outperform all other known superhard materials, thereby making them one of the leading candidates for high hardness low density applications.

8.2 Recommendations for Future Work

The work presented in this thesis raises a number of unanswered questions. In an effort to address these points, the following future work is proposed:

NF morphology in true three dimensions

- ▷ Experimental evaluation and re-construction of the CNT topology in three dimensions *via* quantitative electron tomography, similar to the recent work by Natarajan et al.[157]
- ▷ Atomistic and meso-scale modeling of the CNT electrostatic interactions as a function of CNT proximity and surface chemistry.
- ▷ Extension of the 3D morphology simulation to explicitly account for CNT-CNT interactions.
- ▷ Study and modeling of the spatial evolution of the A-CNT packing structure during mechanical manipulation.

Mechanical behavior of A-CNTs

- ▷ Atomistic and NCM exploration of the nm-scale evolution of the CNTs during deformation.
- ▷ Exploration of the impact of defects, such as divacancies and inter-layer bonds, on the shear and torsion deformation modes in the CNTs that comprise A-CNT arrays.
- ▷ Modeling and simulation of CNT-CNT frictional effects as a function of mechanical testing technique, *e.g.* indentation with different tip geometries, as discussed in Cebeci, Stein, and Wardle.[29]
- ▷ Experimental and theoretical prediction of the full elastic constitutive relations of A-CNT arrays as a function of V_f.

Full elastic constitutive relations of A-PNCs

- ▷ Experimentally informed, *via* Handlin et al.,[158] FEA and meso-scale modeling of the full elastic constitutive relations (*i.e.* beyond solely axial stiffness) of A-PNCs and their evolution with CNT packing proximity.
- ▷ Atomistic and meso-scale modeling of the impact of a CNT-polymer interphase layer on the load transfer between the A-CNTs and polymer matrix in A-PNCs.
- ▷ *In situ* mechanical testing and 3D topology re-construction to explore impact of polymeric matrix on the CNT deformation mechanisms activated in A-PNCs.

PyC matrix modeling and evaluation

- ▷ Analysis of atomic and meso-scale evolution of the graphitic crystallites that comprise the PyCs as a function of processing *via* small and wide angle x-ray scattering, similar to the recent work by Faber et al.[312]
- ▷ Modeling and simulation of inter-layer bonding and disorder and their impact on the inter-layer shear modulus of graphitic crystallites.
- ▷ Theoretical and experimental exploration of the load transfer efficacy of sp^3 crystallite-crystallite junctions.

A-CMNC synthesis and processing

- ▷ Exploration of vapor phase polymer infusion methods to enable synthesis of A-CMNCs at $V_f > 30\%$.
- ▷ Experimental quantification of the impact re-infusion processing has on the chemical structure and nature of A-CMNCs.
- ▷ A study of the importance of atmosphere and pressure on the porosity and nanostructure of the A-CMNCs.

Structure-mechanical property relations for A-CMNCs as a function of CNT proximity

- ▷ A study of the role CNT confinement plays during the formation and self-organization of the graphitic crystallites that comprise the PyC matrix of the A-CMNCs, especially at $V_f > 10\%$.

- ▷ Atomistic and meso-scale modeling of the evolution of CNT-CNT junctions inside of the A-CMNCs during deformation.
- ▷ Simulation of the formation of a CNT-PyC interphase region, and its impact on load transfer.

Thermal and electrical property modeling and prediction for A-CNT systems

- ▷ Modeling of the influence of CNT-CNT junction on barriers to phonon and electron hopping.
- ▷ Simulation of the evolution of CNT-CNT junctions as a function of CNT proximity and their contribution to energy dissipation mechanisms.
- ▷ Investigation of the role of native wall defects, inter-layer, and local curvature play on the phonon and electron scattering probabilities in the CNTs that comprise A-CNT systems.
- ▷ Experimental characterization of non-isotropic thermal and electrical conduction in A-CNT nanocomposites as a function of V_{f}.

Appendix A

Waviness Data

This Appendix contains the values of the waviness amplitude (a, see Table A.1), wavelength (λ, see Table A.2). A correction factor of $\sqrt(2)$ was used to adjust w for a view angle of 45° $\rightarrow$ $w = \sqrt{2} \times a/\lambda$ here. The values in Tables A.1$-$ A.2 were approximated from 30 CNTs captured in HRSEM images of the cross-sectional morphologies of the outer edges and middle sections of A-CNT arrays at $V_{\mathrm{f}} \sim 1\%$, 6%, 10.6%, and 20%.

Table A.1: Experimentally evaluated waviness amplitude (a) for A-CNT arrays a function of V_f.

$a(V_f = 1\%)$ [nm]	$a(V_f = 6\%)$ [nm]	$a(V_f = 10.6\%)$ [nm]	$a(V_f = 20\%)$ [nm]
29	22	16	86
39	153	166	56
14	63	86	66
31	69	141	77
37	37	25	66
77	45	20	61
37	101	18	106
17	23	65	40
121	211	89	82
321	60	47	72
226	153	58	45
143	91	64	38
120	13	96	105
174	124	28	59
169	51	158	49
158	18	129	108
88	51	109	65
314	75	75	112
121	131	105	59
431	148	100	34
79	53	35	48
197	83	34	43
137	73	67	71
129	142	99	100
210	128	94	94
74	53	46	37
361	110	71	42
45	95	120	80
104	148	67	36
95	103	23	105
137 ± 107	81 ± 57	75 ± 42	68 ± 25

Table A.2: Experimentally evaluated waviness wavelength (λ) for A-CNT arrays a function of V_f.

$\lambda(V_\mathrm{f}=1\%)$ [nm]	$\lambda(V_\mathrm{f}=6\%)$ [nm]	$\lambda(V_\mathrm{f}=10.6\%)$ [nm]	$\lambda(V_\mathrm{f}=20\%)$ [nm]
259	590	796	1031
427	691	1120	785
259	659	568	894
399	783	799	1114
251	670	735	894
473	555	691	1178
271	550	381	1334
313	446	551	666
1123	843	716	1058
1077	783	525	633
585	910	886	1335
856	1055	986	809
2395	796	730	781
1064	620	665	1096
1021	555	1449	1059
1622	630	1131	754
1466	749	1372	1335
1572	908	1014	808
1239	561	702	1470
2263	1084	900	1508
1364	1072	1137	1184
1689	534	538	1126
1328	1231	811	814
721	1376	1000	701
842	987	780	1270
662	829	1279	1367
1129	392	962	757
1020	1136	513	957
785	1438	957	942
1268	1291	1320	1102
991 ± 571	824 ± 282	867 ± 263	1025 ± 250

References

[1] A. Bezryadin, C. N. Lau, and M. Tinkham, Nature **404**, 971 (2000).

[2] J. E. Mooij and Y. Nazarov, Nature Phys. **2**, 169 (2006).

[3] J. Wang, M. Singh, M. Tian, N. Kumar, B. Liu, C. Shi, J. K. Jain, N. Samarth, T. E. Mallouk, and M. H. W. Chan, Nature Phys. **6**, 389 (2010).

[4] K. Xu and J. R. Heath, Nano Lett. **8**, 3845 (2008).

[5] S. Shen, A. Henry, J. Tong, R. Zheng, and G. Chen, Nature Nanotechnol. **5**, 251 (2010).

[6] Y. Zhang, M. S. Dresselhaus, Y. Shi, Z. Ren, and G. Chen, Nano Lett. **11**, 1166 (2011).

[7] A. A. Balandin, Nature Mater. **10**, 569 (2011).

[8] A. M. Marconnet, M. A. Panzer, and K. E. Goodson, Rev. Mod. Phys. **85**, 1295 (2013).

[9] B. Wu, A. Heidelberg, and J. J. Boland, Nature Mater. **4**, 525 (2005).

[10] C. Q. Chen, Y. Shi, Y. S. Zhang, J. Zhu, and Y. J. Yan, Phys. Rev. Lett. **96**, 075505 (2006).

[11] B. Wen, J. E. Sader, and J. J. Boland, Phys. Rev. Lett. **101**, 175502 (2008).

[12] M. F. L. De Volder, S. H. Tawfick, R. H. Baughman, and A. J. Hart, Science **339**, 535 (2013).

[13] D. Kauffman and A. Star, Angew. Chem., Int. Ed. **47**, 6550 (2008).

[14] Q. Cao and J. A. Rogers, Adv. Mater. **21**, 29 (2009).

[15] W. Lu and C. M. Lieber, Nature Mater. **6**, 841 (2007).

[16] Z. Fan, J. C. Ho, T. Takahashi, R. Yerushalmi, K. Takei, A. C. Ford, Y.-L. Chueh, and A. Javey, Adv. Mater. **21**, 3730 (2009).

[17] J. A. Rogers, T. Someya, and Y. Huang, Science **327**, 1603 (2010).

[18] L. Liu, W. Ma, and Z. Zhang, Small **7**, 1504 (2011).

[19] A. M. Marconnet, N. Yamamoto, M. A. Panzer, B. L. Wardle, and K. E. Goodson, ACS Nano **5**, 4818 (2011).

[20] S. Vaddiraju, H. Cebeci, K. K. Gleason, and B. L. Wardle, ACS Appl. Mater. Interfaces **1**, 2565 (2009).

[21] E. J. Garcia, B. L. Wardle, A. J. Hart, and N. Yamamoto, Compos. Sci. Technol. **68**, 2034 (2008).

[22] B. L. Wardle, D. S. Saito, E. J. García, A. J. Hart, R. Guzmán de Villoria, and E. A. Verploegen, Adv. Mater. **20**, 2707 (2008).

[23] M. K. Shin, J. Oh, M. Lima, M. E. Kozlov, S. J. Kim, and R. H. Baughman, Adv. Mater. **22**, 2663 (2010).

[24] A. T. Sepúlveda, R. Guzmán de Villoria, J. C. Viana, A. J. Pontes, B. L. Wardle, and L. A. Rocha, Nanoscale **5**, 4847 (2013).

[25] L. Ci, J. Suhr, V. Pushparaj, X. Zhang, and P. M. Ajayan, Nano Lett. **8**, 2762 (2008).

[26] I. Y. Stein, H. M. Vincent, S. A. Steiner, E. Colombini, and B. L. Wardle, in *54th AIAA Structures, Structural Dynamics, and Materials (SDM) Conference* (Boston, MA, 2013).

[27] I. Y. Stein, *Synthesis and Characterization of Next-Generation Multifunctional Material Architectures: Aligned Carbon Nanotube Carbon Matrix Nanocomposites*, Master's thesis, Massachusetts Institute of Technology (2013).

[28] I. Y. Stein and B. L. Wardle, Carbon **68**, 807 (2014).

[29] H. Cebeci, I. Y. Stein, and B. L. Wardle, Appl. Phys. Lett. **104**, 023117 (2014).

[30] B. Peng, M. Locascio, P. Zapol, S. Li, S. L. Mielke, G. C. Schatz, and H. D. Espinosa, Nature Nanotechnol. **3**, 626 (2008).

[31] M.-F. Yu, O. Lourie, M. J. Dyer, K. Moloni, T. F. Kelly, and R. S. Ruoff, Science **287**, 637 (2000).

[32] M.-F. Yu, B. S. Files, S. Arepalli, and R. S. Ruoff, Phys. Rev. Lett. **84**, 5552 (2000).

[33] J.-P. Salvetat, G. A. D. Briggs, J.-M. Bonard, R. R. Bacsa, A. J. Kulik, T. Stöckli, N. A. Burnham, and L. Forró, Phys. Rev. Lett. **82**, 944 (1999).

[34] K. Koziol, J. Vilatela, A. Moisala, M. Motta, P. Cunniff, M. Sennett, and A. Windle, Science **318**, 1892 (2007).

[35] N. Behabtu, C. C. Young, D. E. Tsentalovich, O. Kleinerman, X. Wang, A. W. K. Ma, E. A. Bengio, R. F. ter Waarbeek, J. J. de Jong, R. E. Hoogerwerf, S. B. Fairchild, J. B. Ferguson, B. Maruyama, J. Kono, Y. Talmon, Y. Cohen, M. J. Otto, and M. Pasquali, Science **339**, 182 (2013).

[36] C. P. Deck, J. Flowers, G. S. B. McKee, and K. Vecchio, J. Appl. Phys. **101**, 023512 (2007).

[37] T. Tong, Y. Zhao, L. Delzeit, A. Kashani, M. Meyyappan, and A. Majumdar, Nano Lett. **8**, 511 (2008).

[38] A. Qiu, D. Bahr, A. Zbib, A. Bellou, S. Mesarovic, D. McClain, W. Hudson, J. Jiao, D. Kiener, and M. Cordill, Carbon **49**, 1430 (2011).

[39] Y. Won, Y. Gao, M. A. Panzer, S. Dogbe, L. Pan, T. W. Kenny, and K. E. Goodson, Carbon **50**, 347 (2012).

[40] I. Y. Stein, D. J. Lewis, and B. L. Wardle, Nanoscale **7**, 19426 (2015).

[41] I. Y. Stein and B. L. Wardle, Phys. Chem. Chem. Phys. **18**, 694 (2016).

[42] I. Y. Stein and B. L. Wardle, Nanotechnology **27**, 035701 (2016).

[43] I. Y. Stein and B. L. Wardle, Phys. Chem. Chem. Phys. **15**, 4033 (2013).

[44] A. J. Hart and A. H. Slocum, J. Phys. Chem. B **110**, 8250 (2006).

[45] B. Lee, Y. Baek, M. Lee, D. H. Jeong, H. H. Lee, J. Yoon, and Y. H. Kim, Nature Commun. **6**, 7109 (2015).

[46] I. Y. Stein, N. Lachman, M. E. Devoe, and B. L. Wardle, ACS Nano **8**, 4591 (2014).

[47] X. Chen, S. Zhang, D. A. Dikin, W. Ding, R. S. Ruoff, L. Pan, and Y. Nakayama, Nano Lett. **3**, 1299 (2003).

[48] R. R. Mitchell, N. Yamamoto, H. Cebeci, B. L. Wardle, and C. V. Thompson, Compos. Sci. Technol. **74**, 205 (2013).

[49] Y. Yun, V. Shanov, Y. Tu, M. J. Schulz, S. Yarmolenko, S. Neralla, J. Sankar, and S. Subramaniam, Nano Lett. **6**, 689 (2006).

[50] H. Cebeci, R. Guzmán de Villoria, A. J. Hart, and B. L. Wardle, Compos. Sci. Technol. **69**, 2649 (2009).

[51] A. Dombovari, N. Halonen, A. Sapi, M. Szabo, G. Toth, J. MÃČÂďklin, K. Kordas, J. Juuti, H. Jantunen, A. Kukovecz, and Z. Konya, Carbon **48**, 1918 (2010).

[52] Q. Cheng, J. Wang, J. Wen, C. Liu, K. Jiang, Q. Li, and S. Fan, Carbon **48**, 260 (2010).

[53] T. Souier, C. Maragliano, M. Stefancich, and M. Chiesa, Carbon **64**, 150 (2013).

[54] T. W. Ebbesen, H. J. Lezec, H. Hiura, J. W. Bennett, H. F. Ghaemi, and T. Thio, Nature **382**, 54 (1996).

[55] C. Gómez-Navarro, P. J. D. Pablo, J. Gómez-Herrero, B. Biel, F. J. Garcia-Vidal, A. Rubio, and F. Flores, Nature Mater. **4**, 534 (2005).

[56] M. A. Kuroda and J.-P. Leburton, Phys. Rev. B **80**, 165417 (2009).

[57] A. Salehi-Khojin, F. Khalili-Araghi, M. A. Kuroda, K. Y. Lin, J.-P. Leburton, and R. I. Masel, ACS Nano **5**, 153 (2011).

[58] M. Y. Han, B. Özyilmaz, Y. Zhang, and P. Kim, Phys. Rev. Lett. **98**, 206805 (2007).

[59] J. Li, Z. Li, G. Zhou, Z. Liu, J. Wu, B.-L. Gu, J. Ihm, and W. Duan, Phys. Rev. B **82**, 115410 (2010).

[60] J. Haskins, A. Kinaci, C. Sevik, H. Sevinçli, G. Cuniberti, and T. Çağin, ACS Nano **5**, 3779 (2011).

[61] S. Ihnatsenka and G. Kirczenow, Phys. Rev. B **88**, 125430 (2013).

[62] A. V. Krasheninnikov and K. Nordlund, J. Appl. Phys. **107**, 071301 (2010).

[63] J. A. Robinson, E. S. Snow, c. C. Bádescu, T. L. Reinecke, and F. K. Perkins, Nano Lett. **6**, 1747 (2006).

[64] P. C. P. Watts, N. Mureau, Z. Tang, Y. Miyajima, J. D. Carey, and S. R. P. Silva, Nanotechnology **18**, 175701 (2007).

[65] A. S. Jombert, K. S. Coleman, D. Wood, M. C. Petty, and D. A. Zeze, J. Appl. Phys. **104**, 094503 (2008).

[66] A. Salehi-Khojin, C. R. Field, J. Yeom, and R. I. Masel, Appl. Phys. Lett. **96**, 163110 (2010).

[67] Y. Ling, G. Gu, R. Liu, X. Lu, V. Kayastha, C. S. Jones, W.-S. Shih, and D. C. Janzen, J. Appl. Phys. **113**, 024312 (2013).

[68] A. Boyd, I. Dube, G. Fedorov, M. Paranjape, and P. Barbara, Carbon **69**, 417 (2014).

[69] D. Janas and K. K. Koziol, Nanoscale **6**, 3037 (2014).

[70] J. Lee, I. Y. Stein, M. E. Devoe, D. J. Lewis, N. Lachman, S. S. Kessler, S. T. Buschhorn, and B. L. Wardle, Appl. Phys. Lett. **106**, 053110 (2015).

[71] K. Zhang, J. Zou, and Q. Zhang, Nanotechnology **26**, 455501 (2015).

[72] S. Pathak, J. R. Raney, and C. Daraio, Carbon **63**, 303 (2013).

[73] M. Bedewy and A. J. Hart, Nanoscale **5**, 2928 (2013).

[74] Y. Zhang, G. Zou, S. K. Doorn, H. Htoon, L. Stan, M. E. Hawley, C. J. Sheehan, Y. Zhu, and Q. Jia, ACS Nano **3**, 2157 (2009).

[75] V. Bezugly, H. Eckert, J. Kunstmann, F. Kemmerich, H. Meskine, and G. Cuniberti, Phys. Rev. B **87**, 245409 (2013).

[76] E. A. Laird, F. Kuemmeth, G. A. Steele, K. Grove-Rasmussen, J. Nygård, K. Flensberg, and L. P. Kouwenhoven, Rev. Mod. Phys. **87**, 703 (2015).

[77] C. Yu, L. Shi, Z. Yao, D. Li, and A. Majumdar, *Nano Letters*, Nano Lett. **5**, 1842 (2005).

[78] M. Fujii, X. Zhang, H. Xie, H. Ago, K. Takahashi, T. Ikuta, H. Abe, and T. Shimizu, Phys. Rev. Lett. **95**, 065502 (2005).

[79] E. Pop, D. Mann, Q. Wang, K. Goodson, and H. Dai, *Nano Letters*, Nano Lett. **6**, 96 (2006).

[80] S. Shaikh, L. Li, K. Lafdi, and J. Huie, Carbon **45**, 2608 (2007).

[81] A. E. Aliev, M. H. Lima, E. M. Silverman, and R. H. Baughman, Nanotechnology **21**, 035709 (2010).

[82] R. N. Salaway and L. V. Zhigilei, Int. J. Heat Mass Transfer **70**, 954 (2014).

[83] A. Hashimoto, K. Suenaga, A. Gloter, K. Urita, and S. Iijima, Nature **430**, 870 (2004).

[84] M. T. Pettes and L. Shi, Adv. Funct. Mater. **19**, 3918 (2009).

[85] E. Pop, V. Varshney, and A. K. Roy, MRS Bull. **37**, 1273 (2012).

[86] F. Hao, D. Fang, and Z. Xu, Appl. Phys. Lett. **99**, 041901 (2011).

[87] T. Ng, J. Yeo, and Z. Liu, Carbon **50**, 4887 (2012).

[88] M. Goryachev, D. L. Creedon, S. Galliou, and M. E. Tobar, Phys. Rev. Lett. **111**, 085502 (2013).

[89] S.-H. Tan, L.-M. Tang, Z.-X. Xie, C.-N. Pan, and K.-Q. Chen, Carbon **65**, 181 (2013).

[90] Z. Zhu, X. Yang, M. Huang, Q. He, G. Yang, and Z. Wang, Nanotechnology **27**, 055401 (2016).

[91] A. N. Volkov, R. N. Salaway, and L. V. Zhigilei, J. Appl. Phys. **114**, 104301 (2013).

[92] M. L. Bauer, Q. N. Pham, C. B. Saltonstall, and P. M. Norris, Appl. Phys. Lett. **105**, 151909 (2014).

[93] Z. Xu and M. J. Buehler, Nanotechnology **20**, 185701 (2009).

[94] A. N. Volkov, T. Shiga, D. Nicholson, J. Shiomi, and L. V. Zhigilei, J. Appl. Phys. **111**, 053501 (2012).

[95] G. Li and Z. Ren, EPL **113**, 16002 (2016).

[96] C. Lin, H. Wang, and W. Yang, Nanotechnology **21**, 365708 (2010).

[97] V. Lee, R. Chen, and C.-W. Chang, Phys. Rev. B **87**, 035406 (2013).

[98] J. Ma, Y. Ni, S. Volz, and T. Dumitrică, Phys. Rev. Appl. **3**, 024014 (2015).

[99] Z. Aksamija and I. Knezevic, Appl. Phys. Lett. **98**, 141919 (2011).

[100] L. Zhu and B. Li, Sci. Rep. **4**, 4917 (2014).

[101] O. V. Yazyev and Y. P. Chen, Nature Nanotechnol. **9**, 755 (2014).

[102] N. J. Ginga, W. Chen, and S. K. Sitaraman, Carbon **66**, 57 (2014).

[103] M. Sammalkorpi, A. Krasheninnikov, A. Kuronen, K. Nordlund, and K. Kaski, Phys. Rev. B **70**, 245416 (2004).

[104] Q. Lu and B. Bhattacharya, Nanotechnology **16**, 555 (2005).

[105] C. Wong, Comput. Mater. Sci. **49**, 143 (2010).

[106] J. Xiao, J. Staniszewski, and J. W. Gillespie, Jr., Mater. Sci. Eng. A **527**, 715 (2010).

[107] L. Pan, Z. Shen, Y. Jia, and X. Dai, Phys. B (Amsterdam, Neth.) **407**, 2763 (2012).

[108] K. I. Tserpes, Acta Mech. **223**, 669 (2012).

[109] Z. Song, V. I. Artyukhov, B. I. Yakobson, and Z. Xu, Nano Lett. **13**, 1829 (2013).

[110] A. Zandiatashbar, G.-H. Lee, S. J. An, S. Lee, N. Mathew, M. Terrones, T. Hayashi, C. R. Picu, J. Hone, and N. Koratkar, Nature Commun. **5**, (2014).

[111] J. H. Los, A. Fasolino, and M. I. Katsnelson, Phys. Rev. Lett. **116**, 015901 (2016).

[112] L. Muthaswami, Y. Zheng, R. Vajtai, G. Shehkawat, P. Ajayan, and R. E. Geer, Nano Lett. **7**, 3891 (2007).

[113] C. Tang, Y. Zhang, W. Guo, and C. Chen, J. Phys. Chem. C **114**, 18091 (2010).

[114] G. Lopez-Polin, C. Gomez-Navarro, V. Parente, F. Guinea, M. I. Katsnelson, F. Perez-Murano, and J. Gomez-Herrero, Nature Phys. **11**, 26 (2015).

[115] D. Kvashnin and P. Sorokin, J. Phys. Chem. Lett. **6**, 2384 (2015).

[116] G. Savini, Y. Dappe, S. Öberg, J.-C. Charlier, M. Katsnelson, and A. Fasolino, Carbon **49**, 62 (2011).

[117] X. Chen, C. Yi, and C. Ke, Appl. Phys. Lett. **106**, 101907 (2015).

[118] X.-L. Wei, Y. Liu, Q. Chen, M.-S. Wang, and L.-M. Peng, Adv. Funct. Mater. **18**, 1555 (2008).

[119] G. Guhados, W. Wan, X. Sun, and J. L. Hutter, J. Appl. Phys. **101**, 033514 (2007).

[120] K. Liu, Y. Sun, L. Chen, C. Feng, X. Feng, K. Jiang, Y. Zhao, and S. Fan, Nano Lett. **8**, 700 (2008).

[121] W. Fu, L. Liu, K. Jiang, Q. Li, and S. Fan, Carbon **48**, 1876 (2010).

[122] C.-M. Seah, S.-P. Chai, and A. R. Mohamed, Carbon **49**, 4613 (2011).

[123] S. Park, M. Vosguerichian, and Z. Bao, Nanoscale **5**, 1727 (2013).

[124] O. Eberhardt and T. Wallmersperger, Carbon **95**, 166 (2015).

[125] S. W. Cranford and M. J. Buehler, Nanotechnology **21**, 265706 (2010).

[126] J.-L. Tsai, S.-H. Tzeng, and Y.-T. Chiu, Composites, Part B **41**, 106 (2010).

[127] S. Yang, S. Yu, W. Kyoung, D.-S. Han, and M. Cho, Polymer **53**, 623 (2012).

[128] R. Rafiee and R. M. Moghadam, Composites, Part B **56**, 435 (2014).

[129] A. Alian, S. Kundalwal, and S. Meguid, Polymer **70**, 149 (2015).

[130] A. Alian, S. Kundalwal, and S. Meguid, Compos. Struct. **131**, 545 (2015).

[131] C. Li and T.-W. Chou, Compos. Sci. Technol. **66**, 2409 (2006).

[132] G. M. Odegard, T. S. Gates, L. M. Nicholson, and K. E. Wise, Compos. Sci. Technol. **62**, 1869 (2002).

[133] C. Li and T.-W. Chou, Int. J. Solids Struct. **40**, 2487 (2003).

[134] L. Nasdala and G. Ernst, Comput. Mater. Sci. **33**, 443 (2005).

[135] W.-H. Chen, H.-C. Cheng, and Y.-L. Liu, Comput. Mater. Sci. **47**, 985 (2010).

[136] L. Lu, J. Liu, Y. Hu, Y. Zhang, H. Randriamahazaka, and W. Chen, Adv. Mater. **24**, 4317 (2012).

[137] L. Nasdala, A. Kempe, and R. Rolfes, Compos. Sci. Technol. **72**, 989 (2012).

[138] M. J. Buehler, J. Mater. Res. **21**, 2855 (2006).

[139] S. Cranford, H. Yao, C. Ortiz, and M. J. Buehler, J. Mech. Phys. Solids **58**, 409 (2010).

[140] S. Hu, H. Jiang, Z. Xia, and X. Gao, ACS Appl. Mater. Interfaces **2**, 2570 (2010).

[141] B. Xie, Y. Liu, Y. Ding, Q. Zheng, and Z. Xu, Soft Matter **7**, 10039 (2011).

[142] M. G. Hahm, H. Wang, H. Y. Jung, S. Hong, S.-G. Lee, S.-R. Kim, M. Upmanyu, and Y. J. Jung, Nanoscale **4**, 3584 (2012).

[143] Y. Li and M. Kröger, Carbon **50**, 1793 (2012).

[144] I. Ostanin, R. Ballarini, D. Potyondy, and T. Dumitrică, J. Mech. Phys. Solids **61**, 762 (2013).

[145] X. Liu, W. Lu, O. M. Ayala, L.-P. Wang, A. M. Karlsson, Q. Yang, and T.-W. Chou, Nanoscale **5**, 2002 (2013).

[146] C. Wang, L. Wang, and Z. Xu, Carbon **64**, 237 (2013).

[147] Y. Won, Y. Gao, M. A. Panzer, R. Xiang, S. Maruyama, T. W. Kenny, W. Cai, and K. E. Goodson, Proc. Natl. Acad. Sci. U.S.A. **110**, 20426 (2013).

[148] L. V. Zhigilei, C. Wei, and D. Srivastava, Phys. Rev. B **71**, 165417 (2005).

[149] A. N. Volkov and L. V. Zhigilei, J. Phys. Chem. C **114**, 5513 (2010).

[150] A. N. Volkov and L. V. Zhigilei, Phys. Rev. Lett. **104**, 215902 (2010).

[151] A. N. Volkov and L. V. Zhigilei, ACS Nano **4**, 6187 (2010).

[152] W. M. Jacobs, D. A. Nicholson, H. Zemer, A. N. Volkov, and L. V. Zhigilei, Phys. Rev. B **86**, 165414 (2012).

[153] Y. Wang, I. Ostanin, C. Gaidău, and T. Dumitrică, Langmuir **31**, 12323 (2015).

[154] R. H. Poelma, X. Fan, Z.-Y. Hu, G. Van Tendeloo, H. W. van Zeijl, and G. Q. Zhang, Adv. Funct. Mater. **26**, 1233 (2016).

[155] Y. Liu, Nanotechnology **26**, 442501 (2015).

[156] M. Mahdavi, M. Baniassadi, M. Baghani, M. Dadmun, and M. Tehrani, Nanotechnology **26**, 385704 (2015).

[157] B. Natarajan, N. Lachman, T. Lam, D. Jacobs, C. Long, M. Zhao, B. L. Wardle, R. Sharma, and J. A. Liddle, ACS Nano **9**, 6050 (2015).

[158] D. Handlin, I. Y. Stein, R. Guzman de Villoria, H. Cebeci, E. M. Parsons, S. Socrate, S. Scotti, and B. L. Wardle, J. Appl. Phys. **114**, 224310 (2013).

[159] K. Chae and L. Huang, J. Phys. Chem. C **119**, 6806 (2015).

[160] J.-Q. Huang, Q. Zhang, G.-H. Xu, W.-Z. Qian, and F. Wei, Nanotechnology **19**, 435602 (2008).

[161] P. Vinten, J. Bond, P. Marshall, J. Lefebvre, and P. Finnie, Carbon **49**, 4972 (2011).

[162] H. Jinnai, R. J. Spontak, and T. Nishi, Macromolecules **43**, 1675 (2010).

[163] P. A. Midgley and R. E. Dunin-Borkowski, Nature Mater. **8**, 271 (2009).

[164] G. Van Tendeloo, S. Bals, S. Van Aert, J. Verbeeck, and D. Van Dyck, Adv. Mater. **24**, 5655 (2012).

[165] M. C. Scott, C.-C. Chen, M. Mecklenburg, C. Zhu, R. Xu, P. Ercius, U. Dahmen, B. C. Regan, and J. Miao, Nature **483**, 444 (2012).

[166] H. Malik, K. J. Stephenson, D. F. Bahr, and D. P. Field, J. Mater. Sci. **46**, 3119 (2011).

[167] O. M. Fakron and D. P. Field, Ultramicroscopy **149**, 21 (2015).

[168] F. T. Fisher, R. D. Bradshaw, and L. C. Brinson, Appl. Phys. Lett. **80**, 4647 (2002).

[169] F. Fisher, R. Bradshaw, and L. Brinson, Compos. Sci. Technol. **63**, 1689 (2003).

[170] E. Shady and Y. Gowayed, Compos. Sci. Technol. **70**, 1476 (2010).

[171] A. Y. Matveeva, S. V. Pyrlin, M. M. Ramos, H. J. Böhm, and F. W. van Hattum, Comput. Mater. Sci. **87**, 1 (2014).

[172] S. Paunikar and S. Kumar, Comput. Mater. Sci. **95**, 21 (2014).

[173] M. R. Maschmann, Carbon **86**, 26 (2015).

[174] A. Pantano, D. M. Parks, and M. C. Boyce, J. Mech. Phys. Solids **52**, 789 (2004).

[175] I. Nikiforov, D.-B. Zhang, R. D. James, and T. Dumitrică, Appl. Phys. Lett. **96**, 123107 (2010).

[176] Y. Kinoshita, M. Kawachi, T. Matsuura, and N. Ohno, Phys. E (Amsterdam, Neth.) **54**, 308 (2013).

[177] C. D. Latham, M. I. Heggie, M. Alatalo, S. Öberg, and P. R. Briddon, J. Phys.: Condens. Matter **25**, 135403 (2013).

[178] T. Trevethan, P. Dyulgerova, C. D. Latham, M. I. Heggie, C. R. Seabourne, A. J. Scott, P. R. Briddon, and M. J. Rayson, Phys. Rev. Lett. **111**, 095501 (2013).

[179] U. Vainio, T. I. W. Schnoor, S. Koyiloth Vayalil, K. Schulte, M. Müller, and E. T. Lilleodden, J. Phys. Chem. C **118**, 9507 (2014).

[180] J.-K. Lee, S.-C. Lee, J.-P. Ahn, S.-C. Kim, J. I. B. Wilson, and P. John, J. Chem. Phys. **129**, 234709 (2008).

[181] A. Cao, P. L. Dickrell, W. G. Sawyer, M. N. Ghasemi-Nejhad, and P. M. Ajayan, Science **310**, 1307 (2005).

[182] J. Suhr, P. Victor, L. Ci, S. Sreekala, X. Zhang, O. Nalamasu, and P. M. Ajayan, Nature Nanotechnol. **2**, 417 (2007).

[183] A. A. Zbib, S. D. Mesarovic, E. T. Lilleodden, D. McClain, J. Jiao, and D. F. Bahr, Nanotechnology **19**, 175704 (2008).

[184] L. Ge, L. Ci, A. Goyal, R. Shi, L. Mahadevan, P. M. Ajayan, and A. Dhinojwala, Nano Lett. **10**, 4509 (2010).

[185] C. Cao, A. Reiner, C. Chung, S.-H. Chang, I. Kao, R. V. Kukta, and C. S. Korach, Carbon **49**, 3190 (2011).

[186] M. R. Maschmann, Q. Zhang, F. Du, L. Dai, and J. Baur, Carbon **49**, 386 (2011).

[187] M. R. Maschmann, Q. Zhang, R. Wheeler, F. Du, L. Dai, and J. Baur, ACS Appl. Mater. Interfaces **3**, 648 (2011).

[188] K. Eom, K. Nam, H. Jung, P. Kim, M. S. Strano, J.-H. Han, and T. Kwon, Carbon **65**, 305 (2013).

[189] N. J. Ginga and S. K. Sitaraman, Carbon **53**, 237 (2013).

[190] J. Wang, T. Kemper, T. Liang, and S. B. Sinnott, Carbon **50**, 968 (2012).

[191] I. Y. Stein and B. L. Wardle, in *57th AIAA Structures, Structural Dynamics, and Materials (SDM) Conference, AIAA SciTech 2016* (San Diego, CA, 2016).

[192] D. Luo, W.-X. Wang, and Y. Takao, Compos. Sci. Technol. **67**, 2947 (2007).

[193] R. Allen, O. Ghita, B. Farmer, M. Beard, and K. Evans, Compos. Sci. Technol. **77**, 1 (2013).

[194] H. Cebeci, *Multifunctional Properties of Controlled Morphology Aligned Carbon Nanotube Polymer Nanocomposites and Their Applications*, Ph.D. thesis, Istanbul Technical University (2011).

[195] S. Herasati and L. Zhang, Compos. Sci. Technol. **100**, 136 (2014).

[196] N. Subramanian, A. Rai, and A. Chattopadhyay, Carbon **94**, 661 (2015).

[197] D.-L. Shi, X.-Q. Feng, Y. Y. Huang, K.-C. Hwang, and H. Gao, J. Eng. Mater. Technol. **126**, 250 (2004).

[198] L. Shao, R. Luo, S. Bai, and J. Wang, Compos. Struct. **87**, 274 (2009).

[199] P. D. Spanos and M. Esteva, J. Comput. Theor. Nanosci. **6**, 2317 (2009).

[200] R. Rafiee, Compos. Struct. **97**, 304 (2013).

[201] J. N. Dastgerdi, G. Marquis, and M. Salimi, Compos. Sci. Technol. **86**, 164 (2013).

[202] J. N. Dastgerdi, G. Marquis, and M. Salimi, Compos. Struct. **110**, 1 (2014).

[203] J. Varischetti, J.-S. Jang, R. Gibson, and J. Suhr, J. Mater. Sci. **48**, 832 (2013).

[204] F. T. Fisher, *Nanomechanics and the Viscoelastic Behavior of Carbon Nanotube-Reinforced Polymers*, Ph.D. thesis, Northwestern University (2002).

[205] R. Bradshaw, F. Fisher, and L. Brinson, Compos. Sci. Technol. **63**, 1705 (2003).

[206] V. Anumandla and R. F. Gibson, Composites, Part A **37**, 2178 (2006).

[207] A. Pantano and P. Mantione, Appl. Phys. A **99**, 895 (2010).

[208] K. Yazdchi and M. Salehi, Composites, Part A **42**, 1301 (2011).

[209] N. Montinaro and A. Pantano, Compos. Struct. **109**, 246 (2014).

[210] C. Li, E. T. Thostenson, and T.-W. Chou, Compos. Sci. Technol. **68**, 1445 (2008).

[211] M. Omidi, H. R. D.T., A. S. Milani, R. J. Seethaler, and R. Arasteh, Carbon **48**, 3218 (2010).

[212] M. M. Shokrieh and R. Rafiee, Comput. Mater. Sci. **50**, 437 (2010).

[213] B. J. Yang, H. Souri, S. Kim, S. Ryu, and H. K. Lee, J. Appl. Phys. **116**, 033511 (2014).

[214] B. J. Carey, P. K. Patra, M. G. Hahm, and P. M. Ajayan, Adv. Funct. Mater. **23**, 3002 (2013).

[215] A. Needleman, T. L. Borders, L. C. Brinson, V. M. Flores, and L. S. Schadler, Compos. Sci. Technol. **70**, 2207 (2010).

[216] T. Ozkan, Q. Chen, and I. Chasiotis, Compos. Sci. Technol. **72**, 965 (2012).

[217] G. Chen, D. N. Futaba, H. Kimura, S. Sakurai, M. Yumura, and K. Hata, ACS Nano **7**, 10218 (2013).

[218] L.-P. Simoneau, J. Villeneuve, and A. Rochefort, J. Appl. Phys. **118**, 124309 (2015).

[219] L. An, W. Xu, S. Rajagopalan, C. Wang, H. Wang, Y. Fan, L. Zhang, D. Jiang, J. Kapat, L. Chow, B. Guo, J. Liang, and R. Vaidyanathan, Adv. Mater. **16**, 2036 (2004).

[220] S. Sarkar, J. Zou, J. Liu, C. Xu, L. An, and L. Zhai, ACS Appl. Mater. Interfaces **2**, 1150 (2010).

[221] X. Li, K. Li, H. Li, J. Wei, and C. Wang, Carbon **45**, 1662 (2007).

[222] D. Bansal, S. Pillay, and U. Vaidya, Carbon **55**, 233 (2013).

[223] R. E. Franklin, Proc. R. Soc. London, Ser. A **209**, 196 (1951).

[224] N. Iwashita, C. R. Park, H. Fujimoto, M. Shiraishi, and M. Inagaki, Carbon **42**, 701 (2004).

[225] G. A. Zickler, B. Smarsly, N. Gierlinger, H. Peterlik, and O. Paris, Carbon **44**, 3239 (2006).

[226] H. Badenhorst, Carbon **66**, 674 (2014).

[227] M. S. Nyathi, C. B. Clifford, and H. H. Schobert, Fuel **114**, 244 (2013).

[228] A. C. Ferrari and J. Robertson, Phys. Rev. B **61**, 14095 (2000).

[229] A. C. Ferrari and D. M. Basko, Nat. Nanotechnol. **8**, 235 (2013).

[230] M. S. Dresselhaus, A. Jorio, M. Hofmann, G. Dresselhaus, and R. Saito, Nano Lett. **10**, 751 (2010).

[231] A. C. Ferrari, J. C. Meyer, V. Scardaci, C. Casiraghi, M. Lazzeri, F. Mauri, S. Piscanec, D. Jiang, K. S. Novoselov, S. Roth, and A. K. Geim, Phys. Rev. Lett. **97**, 187401 (2006).

[232] C. A. Amadei, I. Y. Stein, G. J. Silverberg, B. L. Wardle, and C. D. Vecitis, Nanoscale **8**, 6783 (2016).

[233] F. Tuinstra and J. L. Koenig, J. Chem. Phys. **53**, 1126 (1970).

[234] L. G. Cançado, K. Takai, T. Enoki, M. Endo, Y. A. Kim, H. Mizusaki, A. Jorio, L. N. Coelho, R. Magalhaes-Paniago, and M. A. Pimenta, Appl. Phys. Lett. **88**, 163106 (2006).

[235] L. G. Cançado, A. Jorio, E. H. M. Ferreira, F. Stavale, C. A. Achete, R. B. Capaz, M. V. O. Moutinho, A. Lombardo, T. S. Kulmala, and A. C. Ferrari, Nano Lett. **11**, 3190 (2011).

[236] M. Lucchese, F. Stavale, E. M. Ferreira, C. Vilani, M. Moutinho, R. B. Capaz, C. Achete, and A. Jorio, Carbon **48**, 1592 (2010).

[237] E. H. Martins Ferreira, M. V. O. Moutinho, F. Stavale, M. M. Lucchese, R. B. Capaz, C. A. Achete, and A. Jorio, Phys. Rev. B **82**, 125429 (2010).

[238] M. S. Shafeeyan, W. M. A. W. Daud, A. Houshmand, and A. Shamiri, J. Anal. Appl. Pyrol. **89**, 143 (2010).

[239] C. Sellitti, J. Koenig, and H. Ishida, Carbon **28**, 221 (1990).

[240] R. Morent, N. De Geyter, C. Leys, L. Gengembre, and E. Payen, Surf. Interface Anal. **40**, 597 (2008).

[241] S. Yajima, T. Hirai, and T. Hayase, Tanso **No. 69**, 41 (1972).

[242] H. Zhang, E. López-Honorato, and P. Xiao, Carbon **91**, 346 (2015).

[243] R. Dettori, E. Cadelano, and L. Colombo, J. Phys.: Condens. Matter **24**, 104020 (2012).

[244] M. Šupová, J. Svítilová, Z. Chlup, M. Černý, Z. Weishauptová, T. Suchý, V. Machovič, Z. Sucharda, and M. Žaloudková, Ceram.-Silik. **56**, 40 (2012).

[245] J.-W. Jiang, J.-S. Wang, and B. Li, Phys. Rev. B **80**, 113405 (2009).

[246] H. Zhao, K. Min, and N. R. Aluru, Nano Lett. **9**, 3012 (2009).

[247] S. Bera, A. Arnold, F. Evers, R. Narayanan, and P. Wölfle, Phys. Rev. B **82**, 195445 (2010).

[248] H. Allouche, M. Monthioux, and R. L. Jacobsen, Carbon **41**, 2897 (2003).

[249] H. Allouche and M. Monthioux, Carbon **43**, 1265 (2005).

[250] M. Monthioux, H. Allouche, and R. L. Jacobsen, Carbon **44**, 3183 (2006).

[251] X. Li, L. Ci, S. Kar, C. Soldano, S. J. Kilpatrick, and P. M. Ajayan, Carbon **45**, 847 (2007).

[252] Q.-M. Gong, Z. Li, X.-D. Bai, D. Li, Y. Zhao, and J. Liang, Mater. Sci. Eng., A **384**, 209 (2004).

[253] Q.-M. Gong, Z. Li, D. Li, X.-D. Bai, and J. Liang, Solid State Commun. **131**, 399 (2004).

[254] S. Prilutsky, E. Zussman, and Y. Cohen, Nanotechnology **19**, 165603 (2008).

[255] L. J. Lanticse-Diaz, Y. Tanabe, T. Enami, K. Nakamura, M. Endo, and E. Yasuda, Carbon **47**, 974 (2009).

[256] Y. Han, S. Li, F. Chen, and T. Zhao, Mater. Today Commun. **6**, 56 (2016).

[257] Z. Zhou, X. Wang, S. Faraji, P. D. Bradford, Q. Li, and Y. Zhu, Carbon **75**, 307 (2014).

[258] B. Saha, A. Furmanchuk, Y. Dzenis, and G. C. Schatz, Carbon **94**, 694 (2015).

[259] Y. Zhang, N. Tajaddod, K. Song, and M. L. Minus, Carbon **91**, 479 (2015).

[260] S. Faraji, K. Stano, C. Rost, J.-P. Maria, Y. Zhu, and P. D. Bradford, Carbon **79**, 113 (2014).

[261] B. D. Jensen, K. E. Wise, and G. M. Odegard, J. Phys. Chem. A **119**, 9710 (2015).

[262] R. H. Telling, C. J. Pickard, M. C. Payne, and J. E. Field, Phys. Rev. Lett. **84**, 5160 (2000).

[263] H. Chacham and L. Kleinman, Phys. Rev. Lett. **85**, 4904 (2000).

[264] D. Roundy and M. L. Cohen, Phys. Rev. B **64**, 212103 (2001).

[265] Y. Zhang, H. Sun, and C. Chen, Phys. Rev. B **73**, 144115 (2006).

[266] Y. Zhang, H. Sun, and C. Chen, Phys. Rev. Lett. **94**, 145505 (2005).

[267] Y. Gogotsi, S. Welz, D. A. Ersoy, and M. J. McNallan, Nature **411**, 283 (2001).

[268] X. Luo, Z. Liu, B. Xu, D. Yu, Y. Tian, H.-T. Wang, and J. He, J. Phys. Chem. C **114**, 17851 (2010).

[269] J. M. Wheeler, R. Raghavan, J. Wehrs, Y. Zhang, R. Erni, and J. Michler, Nano Lett. **16**, 812 (2016).

[270] P. Mallet-Ladeira, P. Puech, P. Weisbecker, G. L. Vignoles, and M. Monthioux, Appl. Phys. A **114**, 759 (2014).

[271] P. Mallet-Ladeira, P. Puech, C. Toulouse, M. Cazayous, N. Ratel-Ramond, P. Weisbecker, G. L. Vignoles, and M. Monthioux, Carbon **80**, 629 (2014).

[272] Z. Li, C. Lu, Z. Xia, Y. Zhou, and Z. Luo, Carbon **45**, 1686 (2007).

[273] J. Rautavuori and P. Törmälä, J. Mater. Sci. **14**, 2020 (1979).

[274] Z. Laušević and S. Marinković, Carbon **24**, 575 (1986).

[275] M. Terrones, N. Grobert, and H. Terrones, Carbon **40**, 1665 (2002).

[276] J. Zhao, L. Yang, F. Li, R. Yu, and C. Jin, Carbon **47**, 744 (2009).

[277] J.-K. Lee, S. Lee, J.-G. Kim, B.-K. Min, Y.-I. Kim, K.-I. Lee, K. H. An, and P. John, Small **10**, 3283 (2014).

[278] M. Mauro, V. Cipolletti, M. Galimberti, P. Longo, and G. Guerra, J. Phys. Chem. C **116**, 24809 (2012).

[279] J.-Y. Hong, J. Kong, and S. H. Kim, Small **10**, 4839 (2014).

[280] C. Casiraghi, A. Hartschuh, H. Qian, S. Piscanec, C. Georgi, A. Fasoli, K. S. Novoselov, D. M. Basko, and A. C. Ferrari, Nano Lett. **9**, 1433 (2009).

[281] C. Hwang, D. A. Siegel, S.-K. Mo, W. Regan, A. Ismach, Y. Zhang, A. Zettl, and A. Lanzara, Sci. Rep. **2**, 590 (2012).

[282] M. Ijäs, M. Ervasti, A. Uppstu, P. Liljeroth, J. van der Lit, I. Swart, and A. Harju, Phys. Rev. B **88**, 075429 (2013).

[283] B. H. Stuart, *Infrared Spectroscopy: Fundamentals and Applications*, edited by D. J. Ando (John Wiley & Sons, Ltd, 2005).

[284] I. Poljanšek and M. Krajaž, Acta Chim. Slov. **52**, 238 (2005).

[285] J. Huang, M. Xu, Q. Ge, M. Lin, Q. Lin, Y. Chen, J. Chu, L. Dai, and Y. Zou, J. Appl. Polym. Sci. **97**, 652 (2005).

[286] S.-S. Tzeng and Y.-G. Chr, Mater. Chem. Phys. **73**, 162 (2002).

[287] M. Inagaki and F. Kang, *Carbon Materials Science and Engineering: From Fundamentals to Applications* (Tsinghua University Press, 2006).

[288] R. A. Cunningham, *High temperature degradation mechanisms in polymer matrix composites*, Master's thesis, Massachusetts Institute of Technology (1997).

[289] L. Zou, B. Huang, Y. Huang, Q. Huang, and C. Wang, Mater. Chem. Phys. **82**, 654 (2003).

[290] L.-R. Bao and A. F. Yee, Polymer **43**, 3987 (2002).

[291] L.-R. Bao, A. F. Yee, and C. Y.-C. Lee, Polymer **42**, 7327 (2001).

[292] T. Belin and F. Epron, Mater. Sci. Eng., B **119**, 105 (2005).

[293] P. Meadows, E. López-Honorato, and P. Xiao, Carbon **47**, 251 (2009).

[294] E. López-Honorato, P. Meadows, and P. Xiao, Carbon **47**, 396 (2009).

[295] T. Oku, A. Kurumada, Y. Imamura, and M. Ishihara, J. Nucl. Mater. **381**, 92 (2008), proceedings of the Seventh and Eighth International Graphite Specialists Meetings (INGSM).

[296] D. M. Teter, MRS Bull. **23**, 22 (1998).

[297] R. Andrievski, Int. J. Refract. Met. Hard Mater. **19**, 447 (2001).

[298] X.-Q. Chen, H. Niu, D. Li, and Y. Li, Intermetallics **19**, 1275 (2011).

[299] B. D. Fulcher, X. Y. Cui, B. Delley, and C. Stampfl, Phys. Rev. B **85**, 184106 (2012).

[300] I. Bello, Y. Chong, K. Leung, C. Chan, K. Ma, W. Zhang, S. Lee, and A. Layyous, Diamond Relat. Mater. **14**, 1784 (2005).

[301] M. F. Ashby, *Materials Selection in Mechanical Design*, 4th ed. (Butterworth-Heinemann, 2010).

[302] G. Demazeau, Diamond Relat. Mater. **4**, 284 (1995).

[303] S. N. Monteiro, A. L. D. Skury, M. G. de Azevedo, and G. S. Bobrovnitchii, J. Mater. Res. Technol. **2**, 68 (2013).

[304] Y.-M. Chong, K.-L. Ma, K.-M. Leung, C.-Y. Chan, Q. Ye, I. Bello, W. Zhang, and S.-T. Lee, Chem. Vap. Deposition **12**, 33 (2006).

[305] W. J. Zhang, Y. M. Chong, I. Bello, and S. T. Lee, J. Phys. D: Appl. Phys. **40**, 6159 (2007).

[306] S. Ulrich, J. Schwan, W. Donner, and H. Ehrhardt, Diamond Relat. Mater. **5**, 548 (1996).

[307] V. L. Solozhenko, V. Z. Turkevich, and W. B. Holzapfel, J. Phys. Chem. B **103**, 2903 (1999).

[308] H. Sumiya, K. Harano, and Y. Ishida, Diamond Relat. Mater. **41**, 14 (2014).

[309] H. Sumiya, Y. Ishida, K. Arimoto, and K. Harano, Diamond Relat. Mater. **48**, 47 (2014).

[310] V. L. Solozhenko, O. O. Kurakevych, and Y. Le Godec, Adv. Mater. **24**, 1540 (2012).

[311] Y. Tian, B. Xu, D. Yu, Y. Ma, Y. Wang, Y. Jiang, W. Hu, C. Tang, Y. Gao, K. Luo, Z. Zhao, L.-M. Wang, B. Wen, J. He, and Z. Liu, Nature **493**, 385 (2013).

[312] K. Faber, F. Badaczewski, M. Oschatz, G. Mondin, W. Nickel, S. Kaskel, and B. M. Smarsly, J. Phys. Chem. C **118**, 15705 (2014).